Mesure des observables de polarisation dans la photoproduction de mésons à Graal. Optimisation de la reconstruction de traces pour l'analyse des canaux à trois particules chargées.

Luisa Nicoletti

ISN 02.09

THÈSE

présentée par

Luisa Nicoletti

pour obtenir le titre de

Docteur de l'Université Joseph Fourier - Grenoble 1

spécialité : PHYSIQUE

Mesure des observables de polarisation dans la photoproduction de mésons à Graal

---

Optimisation de la reconstruction de traces

pour l'analyse des canaux à trois particules chargées

Soutenue le 8 Février 2002

Composition du jury:

J.-F. Bruandet	Président
A. Di Ciaccio	Rapporteur
B. Saghai	Rapporteur
A. Lleres	Directeur de thèse
V. Bellini	Examinateur

Thèse préparée au sein de l'Institut des Sciences Nucléaires de Grenoble

Libro completo
Saltat scriptor pede lacto.

École celtique V-VI siècle après J-C

Les trois années de thèse ont étés une très riche expérience professionelle et de vie. J'ai eu la chance de faire des rencontres fondamentales pour ma formation comme physicienne et comme personne.

Je remercie tout d'abord Joël Chauvin, directeur de l'Institut des Sciences Nucléaires de Grenoble, qui m'a accuelli dans ses laboratoires en me fournissant tous les instruments nécessaires à ma recherche, ainsi que Jean-Paul Bocquet pour m'avoir permis d'effectuer ma thèse dans le groupe *Graal* et pour sa sensibilité vis à vis de toutes les difficultés que j'ai pu rencontrer au cours de ce travail. Un merci chaleureux à ma directrice de thèse Annick Lleres pour la collaboration continue sur les problèmes liés à l'analyse et à l'interpretation des données expérimentales, et pour m'avoir appris à conduire mon travail de façon indépendante. Merci également à Dominique Rebreyend pour le travail fait ensemble afin de comprendre et optimiser les performances des détecteurs et pour les échanges d'idées dans plusieurs domaines.

Je suis très reconnaissante à Anna Di Ciaccio et Bijan Saghai pour avoir accepté d'être rapporteurs de cette thèse et pour leurs commentaires toujours utiles et enrichissants. En particulier je remercie le deuxième d'entre eux pour avoir nourri mes connaissances de physique théorique ainsi que pour son hospitalité au SPHN de Saclay. Je remercie Jean-François Bruandet pour avoir presidié la commission de soutenance et pour les précieux conseils de rédaction, et Vincenzo Bellini, examinateur et collaborateur, pour le soutien donné à mon travail pendant la dernière année de thèse.

Un travail de thèse n'est jamais facile, mais dans mon experience j'ai vécu aussi la difficulté de la recherche des financement pour ma thèse. Je souhaite conseiller aux etudiants qui s'achemineront dans cette entreprise de prévoir dès le debut les possibilités de financement. Je tiens donc à remercier les institutions qui m'ont soutenue financierement: l'INFN pour deux ans, puis les universités de Rome (Tor Vergata) et de Catane en Italie et le CNRS dans le cadre du projet européen HAPHEEP.

Ce que j'ai acquis de plus précieux a été l'expérience de travail dans un environnement international, français, italien et russe: les échanges avec toutes les personnes de mon groupe m'ont permis d'apprendre plusieurs façons de travail. Je ne pourrais pas oublier le soutien de mon cher parrain Jacques Berger, pour avoir toujours su me donner le bon conseil au bon moment et pour les agréables discussions pendant les "soirées" passées au laboratoire. Je suis très reconnaissante envers Carlo Schaerf pour sa confiance et son ecouragement et envers Annalisa D'Angelo, Dario Moricciani et Rachele Di Salvo pour les échanges d'idées et leurs précieux conseils de travail. Je ne oublierai pas la collaboration et la sympathie de Fréderic R., ainsi que celle des mes collègues siciliens Antonio et Cristian et des mes collègues russes Sasha et Slava.

Je suis très reconnaissante envers tous les amis que j'ai eu la chance de rencontrer pendant ces trois annés et avec qui j'ai passé des moments de convivialité trés intenses: en particulier, pour les cours intensifs de vie française sans contrôle, Luc, Nicolas, Manuela, Sébastien, Stefania, Delia, Auguste, Jacob, Frédéric M., Thomas, Sophie et Cristophe. Je remercie encore ceux qui m'ont soutenue dans ma recherche de la Langue Mère, l'*esperanto*: le *chef* Olivier, *le care professoresse* Elena et Ilaria, *i mitici milanesi* Alberto et Giacomo (grâce à qui ce texte est devenu comprehensible...).

Et ces remerciements ne sont pas terminés car il y a encore Gaëlle et Pierlorenzo pour les "entraînements" bretons, Elena M. pour les soirées savoureuses, et de même que Jean-Pierre, Florence, Elène, Bastien et Amélie, qui ont permis la "vrai" *joint-venture* franco-italienne. Et puis merci aussi pour le soutien pendant ces trois années à mes amis de la "Vrai Capitale": Orietta, Francesco, Antonella, désormais anglaise, Fabrizio, Giovanna, Ludovica, Tiziana, Antonello, Silvio, Walter, Margherita e Ferruccio. Et si j'ai oubilé quelqu'un, c'est ici que je le remercie.

La on est à la fin, car c'est à la fin que l'on remercie la famille qui fait le travail les plus difficile, c'est à dire celui d'aimer et d'être loin: donc, grazie per il vostro sostegno Mario, Rita, Alessandro.

Contents

Introduction

Ce travail a été effectué au sein du group Graal de l'Institut des Sciences Nucléaires de Grenoble. L'expérience Graal, située au "European Synchrotron Radiation Facility" de Grenoble, est constituée d'un faisceau de photons Compton polarisés avec une énergie comprise entre 0.5 et 1.5 GeV et d'un détecteur 4π pour l'identification des particules neutres et chargées. L'objectif de cette expérience est l'étude des états excités du nucléon (résonances) au moyen de la photoproduction de mésons et de la mesure d'observables de polarisation.

Différents modèles phénoménologiques et théoriques ont été developpés afin de reproduire le spectre des résonances nucléoniques (et plus largement baryoniques) observé. Ces modèles prédisent également l'existence d'états expérimentalement non observés, qui sont appellés "résonances manquantes". Dans ce contexte, les observables de simple et double polarisation extraites de la photoproduction, qui sont sensibles à l'interference de multipôles permettent de mettre en évidence plus facilement les differentes contributions résonantes et d'en extraire leurs caractéristiques (masse, largeur, ...).

L'utilisation de la sonde électromagnétique (photon ou électron) associée à la détection des états finals des réactions via un calorimètre à large acceptance, des détecteurs de traces et des scintillateurs plastiques constituent un ensemble puissant pour l'étude de la spectroscopie nucléonique. En effet la sonde électromagnétique à la place de la sonde hadronique peut d'une part, amplifier la contribution de certaines résonances et, d'autre part, permet plus facilement l'interpretation des mécanismes de réaction. Par ailleurs, la large acceptance et la bonne résolution spatiale du détecteur rendent possible la réconstruction complète de la cinématique des particules de l'état final des réactions.

Ce travail de thèse est consacré principalement à l'étude et l'analyse des réactions de photoproduction avec trois particules chargées dans l'état final. En particulier la photoproduction d'étrangeté constitue la partie fondamentale du programme du Groupe Graal de l'ISN. La mesure de ces canaux ($K^+\Lambda$,$K\Sigma$) nécessite l'utilisation de détecteurs de traces. L'ISN-Graal a donc construit deux détecteurs spécifiques : un détecteur constitué de deux chambres à fils planes pour la détection des particules chargées aux angles avant

et deux chambres à fils cylindriques pour la mesure des particules chargées aux grands angles.

Le travail principal presenté dans cette thèse a porté sur l'optimisation des programmes de reconstruction des traces du détecteur cylindrique, afin d'améliorer l'efficacité de détection des événements à trois particules chargées. Les performances de ce détecteur ont été testées en analysant la photoproduction du η et du ω via leur décroissance chargée ($\pi^+\pi^-\pi^\circ$).

Dans le premier chapitre la photoproduction de mesons est présentée dans le cadre de modèles et des formalisms theoriques. Le deuxième chapitre est dedié à la description de l'ensemble expérimental Graal. La réponse et les performances des MWPCs cylindriques sont presentées dans le chapitre 3. Les méthodes d'analyse des trois canaux η, ω, $K\Lambda$ sont expliquées au cours du chapitre 4. Dans le chapitre 5 la mesure des asymétries faisceau est montrée pour le η et le $K^+\Lambda$ et les asymétries du $K^+\Lambda$ sont comparées à un modèle pénoménologique.

Chapter 1

Hadron physics at GRAAL

1.1 A survey on Hadron's physics

1.1.1 History

Strong interactions[1] have been introduced in the '30s to explain the force which provides stable nuclei. At this time Heisenberg and others established that the building elements of the atomic nuclei, called "nucleons", are held together by the so-called nuclear forces, which have a short range of about 1 fm. Yukawa thought that each field of force is associated with the exchange of some kind of particles and that there is a simple relation between the range of the forces and the mass of the corresponding particles. Hence he estimated the range from known experimental data and found that the new particles had to be about 200 times heavier than the electrons. This particle was then identified with the meson π.

A new input to this idea was the discovery of the anomalous magnetic moment of the proton, that suggested that it is not point-like but composed by other sub-particles. During the 1940s new particles were discovered, as the Λ, the Ξ^- and the $\Sigma^{\pm}$ in cloud chambers exposed to cosmic rays and their behaviour was "strange": these particles are in fact strongly produced but they decay in longer times as if they undergo a weaker interaction. This property was quantified with a new quantum number, the "strangeness", which is conserved in strong interactions but not in the weak ones. In 1953 Gell-Mann-Nakano-Nishjima classified these new particles as a function of the strangeness. During the 1960s a large number of new particles were discovered with the new particle accelerators in the GeV range and a new classification was accomplished in 1961 by Gell-Mann, and

[1] See [1] for a complete picture

independently by Ne'eman: these particles were composed of three smaller particles, called quarks u, d and s, which were described by the symmetry group SU(3). In their theory, the so called "static quark model", these particles are assembled in two families: only qqq and $q\bar{q}$ states, the so called *baryons* and *mesons*, are permitted. The fundamental states of this model are the mesonic pseudoscalar octet, $\pi^+, \pi^-, \pi^0, K^+, K^-, K^0, \eta_0$ plus the singlet η_8 and the baryonic vectorial decuplet, composed by $p, n, \Sigma^+, \Sigma^0, \Sigma^-, \Xi^-, \Xi^0$ with spin 1/2, $\Delta^-, \Delta^{++}, \Omega^-$ with spin 3/2 and the singlet Λ. The quarks are confined inside these hadrons but the reason of that is still not understood.

The main problem at that time was that in the quantum field-theoretical approach, QFT, which describes the hadrons in terms of the SU(3) symmetry, the coupling constant is not small in comparison with unity. The theory was, thus, difficult to be mathematically studied. The main difficulty for physicists at that time was also treating with non integrally charged quarks: the evidence of the fractional charge was measured with experiments of lepton pairs production in pion-carbon interactions, whose cross section is proportional to the quark charge squared. That is why quark confinement into hadrons was not strictly considered, as difficult to be treated, up to the 1970s. The first who spoke about the QCD[2] was Y. Nambu in 1969. He introduced a new quantum number, the color, which was described with the SU(3) gauge field. The mediators of this new field were an octet of massless vector gauge bosons with spin 1, called gluons, and carrying this new color charge.

In the same years theorists had been trying to understand Bjorken scaling: it is the Q^2 independence of the cross section in the deep-inelastic scattering in lepton-hadron interactions, which was interpreted as the sign of free particles, called "partons".'t Hooft inferred that this "asymptotic freedom" could be explained in the Yang-Mills (spin one) gauge theory and that one could identify the "partons" with the "quarks": quarks and gluons behave as free at high momentum transfer but at low energy they are invisible and the interaction mediators are the hadrons. In this picture quarks and gluons are permanently confined, hence, they will not exist as free particles. Their wave function is a singlet combination of colored quarks and each particle contains also virtual gluons and quark pairs of different flavors. The interaction is mediated either by gluons or by quark-antiquark pairs.

[2]Quantum ChromoDynamics

1.1.2 From low to high energies

In this context we may identify two distinct kinematic regions corresponding to different distance scales. At high energies and small distances the interaction involves elementary quark and gluon fields, acting as quasi-free particles. The interaction is described by perturbative QCD. At low energies and large distances, quarks and gluons appear in "condensed" form as nucleons and mesons, and the reaction is described by the hadron theory.

In this context the best solution would be to exactly resolve the QCD Lagrangian. The challenge of the **Lattice QCD** is to discretize the space-time in order to resolve exactly the Lagrangian in each volume. The main problem of this theory, which gives in this moment some results (as for example the quark confinement, which is associated to the string breaking), is actually the required computer time for the calculation.

At energies close to the reaction threshold (low energies) the quarks are almost invisible and the **Chiral Perturbation Theory** (ChPT) is the most appropriate, because the perturbative development is possible. The ChPT interprets the chiral symmetry group $SU(3)_L \times SU(3)_R$ in terms of the effective low-energy degrees of freedom: they are the Goldstone bosons (π, K, η), resulting from the spontaneous breaking of the symmetry, and the baryon octet (N, Λ, Σ, Ξ). The Lagrangian has the general form [2]:

$$L = L^1_{\phi B} + L^2_{\phi B} + ...$$

where $1, 2, ...$ are the loop expansions corresponding to increasing momenta and quark masses. In the interaction matrix there will be terms fixed by the ChT and other terms, called LECs[3], which cannot be fixed by the ChT.

The ChPT challenge is, moreover, to determine the value of the quark-antiquark condensate, which is the necessary consequence of the spontaneous SU(3) symmetry breaking. The present knowledge on nonperturbative aspects in QCD, does not allow to establish the condensate size, which can be of about $-(250MeV)^3$ or about $-(100MeV)^3$ or even vanishing. In this context the measurement of the η decay into π^+ π^- π° and into $3\pi^\circ$, which is possible at the Graal[4] facility at the ESRF[5] of Grenoble, can give information about the condensate mass. In fact, as explained in Ref. [3] in the generalized chiral perturbation theory developed up to the sixth order, the condensate $\langle q\bar{q}\rangle$ mass is proportional to the constant α. The constant α itself appears at the leading order of the amplitude of

[3]Low Energy Constants

[4]GRenoble Anneau Accélérateur Laser

[5]European Synchrotron Radiation Facility

these two decay channels. Therefore, for a strictly vanishing condensate ($\alpha = 4$) the cross section at low energies is enhanced by a factor 16 for the $3\pi^\circ$ case and 4 for the $\pi^+\pi^-\pi^\circ$ case as compared to the standard case of a strong condensate ($\alpha = 1$). This measurement requires of course a very high control of the efficiency of whole apparatus.

The **Regge theory** of strong interactions, which dominated the 1960s, describes the partial waves amplitudes by the "Regge trajectories" in the complex space of the angular moment. It is reliable at energies greater than 3 GeV. In this picture the hadrons occupy linear trajectories and each family of hadrons is a "Regge pole", with a real value of angular moment. N. Levy [4] used the SU(3) symmetry and the vector-meson dominance (t-channel) to extend the π production theory to the K photoproduction. In this case some effects can be explained, as the difference between the π and K differential cross sections at forward angles.

At intermediate distances (that is to say in the range between the threshold of the meson production up to about $2 - 3$ GeV), which the Graal program is concerned with, quarks and gluons are relevant, however confinement plays a governing role, and quarks appear as constituent quarks confined due to a potential. In the intermediate energies the relationship to QCD remains unclear, although many models describe quite successfully many aspects of hadron spectroscopy. Hence it is essential to provide accurate data that can be confronted with model calculations and show where this picture breaks down in non-trivial ways leading to improved models and to a better understanding of the nucleon structure in terms of its fundamental constituents. The goal of the Graal program is, thus, to probe the internal structure of light quark baryons.

1.2 Nucleon spectroscopy

1.2.1 πN scattering

The meson-nucleon interaction at intermediate energies has been studied in the '70s via the pion-nucleon scattering. This allowed to estimate from the cross section the interaction probability, given by the coupling constant $g_{\pi NN}$. The same experiments also showed that these reactions produce instable intermediate states, whose origin was not known. They were called "baryonic resonances".

A resonant state is an intermediate state produced by a particle interacting with the nucleonic potential. Its evidence is simply calculated by developing the particle in partial waves (a complete base of Legendre polynomials), defined by their orbital quantum num-

ber l and a phase in the complex space. The value of the phase infers if the scattering occurred and if it is elastic or inelastic. The differential cross section (elastic or inelastic scattering) is thus given by the current associated to these waves. In the elastic scattering the amplitude (and thus the cross section) associated to each wave can be mathematically expressed as a Breit-Wigner:

$$A_l = \frac{\Gamma/2}{(E_R - E) - i\Gamma/2}$$

where E_R is the energy of the peak (resonance) and Γ its width. The width is linked to the time of life of the resonance, τ, by the relation $\tau = \hbar/\Gamma$. If the particles have non vanishing isospin and spin the amplitude will be averaged on the initial states and summed on the final ones.

In the meson-nucleon interaction different resonances were identified and they were divided in two types, Δ^* and N^* according to the isospin charge ($I_z = 3/2, 1/2$ for a state composed by a nucleon and a pion). In the spectroscopic notation these resonances are thus described by their mass, m, and by their quantum numbers: the angular momentum J, the parity P, the charge conjugation C and the isospin I. In this notation hadron states and their resonances are given by:

$L_{2I2J}(m)$	for the baryons
$J^{PC}(m)$	for the mesons

Each of them can be produced in a reaction if the conservation rules are satisfied.

The resonances, whose existence has been proved in pion-nucleon production as well as in electromagnetic production, are reported in table 1.1[5]. The resonances have been classified [6] in four families:

- four stars: existence is certain and properties are at least fairly explored;
- three stars: existence ranges form very likely to certain, but further confirmation is desirable and/or quantum numbers, branching ratios, etc. are not well determined;
- two stars: evidence of existence in only fair;
- one star: evidence of existence is poor.

Some of them, as the $S_{11}(1535)$ and $D_{13}(1520)$, have been measured via the $\pi N \to \eta N$ process. More generally, our knowledge on the resonances comes mainly from $\pi N \to \pi N; \eta N$ channels. These reactions have been studied via partial wave analyses [7, 8] and coupled channel approaches [9, 10]. More recently, photoproduction channels have received much attention [11, 12].

Baryon	Three and four star resonances	One and two star resonances
N^*	$S_{11}(1535)$, $S_{11}(1650)$,	$S_{11}(2090)$,
	$P_{11}(1440)$, $P_{11}(1710)$, $P_{13}(1720)$,	$P_{11}(2100)$, $P_{13}(1900)$,
	$D_{13}(1520)$, $D_{13}(1700)$, $D_{15}(1675)$,	$D_{13}(2080)$, $D_{15}(2200)$,
	$F_{15}(1680)$,	$F_{15}(2000)$, $F_{17}(1990)$,
	$G_{17}(2190)$, $G_{19}(2250)$,	
	$H_{19}(2220)$,	
Λ^*	$S_{01}(1405)$, $S_{01}(1670)$, $S_{01}(1800)$,	
	$P_{01}(1600)$, $P_{01}(1810)$, $P_{03}(1890)$,	
	$D_{03}(1520)$, $D_{03}(1690)$, $D_{05}(1830)$,	$D_{03}(2325)$,
	$F_{05}(1820)$, $F_{05}(2110)$,	$F_{07}(2020)$,
	$G_{07}(2100)$,	
	$H_{09}(2350)$,	
Σ^*	$S_{11}(1750)$,	$S_{11}(1620)$, $S_{11}(2000)$,
	$P_{11}(1660)$, $P_{11}(1880)$, $P_{13}(1385)$,	$P_{11}(1770)$, $P_{11}(1880)$, $P_{13}(1840)$,
		$P_{13}(2080)$,
	$D_{13}(1670)$, $D_{13}(1940)$, $D_{15}(1775)$,	$D_{13}(1580)$,
	$F_{15}(1915)$, $F_{17}(2030)$,	$F_{15}(2070)$,
		$G_{17}(2100)$.

Table 1.1: *Isospin-1/2 baryon resonances [5, 6] with mass* $M_{N^*} \leq 2.5$ *GeV*.

1.3 Meson photoproduction at new facilities

1.3.1 Advantages

The new generation of accelerators with high intensity and low emittance, such as CEBAF[6], ELSA[7] and ESRF/Graal, associated to 4π detectors, polarised beams and polarised targets, allow to highlight some particular resonances. The accessible channels in the pseudoscalar meson photoproduction with the Graal polarised beam are:

$$\vec{\gamma} + N \rightarrow \pi + N$$
$$\vec{\gamma} + N \rightarrow \eta + N$$
$$\vec{\gamma} + N \rightarrow K + Y$$

where $Y = \Sigma, \Lambda$.

From a theoretical point of view, the physical observables (we will treat them in the next paragraph) which are extracted from the photoproduction asymmetries, might emphasize in their multipolar structures some resonances which are not present in the differential cross section. The development of polarised photon beams and targets allows in particular to study the polarisation observables. The photon and lepton can, in fact, be easily polarised: a polarisation observable allows to select particular resonant states. In other words the various combinations of the states of the polarised beam, the states of the polarised target and the states of the polarised recoil baryon, give rise to different asymmetry observables, which are the interference of different multipoles. For example, in the photoproduction of pseudoscalar meson the multipolar structure of the target asymmetry is particularly sensitive to the resonances F_{15} and the beam asymmetry to the resonances D_{13}. Furthermore, if one of these channels is studied near its threshold, the multipolar expansion can be truncated at the lower orders, and the resonance contribution is thus amplified.

From a dynamical point of view we must distinguish two aspects: the first is the photoexcitation amplitudes $A_{1/2}$ and $A_{3/2}$, which are the probability to produce a given resonance; the second one is the probability of a given resonance to decay into a particular final state (πN, ηN, KY, ...).

[6]Continuous Electron Beam Accelerator Facility, Virginia

[7]ELectron Stretcher Accelerator, Bonn

The extraction of the photo-excitation amplitudes has been performed on πN and ηN photoproduction, but these previous experiments are limited to the first resonance region ($E_{tot}^{cm} \approx 1.5GeV$): measurements at higher energies require a better resolution of the beam energy, which is the case of the new facilities mentioned above. As the energy increases more decay channels are possible for a given resonance and their branching ratios can be accurately measured with detectors with a large solid angle, which is the case of Graal and CEBAF.

In this context the photoproduction might hopefully highlight the presence of some missing resonances, which have been predicted by QCD-inspired models but that have not been seen so far in the πN systems.

Furthermore the great advantage of the electromagnetic production lies in the perfect knowledge of the electromagnetic interaction of the real or virtual photon with the nucleon, as well as in the possibility to study the electromagnetic form factors of the hyperons.

1.3.2 Polarization observables

We can define single or double polarisation observables, the first being determined by the beam or the target or the recoil polarisations, the latter by the combination of beam-target or beam-recoil or recoil-target polarisations. Together with the unpolarised differential cross section, we have, finally, sixteen observables, but only nine of them are independent. The expression of these observables can be simplified by choosing an appropriate reference system and by expressing transition matrix in terms of the CGLN[8] amplitudes. This calculation has been accomplished [14] for the case of the photoproduction of pseudoscalar ($S = 0, P = -1$) mesons and we summarized it in Appendix A.

The GRAAL experiment consists of a linear polarised γ beam, an unpolarised hydrogen or deuterium target and a 4π detector. Hence, up to now, the unpolarised cross section together with the beam asymmetry $\mathbf{\Sigma}$, the polarisation $\mathbf{P}$ of the recoil hyperon and the double polarisation beam-recoil are our accessible observables. In the near future (2002) a circularly polarised beam together with polarised hydrogen target will be available and the other double polarisation measurements will be accomplished. It is also important to emphasize that the recoil asymmetry can be easily extracted for the hyperon Λ, as it is directly given by the distribution of its decay products.

[8] Chew Goldberger Low Nambu [13]

1.3.3 The D_{13} identification form the beam asymmetry in the η photoproduction

As an illustration we discuss briefly the $\vec{\gamma}p \to \eta p$ reaction, which, near threshold, is known to receive contribution mainly from the S_{11} and D_{13}. One recent result from the Graal collaboration [15] has allowed to identify the resonance $D_{13}(1520)$ in the measurement of the beam asymmetry $\mathbf{\Sigma}$ in the η photoproduction. This channel has been identified by the detection of the two photon from the η decay $\eta \to 2\gamma$ with the electromagnetic calorimeter.

While the cross section up to 1 GeV (see figure 1.1 on the left) is dominated by the resonance $S_{11}(1535)$, concealing the P and D contributions, the beam asymmetry (same figure, on the right) is a clear interference between the $S_{11}(1535)$ and $D_{13}(1520)$ resonances (the Roper $P_{11}(1440)$ is also considered in some models [16]). In particular, in the beam asymmetry we can appreciate the difference of the isobar model [16] when the D_{13} resonance is introduced (dashed line) or not (dotted line). At energies near the threshold the multipolar expansion of the beam asymmetry can be truncated at $L \leq 2$ (the complete expression is given in equation (A.11)) and the dominant term is:

$$\mathbf{\Sigma} \approx 3sin^2\theta Re[E^*_{0+}(E_{2-} + M_{2+})]$$

where $(E_{2-} + M_{2+})$ corresponds to the multipolar component of the resonance D_{13}. Its contribution is clearly given by the dashed line in figure 1.1 (right). The measurement of the beam asymmetry at Graal in figure 1.2 clearly show the D_{13} contribution.

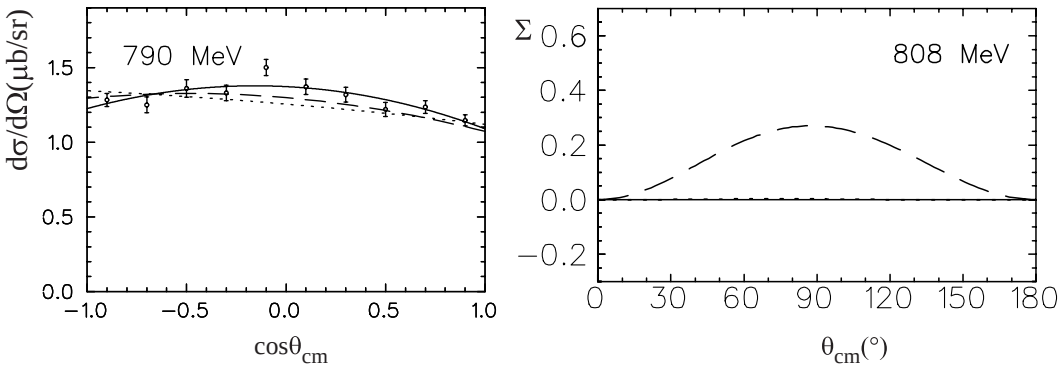

Figure 1.1: *Differential cross section (left) and beam asymmetry (right) for $p(\vec{\gamma}, \eta)p$. The solid line show the fit to the experimental data of Krusche et al. [17]. The dashed lines is the isobar model from [16]. The dotted lines are obtained form the same model when the resonance D_{13} is turned off.*

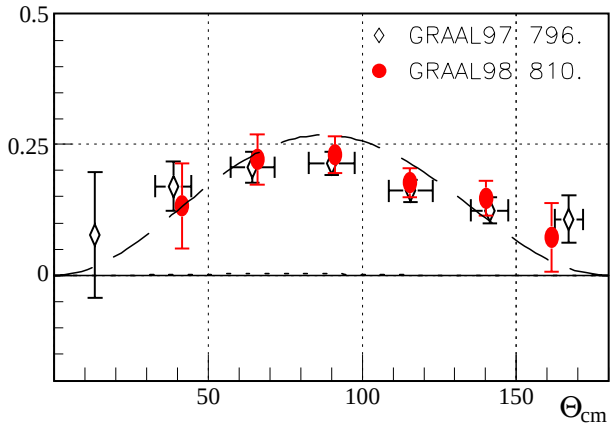

Figure 1.2: *Beam asymmetry measurement from [15] in the η photoproduction. The curves are the same predictions reported in figure 1.1.*

1.3.4 Analysis formalisms

As mentioned above, the transition matrix can be expressed as function of the six CGLN amplitudes f_i [13]:

$$d\sigma[CGLN(A_i)] = d\sigma(f_1, f_2, f_3, f_4, f_5, f_6)$$

where the A_i are the Lorentz invariant amplitudes, which depend on the Mandelstam variables (s, u, t). Therefore, the CGLN formalism gives an easier way to calculate the observables once the function f_i have been determined. Different approaches can be used to calculate the function f_i, which can be model independent analyses or phenomenological models.

In the first case we can report two main kind of approaches. The **multipolar analysis** is a powerful formalism that allows to study the observables in a truncated basis of multipoles, $f_i(E_{l\pm}, M_{l\pm})$. The evidence of a given resonance is thus given by its multipolar components which may appear or not in a particular observable (see as example the D_{13} contribution to the beam asymmetry in Section 1.3.2). Moreover at the reaction threshold we can truncate the multipolar basis, keeping the dominant contributions. The maximum orbital momentum l is thus chosen as to give the truncated f_i' the nearest to the expected one, i.e. $(f_i - f_i')/f_i \simeq 1\%$.

The second model independent approach is the **nodal analysis**. The amplitudes f_i are calculated for $J = 1/2$ and $J \leq 3/2$ and so on, from which the number of expected nodal points of the observables (points at which the observable vanishes) is calculated. The presence of these points can be associated to the appearance or disappearance of a given

family of resonances. Moreover, the fact that the number of nodes is different from the expected one might signify that an s channel has been interpreted as a t one.

The phenomenological models aim to calculate the amplitudes A_i which appear in a given reaction. They can be calculated either with QCD-inspired models (as the Quark Model, reported in Section 1.5) or via the formalism of the Feynman diagrams. In the following we shall report some main methods.

The **ELA**[9] describes the hadrons via an effective Lagrangian at the tree level, that includes the exchange of particles in the three channels, s, u and t.

The ELA has been used in [18] to study the single pion photoproduction, which is dominated by the $\Delta(1234)$ and in [19] to study the η photoproduction, dominated by the $S_{11}(1535)$ up to $\approx 100 MeV$ above threshold. The extension to higher energies imposes to introduce, besides spin 1/2 and 3/2 resonances, those with spin 5/2, that is difficult from the mathematical point of view.

The **Isobaric formalism** express the reaction amplitudes for the exchanged mesons and baryons in terms of Feynman diagrams at the three level. The invariant Mandelstam variables, s, u and t are used to hopefully select the diagrams which best describe the reaction under consideration. For associated strangeness production the amplitudes and propagators are so calculated by including the extended Born terms, whose intermediate states are the nucleon, the kaon and the hyperon, and the terms including the baryon resonances (s channel) as well as the hyperon (u channel) and kaon (t channel) ones. When the coupling constants are unknown (as in the strangeness photoproduction), the SU(3) symmetry states the range of variability of the relative coupling constants of some vertices, which are treated as free parameters adjusted on data. In this case the combination of amplitudes with the lowest reduced χ^2_{red}, whose coupling constant are comparable to the ones foreseen by the SU(3) symmetry, is thus selected. The isobar analysis of the η photoproduction was accomplished for the first time by Hicks in the '73 [20].

This analysis will be used in chapter 5 to interpret the beam asymmetry of the $K\Lambda$ photoproduction measured at Graal during this thesis.

1.3.5 Strangeness photoproduction

In Section 1.3.2 we have underlined that Graal is one of the most suitable apparatus for the measurement of single and double polarisation observables. The energy of the polarised photon beam corresponds to the centre of mass energies ranging from $W = 1.3\ GeV$

[9] Effective Lagrangian Approach

to 1.9 GeV. In this energy domain we can access to the first ($\simeq$ 1.5 GeV) and second ($\simeq$ 1.7 GeV) regions of the baryonic resonances. The threshold for the associated strangeness (KY) photoproduction is roughly $W = 1.6$ GeV.

The $K\Lambda$ photoproduction is a pure isospin 1/2 channel, while in the $K\Sigma$ photoproduction the isospin 3/2 intermediate states (Δ^*) are also allowed. The study of these two channels is then one of the main parts of the Graal program.

Different reasons can explain the strong interest developed with respect to the strangeness production. At first, the nucleon-nucleon interaction is relatively well known while hyperon-nucleon interactions are still not well understood. In other words, interactions between baryons made of u and d quarks are by far better known than those where strange quarks intervene. In the nucleon, the quark s is not a valence quark, as the u and d, but a sea quark.

In the past, the first measurement concerned (π^+,K^+) and (K^-,π^-) reactions, where both initial and final states are governed by strong interactions. Electro- and photo-production presents on the contrary the great advantage to have a well known interaction in the initial state.

In the realm of pseudoscalar meson photoproduction in the threshold region, the reaction mechanisms are dominated by a small number of exchanged resonances in the case of π and η mesons. The strangeness production does not show such features: so, one of the main interests in studying this field is to find out the reaction ingredients. A reliable knowledge of the elementary reactions is also needed for further developments in hypernuclei studies via electromagnetic probes. Moreover a good understanding of the photoproduction will allow us to study the electromagnetic form factors of strange hadrons through electroproduction reactions. Finally several QCD-inspired formalisms predict missing baryon resonances, which should be looked for in mesons electromagnetic production, other than the πN channels.

1.4 $K\Lambda$ photoproduction

The first measurements of strangeness photoproduction have been done in the 1960s, while the first models in the ELA formalism were developed in the 1960-70s by Thom [21] and Renard and Renard [22]. They used an effective Lagrangian with the coupling constants adjusted on the existing data. That database was actually limited and with low quality. Besides the extracted values of the coupling constants were lower than the SU(3) predictions and the calculations contemplated a large number of parameters.

Recent measurements of the total and differential cross sections have been accomplished by the SAPHIR collaboration [23, 24, 25]. Though these data put serious constraints on phenomenological approaches, it has been shown that [26, 27, 28] the polarisation observables bear a much stronger selectivity on the reaction mechanism ingredients. It is thus of great interest to measure the polarised beam asymmetry.

The new experiments at CEBAF, ELSA and ESRF/Graal are providing copious data on the kaon electro- and photo-production. A great effort has been done [26, 29, 27] in order to extend the models to different reactions and to photon energies $E_{\gamma_{lab}} \simeq 2.5\ GeV$ by minimization procedures on all the existing data.

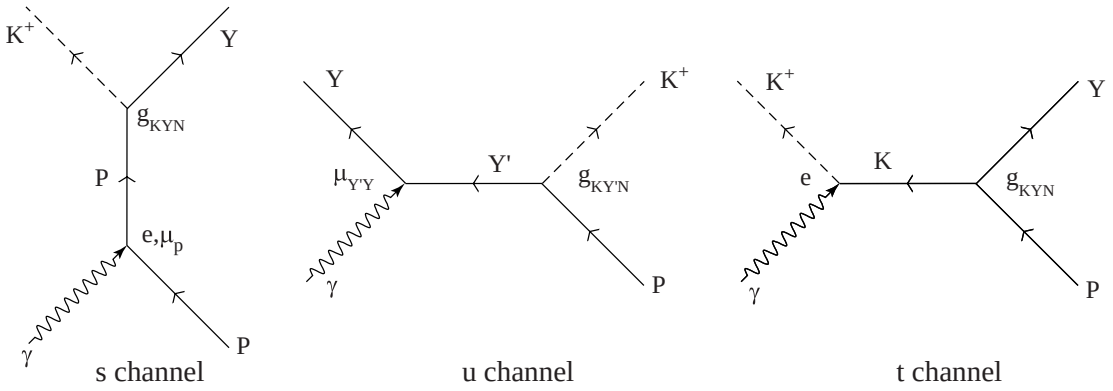

Figure 1.3: *Born terms for the kaon photoproduction with their coupling constant.* $Y = \Sigma, \Lambda, \Xi$

The isobar model has been used [26] in '90 in order to best reproduce the old data from the $K\Lambda$ photoproduction. All the Feynman diagrams for the s, u and t channels of the Born terms (see figure 1.3) and the respective resonances with spin= 1/2 have been considered to calculate the scattering amplitudes of this channel, obtaining this way 4096 possible combinations of state configurations. The combinations have been, hence, minimized on the data with the χ^2_{red} to select the best ones. A further selection was done on the coupling constants, whose values had to be close to the ones expected by the SU(3) predictions. Only two combinations satisfied these conditions and only one was in agreement with the measurement of the target and recoil asymmetry. Besides the Born terms, the best model (called AS) contained the exchange of the following particles: $K^*(892)$, $K1(1280)$,

$N^* = P_{11}(1440)$ and $\Lambda^* = S_{01}(1670)$.

A further improvement of this model have been accomplished with the so called SL model from the Saclay-Lyon collaboration [27]. In the SL model the resonances with spin = 3/2,5/2 have been added to the previous AS model (reported in the previous Section) in the s channel, as required to reproduce data at higher energy. The $\Lambda^*(1405)$ was also added because it is present in the radiative capture of the kaon.

One of the major shortcomings of the ELA is that the propagators for exchanged resonances with spin$> 1/2$ do not have inverse. This situation was cured by the RPI group [19] in the case of the π and η productions. Recently, the Lyon-Saclay-VPI collaboration [28] extended those so-called off-shell treatments to the strangeness production processes. All these formalisms are limited to spin$< 5/2$ resonances.

The recent development of the Saclay-Lyon collaboration (see [30] for a complete picture) includes new improvements concerning the form factors. Up to its latest versions, this model considers only electromagnetic form factors and those of the hyperons are approximated with a nucleonic form factor. Williams et al. [31] have extended the VDM[10] to the Λ and Σ to calculate their form factors. These new form factors are now included in the C model from the Saclay-Lyon collaboration.

The second improvement is on the strong form factors. Up to now, they have been approximated to 1 (point-like particle) because of gauge invariance considerations. Several prescriptions have been suggested to solve this problem. The most comprehensive is the work performed by Davidson and Workman [32]. The authors have shown that the strong form factors can be calculated by adding some counterterms. These strong form factors are now embodied in the Lyon-Saclay formalism.

A different analysis [33] always in the frame of isobar model, includes the Born terms, the K^* and $K1$ resonances in the t channel, the $S_{11}(1650)$, $P_{11}(1710)$ and $P_{13}(1720)$ resonances in the s channel and, finally, a missing resonance, the $D_{13}(1895)$. The authors have shown that this model perfectly reproduces the $K\Lambda$ cross section measured at SAPHIR (see curve "a" in figure 1.4), thus claiming evidence for this missing resonance. Nevertheless, a parallel analysis [5] has shown that the same agreement can be obtained by excluding this missing resonance (curve "b") and including, instead, the off-shell treatment of the $P_{13}(1720)$ spin 3/2 resonance (curve "c"). A good reproduction of the data is also given by including the hyperonic resonances $P_{01}(1810)$ and $P_{03}(1890)$ (curve "d"). Such a result shows how delicate is the determination of the resonances appearing in a given reaction.

[10] Vector Dominance Model

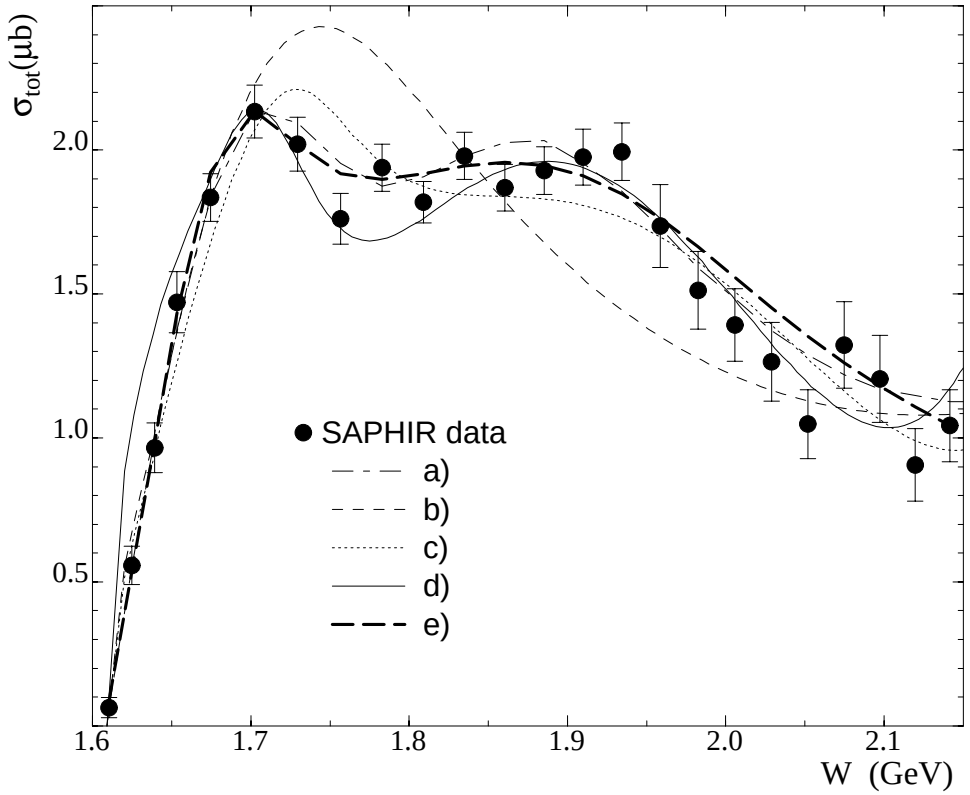

Figure 1.4: *Total cross section for the process $\gamma + p \to \Lambda + K^+$ as function of the center of mass energy. The result is from [24]. We show different fits from different isobar analyses (as explained in the text).*

In the same figure we show as well the prediction of a quark model ([5, 34] curve "e") that is in good agreement with the data.
A further improvement in the resonance identification is thus to measure the polarisation observables as the beam asymmetry.

1.5 The Quark Models

The basis of **Constituent Quark Model** states that quarks are confined by an harmonic or pseudo-harmonic potential which is flavor independent. The constituent quark model (CQM) in its various implementations (non-relativistic, relativized) provides physical insight and is aimed at a global description of both the mass spectrum as well as the structure of hadrons within a common framework. The model predicts a large number of resonant baryon states of light quark (u,d,s). The states fall into supermultiplets with fixed orbital angular momentum and energy excitation level. The mass degeneracy within

one supermultiplet is broken by the color magnetic hyperfine coupling between the quark spins. This hyperfine interaction has been added in the OGE[11] approximation [35] in order to split states with different flavor.

$$V_{qq}(r_{ij}) \;=\; -V(r_{ij})\;\frac{1}{2}\;\overrightarrow{\lambda}_i\;\cdot\;\frac{1}{2}\;\overrightarrow{\lambda}_j$$

where $V(r_{ij})$ does not depend on the flavor and the spin. This way, the hyperfine interaction gives rise to different excited states: for some of them the existence has been partially or completely proved, but there are a lot of excited states which have not been seen so far. They are the so called "missing resonances" [36, 37, 38]. In this context, one of the challenges is, first, to extract mass and width of some resonances with less than four stars (see table 1.1) and, second, to search for these "missing resonances".
The quark model has also been studied [39, 40] in the Chiral Symmetry frame, where the interaction between chiral quarks is described by the effective Lagrangian [41]:

$$L = \bar{\psi}[i\partial^{\mu} + V^{\mu} + \gamma_5 A^{\mu} - m]\psi + ... \tag{1.1}$$

where V^{μ} and A^{μ} are respectively the vectorial and axial currents and $\psi = (\psi(u), \psi(d), \psi(s))$ is the quark field in the SU(3) symmetry. In general, the constant of the confining potential (as the oscillator strength) is linked to the amplitudes of the pseudoscalar meson photoproduction.
A different view of the quark model is going to take shape, the so called **Goldostone Boson Exchange** [42]. High importance, in this theory, is given to the spontaneous breaking of the Chiral Symmetry: the spontaneous breaking means that new particles are created, the so called Goldstone bosons, which are associated to particles with a flavor, where in the OGE theory these last were interpreted by means of the spin-spin interaction.
In the **Bag Model** [43] the quarks are confined in a spherical potential. This choice allows to properly define the quark confinement at low energies. The mesons are explicitly introduced and, in the **Cloudy Bag Model**[44], hadrons are defined as composed by quarks and pions that exchange with each other their masses and angular momentum.
The **Skyrmions Model** [45] describes the hadron interaction in a Lagrangian with an undefined number of colors. As $N_c \rightarrow \infty$ [46, 47] the hadrons are associated to the creation of solitons (Feynman diagrams with only an external leg). This model seems to properly reproduce the mesonic states.

[11] One Gluon Exchange

Chapter 2

A general overview of the apparatus

The Graal[1] facility, installed at the ESRF[2] of Grenoble (France), presents all the features required for the measurement of photoproduction reactions which are characterized by low cross section. The Graal beam is obtained by the backscattering of laser light on high energy electrons circulating in the 6.04 GeV storage ring of the ESRF. This beam has a degree of polarisation up to 0.98 and its energy is tagged with a resolution of a few percent. Compton beams have also the advantage of a rather flat energy spectrum compared to bremsstrahlung beams, which decrease as $1/E_\gamma$, thus reducing the low energy background.
In the first and second sections we will describe the general features of polarised beams and the specific case of the Graal experiment. The third section contains photon beam characterisation in energy, resolution and polarisation and a review of production and monitoring of the experimental set-up. The fourth section is dedicated to the target and the fifth one to the detectors in the experimental hall. The acquisition system is briefly described in the sixth section, while in the last two sections we will describe the procedures for the data preanalysis and simulation.

2.1 Polarised photon facilities

Over the past 30 years photonuclear experiments have not achieved high photon polarisation, high energy resolution and high photon flux at the same time. The turning point was, more recently, a new generation of electron accelerators and photon beams, characterised by high flux ($\approx\ 10^7\ s^{-1}$), high energy resolution (a few MeV), and promises of

[1] Grenoble Anneau Accelerator Laser
[2] European Synchrotron Radiation Facility

high polarisation. Table 2.1 displays the main features for a number of polarised photon facilities.

Facility	laser	λ(nm)	E_e(GeV)	E_γ^{max}(MeV)	Flux (γ/s)
Lebedev (1964)	Rubis	694.3	0.6	7	10^2
CEA[a] (1965)	Rubis	694.3	6.0	400	10^2
SLAC[b] (1969-74)	Rubis	694.3	15.6	4660	10^3
SLAC (1980-83)	Nd-YAG	266.0	30.0	20000	10^3
LNF[c] (1978-90)	Ar-Ion	488.0	1.5	80	10^5
BNL[d] (1988-)	Ar-Ion	351.1	2.5	370	10^7
VEPP[e] (1988-)	Ar-Ion	514.5	2.0	140	10^6
ESRF (1995-)	Ar-Ion	351.1	6.0	1500	2.10^6
SPring-8 (2001-)	Ar	351	8.0	2400	$2.5\ 10^6$

[a]Cambridge Electron Accelerator.
[b]Stanford Linear Accelerator Center.
[c]Laboratori Nazionali di Frascati.
[d]Brookhaven National Laboratories
[e]Novosibirsk.

Table 2.1: *Chief characteristics of polarised photon facilities*

Although there is some overlap among these facilities, many of their programs are complementary and provide a vigorous attack on many key physics issues.
The main methods to produce polarised photon beams are bremsstrahlung radiation and Compton backscattering. High photon fluxes are easily produced by the bremsstrahlung of electrons in a high-Z radiator. These γ rays have an energy distribution of $1/E_\gamma$, namely a high concentration at low energy. The real difficulties are associated with the production of polarised electrons. Impressive results have been obtained at SLAC[48] and successfully duplicated at Mainz[49] and at LADON[50]. Finally, the coherent bremsstrahlung of electrons in single crystals such as diamond and silicon has also been used to produce linear polarisation.

2.2 The ESRF and the Graal facility

The ESRF storage ring has been designed to produce synchrotron radiation for the study of matter properties, ranging from crystals, semiconductors to proteins and cells. When the ESRF was originally proposed it was immediately evident that its high energy and

low emittance would have made it the best machine to produce Compton backscattering γ ray beams.

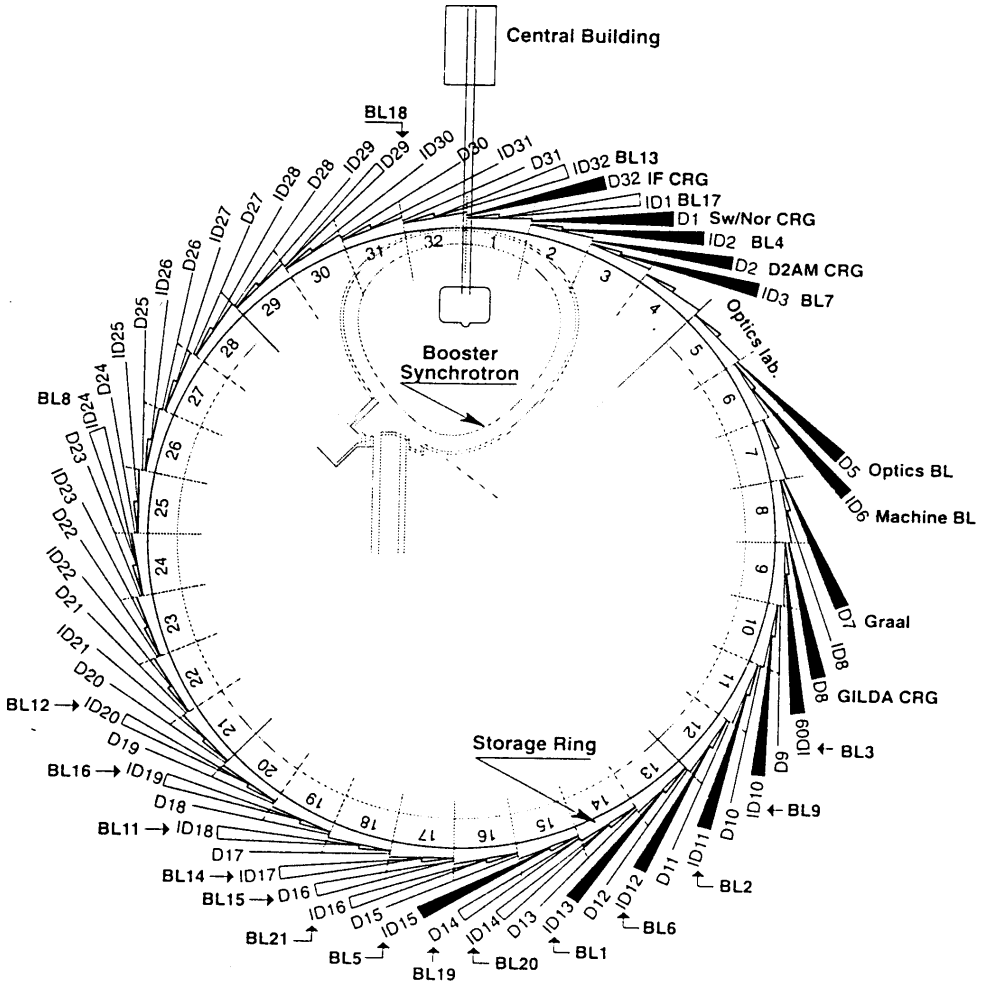

Figure 2.1: *Schematic view of synchrotron radiation facility of Grenoble (France)*

The ESRF is composed of a linear injection system, providing an acceleration up to 200 MeV, a synchrotron (300 m of circumference) for the acceleration up to $\approx 6\ GeV$, and a 854 m circumference storage ring, divided into 64 straight sections joined by magnetic dipoles. The goal is to produce a high brilliance and low dispersion beam by optimizing the electrons intensity and emittance. The result is an electron current, circulating in ultra-high vacuum ($10^{-10}\ Torr$), between 150 and 200 mA with a time of life of about 50 hours and very small dimensions of the order of some hundreds μm.

The electrons circulate in bunches $65-140\ ps$ long, spaced according to different operating modes (single bunch, 16 bunches, 2/3 bunches) and the bunch spacing is function of the

frequency of the resonance cavities (352 MHz).
The basic cell of the ESRF (1/16 of the storage ring) consists of four straight lines: a short one (6.5 m, called D line), a long one (18 m, called ID), a D again and, finally, another ID line. The long straight sections are dispersion-free and, at their center, there can be only a low betatron wavelength β for the insertion of a wiggler or a high β for the insertion of an undulator. The synchrotron radiation is produced in the dipoles and with wigglers and undulators, situated in the straight sections. The Graal experiment does not use the synchrotron radiation but the electron beam to produce a high energy γ beam by the Compton backscattering. Synchrotron radiation is therefore harmful for the Graal experiment, because it can damage the detectors and the optics.

2.3 The γ beam

2.3.1 Characteristics of the Compton scattering

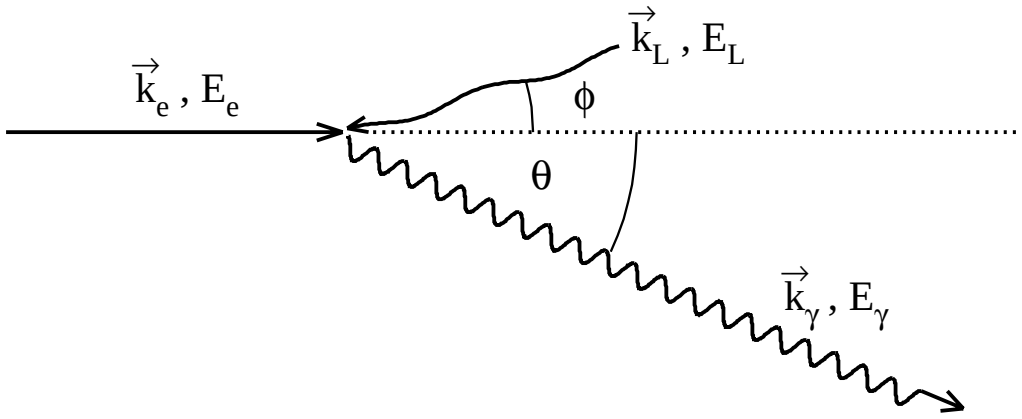

Figure 2.2: *Kinematics of the reaction* $\gamma + e^- \rightarrow \gamma + e^-$

If a laser photon of energy E_L strikes a relativistic electron of energy E_e with a relative angle close to 180°, as in figure 2.2, it is scattered in the backward direction inside a narrow cone, with angle θ. If ϕ and $\theta_1 = -(\phi + \theta)$ are respectively the values of the laser scattering angles with respect to the incoming electron and the γ beam, the energy of the final photon E_γ is

$$E_\gamma = E_L \frac{1 - \beta cos\phi}{1 - \beta cos\theta + (E_L/E_e)(1 - cos\theta_1)} \tag{2.1}$$

where β is the electron velocity in units of the speed of light c. If we consider relativistic electron sources, the following approximations hold: $\gamma = E_e/m >> 1$, $\beta \simeq 1$, $\theta_1 \simeq 180^\circ$ and $\theta << 1$; the relation (2.1) may then be rewritten as follows, neglecting the very weak dependence upon ϕ (if $\phi = 1^\circ$, a very high value compared to the electron and laser beam alignment[3], the energy variation of the gamma beam is about 20 keV):

$$E_\gamma = \frac{4\gamma^2 E_L}{1 + \frac{4\gamma E_L}{mc^2} + \theta^2\gamma^2} \tag{2.2}$$

For a fixed laser line and electron beam energy, the maximum energy of the scattered photon (Compton edge), $E_{\gamma_{max}}$, is obtained at $\theta = 0$ and it is given by the following relation:

$$E_{\gamma_{max}} = E_e \frac{z}{1+z} = \frac{4}{m^2}\frac{E_e^2 E_L}{(1+z)} \tag{2.3}$$

where $z = 4(E_e E_L/m^2)$. For UV laser lines ($\approx 351nm$) one obtains $E_{\gamma_{max}} = 1,47\ GeV$. The maximum scattering angle in the laboratory system is $\theta \approx 500\ \mu rad$ corresponding to about 3 cm at a distance of 35 m.

The energy spectrum of the outcoming photon beam is given by the differential cross-section for the Compton scattering in the laboratory frame:

$$\frac{d\sigma}{d\Omega} = \frac{2r_0^2}{m^2\kappa_1^2} \cdot F \cdot E_L^2\ , \tag{2.4}$$

where $r_0 = 2,818\ fm$ is the classical electron radius and F is:

$$F = 4\left(\frac{1}{\kappa_1} + \frac{1}{\kappa_2}\right)^2 - 4\left(\frac{1}{\kappa_1} + \frac{1}{\kappa_2}\right) - \left(\frac{\kappa_1}{\kappa_2} + \frac{\kappa_2}{\kappa_1}\right)$$

If $\phi = 0$, κ_1 and κ_2 are given by:

$$\kappa_1 = -\frac{4\gamma E_L}{m} \quad ; \quad \kappa_2 = \frac{\gamma E_\gamma}{m}\left(\theta^2 + \frac{1}{\gamma^2}\right)$$

If the electron is relativistic, as in the Graal case, its helicity is conserved. Thus, the degree of polarisation P_γ of the scattered photons is proportional to laser beam one. P_γ depends on the scattering angles θ' and φ' in the electron frame and its value is averaged over φ'. This way, if P_L^L is the linear polarisation of the laser:

$$P_\gamma^L = \frac{(1-\cos\theta')^2}{2F'} \cdot P_L^L \tag{2.5}$$

[3] $\phi \approx 0.2^\circ$, by considering the alignment procedure used

where F' and θ' are given by:

$$F' = \kappa + \kappa^{-1} - \sin^2\theta' \qquad \kappa = 1 + 2\gamma\frac{E_L}{m}(1-\cos\theta')$$

$$\cos\theta' = \frac{1 - E_\gamma/E_{e-} - E_\gamma/[E_L\gamma^2(1+\beta^2)]}{\beta^2 - E_\gamma/E_{e-}}$$

In figure 2.3 the energy spectrum and the polarisation are shown for different laser energy with $P_L^L = 100\%$ and a constant total flux of 10^6 γ/s.

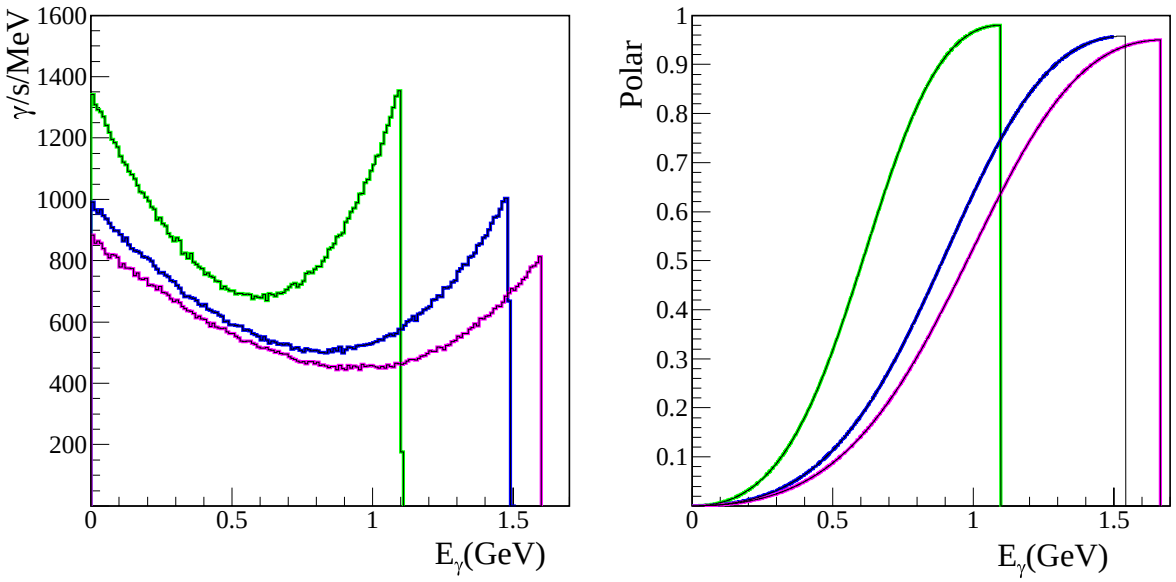

Figure 2.3: *Distribution of the differential flux (left) and linear polarisation (right) for an electron beam energy $E_e = 6$ GeV and for different laser energies (515, 351 and* 300 *nm), as function of the Compton photon energy.*

2.3.2 Beamline set-up

Figure 2.4 displays an overview of all the experimental set-up. The collinearity between the laser and the electrons is achieved thanks to a vacuum line of 30 m of length. The pressure is maintained at about 10^{-10} $Torr$ in order to match the vacuum of the storage ring. The laser cabin is along the tunnel wall, 25 m from the interaction region, and contains all the necessary optics for the alignment and focusing.

The laser and its optics are situated inside the laser cabin on an optical bench. The laser is an Innova 200 Argon-Ion with an output of 12 W on green 512 nm line, 7 W on the UV $340-350$ nm interval and 3 W in the UV $320-330$ nm region. A Brewster window polarises the photons in the vertical direction inside the laser cavity. The virtual waist

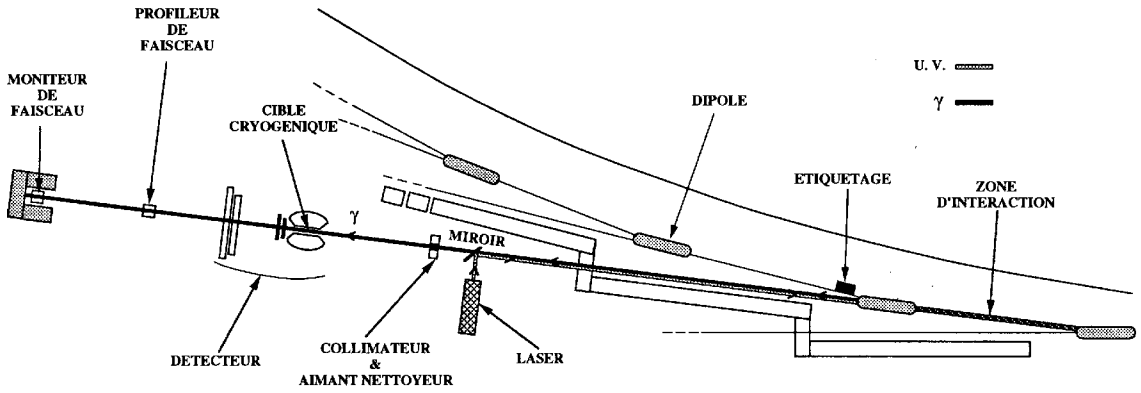

Figure 2.4: *Schematic layout of the Graal beam and its experimental set-up.*

(2 m far in the backward direction with respect to the laser) is 300 μm in diameter. The optics, as shown in figure 2.5 consists of:

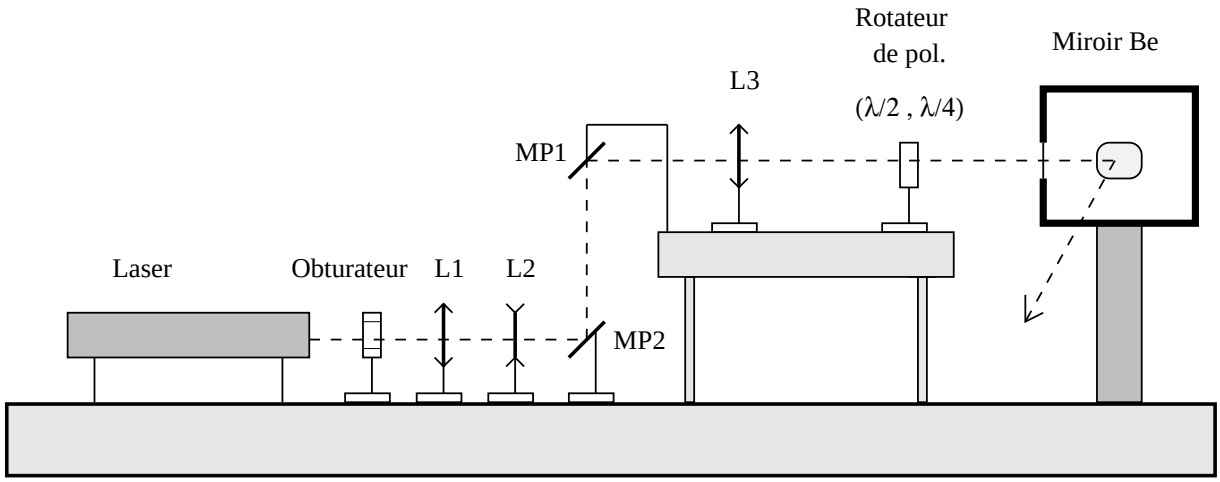

Figure 2.5: *Structure of the optical bench.*

1. a system of three lenses (L1, L2 and L3), in practice a zoom, which allows to change the position and size of the laser waist in the interaction region. This way a waist of about 1 mm is obtained in the interaction region;

2. a polarisation rotator that can either change the orientation of linear polarisation ($\lambda/2$) or transform it in circular polarisation ($\lambda/4$);

3. the periscope: a set of two mirrors, MP1 and MP2, where the orientation of the latter can be controlled with a μrad precision, to reach the superposition of the laser and electron beams in the intersection region;

4. a vacuum window to allow the laser light into the machine vacuum system;

5. a fixed beryllium mirror to deviate (90°) the laser light in the direction of the intersection region. The beryllium was chosen for its low Z since it is crossed by the gamma-rays of our beam .The X ray radiation emitted in the bending magnets of the accelerator may warm up and damage the mirror. These X rays come from the bending magnets which precede and follow the straight section of the intersection: their distribution is thus decentralized with respect to the γ beam and localized in a horizontal plane. It can be almost completely eliminated by two copper "fingers";

The high energy photons travel backwards in the vacuum line, they go through the beryllium mirror, the stainless window and, finally, enter the experimental hall where they come across a 20 cm long lead collimator: the γ beam is hence at the most $12 \times 15\ mm^2$ large. A magnet cleans the beam from the electrons and positrons created by the collimator and finally the photons reach the target through a vacuum pipe ($10^{-5}\ Torr$).
Our simulation shows that this collimator does not affect the polarisation of the γ beam. In addition the optics of the laser line must preserve the laser polarisation as much as possible: the entrance window on the beam line and the beryllium mirror can in fact deteriorate the laser polarisation due to X ray radiation damage on these elements. The laser polarisation was, therefore, measured at the output of the beamline (after the intersection with the electron beam) and its value is[4]:

$$P_L = 0.98 \pm 0.02\% \tag{2.6}$$

2.3.3 Beam energy and resolution

The energy of the Compton photon can be worked out once the energy of the recoil electron is known. It is calculated from the position of the scattered electron measured by the TAGGING detector situated after the bending magnet. The energy of these electrons is lower than the energy of non scattered electrons and they substantially deviate from the main beam trajectory as shown in figure 2.6.

[4]The Stokes parameters have been recently measured and it has been observed that the laser light is not 100% linearly polarised, but slightly elliptical. This effect is negligible for the linear polarisation itself but it might affect the circular polarisation experiments which are foreseen.

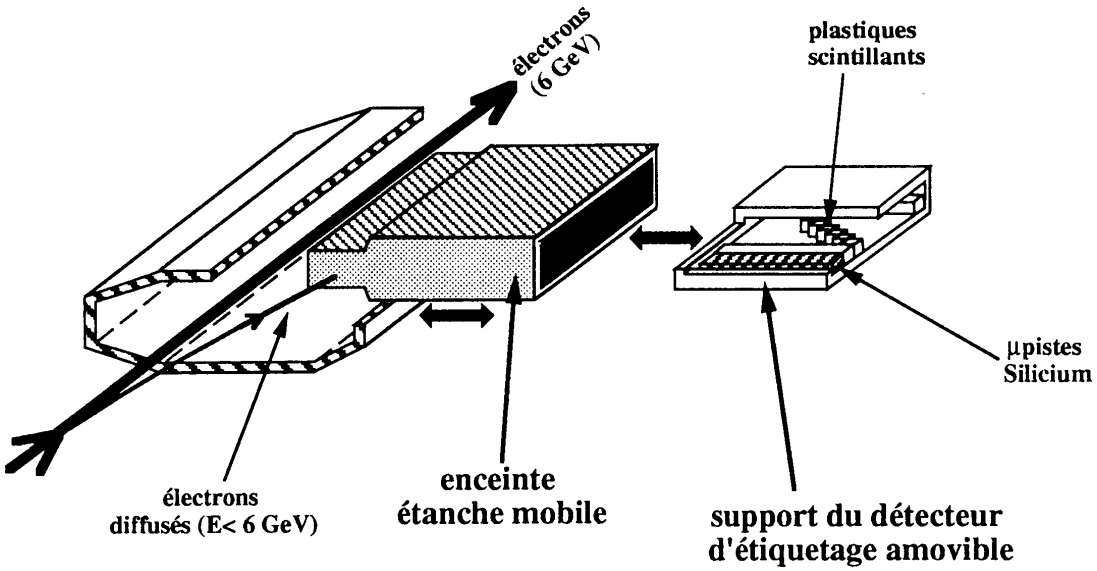

Figure 2.6: *Schematic view of the TAGGING detector.*

The TAGGING detector is inserted in the storage ring, just after the magnet, inside a movable box (represented figure 2.6). The box is hermetically shielded by 4 mm of tungsten in order to suppress almost 100% of the X ray background.

The detection device is inclosed inside a 14 mm heigh and 10 cm wide (along the beam direction) box and consists of two detectors:

- a set of 128 silicon μstrips, where the electrons release about 100 keV. This set-up gives a precise measurement of the position, i.e. an energy resolution of about 16 MeV limited by the emittance of the electron beam;

- 10 plastic scintillators, where the electrons release about 1 MeV. Two long scintillators cover the whole detection zone while eight small ones are placed side by side and each of them covers a small zone of detection (about 60 MeV).

The **experiment trigger** is given by the coincidence between the two long plastic scintillators and at least one among the shorter ones. The gate of this coincidence is 300 ps large and allows to select the right electron bunch using a coincidence with the Radio-Frequency of the ESRF. This trigger allows a time of flight precision of the order of 50 ps for all the detectors. Finally the coincidence is also useful to eliminate the X-rays.

E_γ determination

The relationship between the γ energy and the electron position x_{e^-} on the TAGGING detector is given by:

$$\begin{aligned} E_\gamma = & \quad \frac{x_{e^-} E_{e^-}}{a_0 + x_{e^-}} & \text{where} \\ a_o = & \quad 159,9 \pm 0,3\ mm & \text{is a number dependent on} \\ & & \text{the longitudinal position of the TAGGING} \\ E_{e^-} = & \quad 6030.6 \pm 6\ MeV & \text{is the electron energy } E_{e^-} \end{aligned} \tag{2.7}$$

The electron energy has been deduced from the threshold of the η photoproduction [51]. The x_{e^-} value is linearly dependent on the μstrip number:

$$x_{e^-} = (x_{\mu st} - 0,5) \cdot d + x_{OFF} \tag{2.8}$$

where $d = 0.3\ mm$ is the μstrip width and x_{OFF} the position of the first strip.

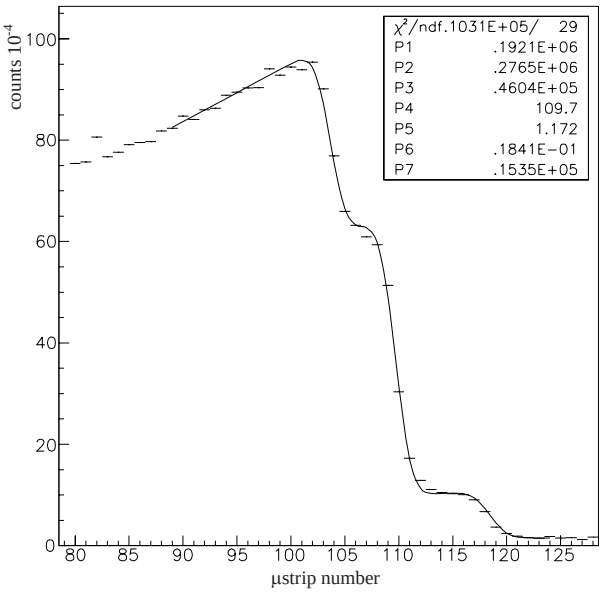

Figure 2.7: *Compton edge on the µstrip detector. There are three groups of different laser lines that gives three different Compton edges.*

The measurement of the Compton edge gives as well an estimation of the energy resolution of the γ beam: when the UV lines of the laser are used , six different lines contribute to the Compton edge as shown in figure 2.7. These lines are: $363.4, [351.4, 351.1], [320, ..., ...]\ nm$

and, by considering the energy resolution, they show up as three groups, which can be observed on the experimental Compton edge in this figure. From the fit the energy resolution is $\sigma_{E_\gamma} = 6.8\ MeV$ corresponding to a FWHM of 16 MeV.

2.3.4 Beam monitoring

The number of photons on the target is monitored by two different detectors positioned at the end of the beam line:
-the **Spaghetti monitor** is a calorimeter for the detection of electromagnetic showers. It is a sandwich of scintillating fibers and lead. It is $10 \times 10\ cm^2$ in section, 60 cm deep, 99% of the electromagnetic shower is contained inside the detector, which has 100% efficiency. At low beam intensities the energy resolution for the photons is $\approx 30\%$ but pile-up effects occur when the γ fluxes are greater than $10^6\ \gamma/s$, distorting the counting rate.
-the **thin monitor**, situated in front of the *spaghetti* is used to measure fluxes up to $10^7\ \gamma/s$. It is composed of three plastic scintillators (5 mm thick) with a square surface of $12 \times 12\ cm^2$. An aluminum sheet (2 mm thick) is placed amid the two first scintillators, in order to convert photons into electron-positron pairs. The photon is thus identified by the coincidence between the second and the third scintillator in anticoincidence with the first one. This way, the counting rate of the thin monitor is limited at about $10^6\ Hz$ and pile-up is negligible. The efficiency has been carefully estimated [51] and is $\epsilon_{MON} = 2.592 \pm 0.005\%$.

2.4 The target

The target is fixed on the beam axis, 25 m far from the interaction region. It is composed of liquid hydrogen (H_2), contained in a Mylar cell of three possible different lengths ($3, 6, 12\ cm$) and 4 cm diameter. Other types of liquids can be used as medium (D_2, ^3He and ^4He).
A cryostat (whose description is reported in [52]), working with Helium cycles, lowers the cell temperature. When the cell is filled up the working temperature of the liquid hydrogen is 18 K and the density is $\rho = 70,8 \cdot 10^{-3}\ g/cm^3$. The total thickness of the three mylar caps is 21 μm ($\rho = 1,39\ g/cm^3$). In the first stage of the Graal program (π°, η channels) 3 and 6 cm targets were used. This way, the uncertainty on the polar and the azimuthal coordinates of the charged particles is only slightly affected by the target dimension. The new experiments ($K\Lambda, \omega N$ channels) require now high statistics and a

longer target (6 or 12 cm). The cylindrical chambers are therefore essential to reconstruct the angles of the charged particles (with high resolution). This thesis deals with data and simulation analysis on 6 cm target.

2.5 The LAGRANγE detector

The 4π detector LAGRANγE[5], for the detection of neutral and charged particles, has been conceived to reconstruct the kinematics for reactions with a center of mass energy from ≈ 1.3 to ≈ 1.9 GeV.

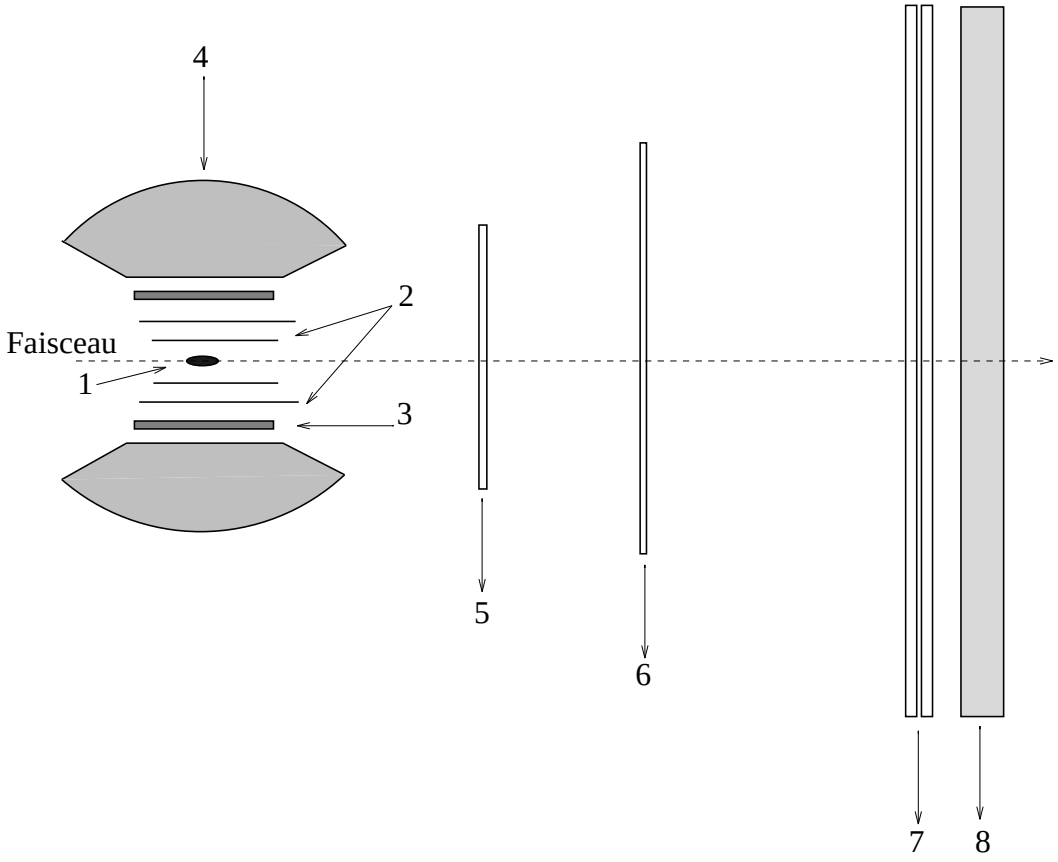

Figure 2.8: *Schematic view of the LAGRANγE detector:*
1- *Target* 2- *Cylindrical MWPCs* 3- *barrel of plastic scintillators* 4- *BGO calorimeter* 5 *and* 6- *Planes MWPCs* 7- *Scintillator hodoscope* 8- *shower detector.*

The detector, as shown in figure 2.8, consists of a cylindrical central part and a set of forward detectors. The particles emitted in the central part at angles between 25° and

[5]**L**arge **A**cceptance **GR**AAL **A**pparatus for **N**uclear γ **E**xperiments.

155° with respect to the beam axis, pass through two coaxial cylindrical MWPCs (2), a barrel made of 32 plastic scintillators (3), that provides ΔE information for particle identification, and the BGO ball (4) made of 480 $Bi_4Ge_3O_{12}$ crystals.
The particles emitted in the forward direction at polar angles less than 25° pass through two plane wire chambers (5,6) and a double wall of plastic scintillators (7), covering an area of $3 \times 3\ m^2$ and located 3 m far from the target. It is followed by a shower detector (8) consisting of 16 vertical modules (lead/scintillator sandwiches) covering the same area as the double plastic wall.

2.5.1 The electromagnetic calorimeter

The BGO calorimeter (4) measures the energy of charged and neutral particles with different efficiencies and resolutions. The calorimeter is composed of 480 crystals, 15 in θ and 32 in ϕ. The crystals are 24 cm long (21 radiation lengths), for a good confinement of the photon shower in the GeV region, and are arranged in such a way that the reaction products, emitted in all directions from the target center, encounter a constant thickness of BGO. They are housed in 24 carbon fiber baskets; each of them is divided into 20 cells, to keep the crystals optically and mechanically separated. The internal walls are 0.38 mm thick, while the external ones are 0.54 mm thick. A cylindrical hole of 20.3 cm diameter along the beam axis allows the insertion of the target, the plastic scintillators and the cylindrical MWPCs.
The accuracy and reliability of the energy calibration is a basic requirement for this detector, in which both crystals and photomultipliers contribute to obtain high energy resolution. The gain variations of all sectors have been monitored as a function of time, thus ensuring uniformity of response during data taking and keeping to a minimum the time spent in calibrating the calorimeter. The whole procedure is reported in [53].
The BGO light output is known to decrease with increasing temperature. Since a thermostatic regulator of the calorimeter is not possible due to its compact geometry, it was necessary to keep under control the crystal temperature in order to estimate the possible variations of the energy calibration; the whole system is described [54]. Nevertheless the existence of an air conditioning system for the whole laboratory, limits room temperature variations to $2 - 3°$. The thermal contribution to the total energy resolution is about $\mathcal{F}_T \simeq 0.4\%$. The total energy resolution is [55]:

$$\Gamma(FWHM) = \sqrt{a^2 + \left(\frac{b}{E_\gamma}\right)^2 + \left(\frac{c}{\sqrt{E_\gamma}}\right)^2} \simeq 2\%$$

where $a = 0.17$ is a constant term, $b = 0.97$ is the noise and $c = 2.36$ is the statistical term. The constant term a includes the fluctuations in the energy leakage, the non-uniformities in the crystal response, the intercalibration uncertainties and the thermal term evaluated with the temperature control system.
When a photon strikes the calorimeter it produces an electromagnetic shower that is absorbed 99% in the detector, 90% being absorbed by the crystal at the center of the shower. The cluster center, identified with the center of gravity method, gives the following resolutions for the photon angles:

$$\mathcal{F}_\theta = 6^\circ \text{ et } \mathcal{F}_\varphi = 7^\circ \ (E_\gamma > 200\ MeV)$$

Hadrons can also be detected by the BGO via nuclear reactions. In this case the efficiency is much lower (about 20%) and it strongly depends on the hadron energy. The best angular resolution for the low energy protons is 10°.

2.5.2 The track detectors

The track detection of charged particles is achieved by four MWPC[6] (2,5,6). Two of them are in the forward direction and two in the central one. The double measurement of the position allows to calculate the polar and azimuthal position of the particle.

Plane chambers (5,6)

Each chamber is composed of two planes of wires (3 mm distance between two wires) with perpendicular directions (see figure 2.9). The first chamber has the wires oriented in the x, y direction while the second in the u, v direction (at 45° with respect to the x, y plane) in order to resolve the ambiguities when more than one particle goes through the chambers.
The chambers are respectively 93.2 and 133.2 cm far from the target center. Each plane, as shown in figure 2.9 is composed of gilt tungsten wires, placed between aluminized mylar cathodes. The dimensions are given in table 2.2. The space within each cathode (10 mm) is filled in with an Argon-Ethane mixture (85 and 15%, respectively). A 2400 V voltage is applied to the wires. Under these conditions the efficiency is close to 100% [56] and the position resolution is comparable to the wire distance.
The angular limit of the plane chambers is $\theta < 21^\circ$. Since the lower limit of the cylindrical chambers is $\theta > 25^\circ$, there is a small angular region that is not covered by the detectors.

[6]MultiWire Proportional Chamber

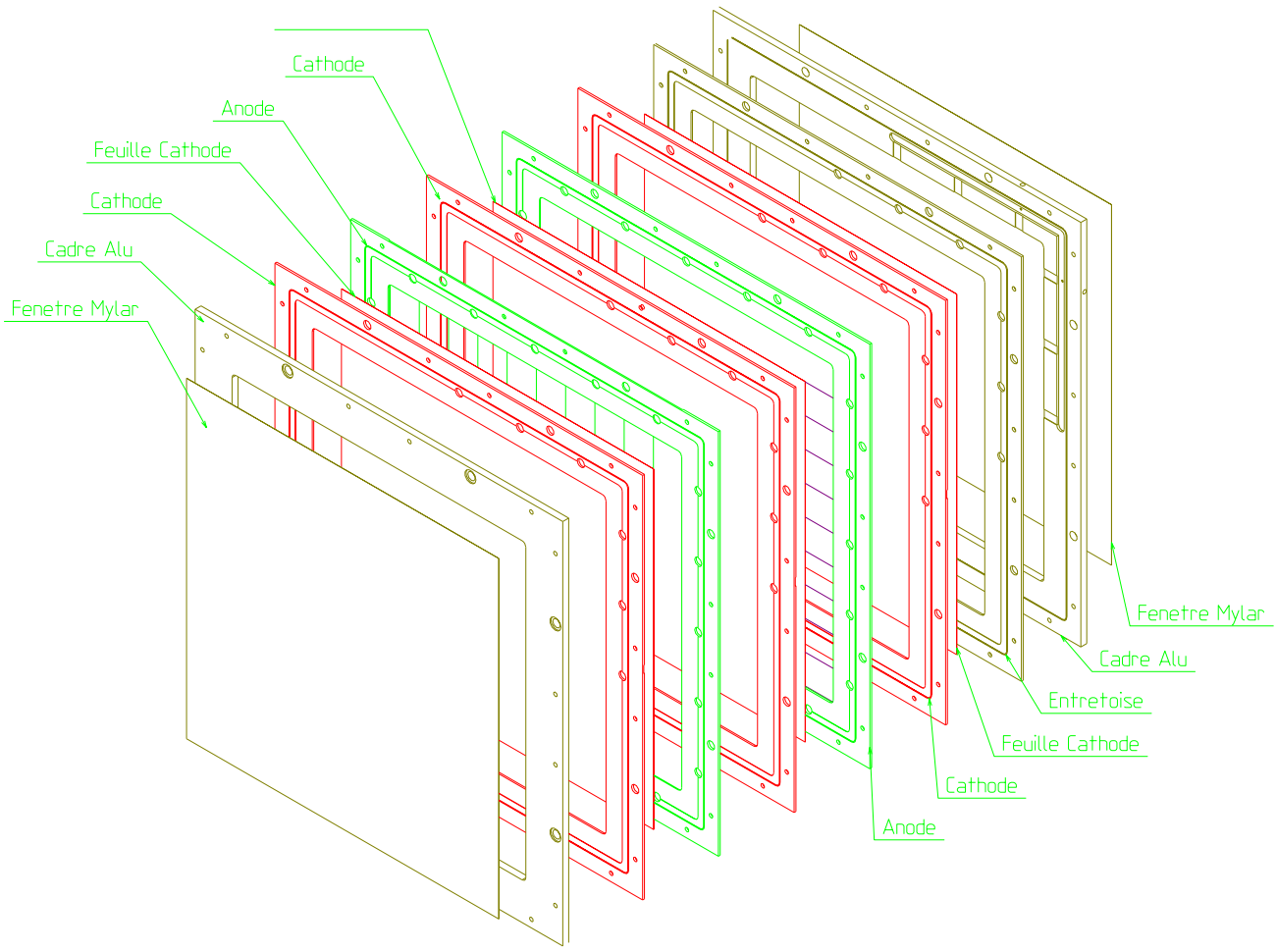

Figure 2.9: *Schematic view of one plane MWPC.*

	Chamber 1	Chamber 2
Surface of the wire plane	$960 \times 960\ mm^2$	$1152 \times 1152\ mm^2$
Number of wires	320×320	384×384
Distance between wires	$3\ mm$	$3\ mm$

Table 2.2: *Geometrical dimensions of the plane chambers.*

The cylindrical chambers (2) together with their efficiencies and the optimization of their software analysis is one of the main parts of this thesis and they will be therefore treated in the following chapter.

2.5.3 The charged particle detectors

The scintillator hodoscope (7)

A $3 \times 3\ m^2$ plastic scintillators wall identifies charged particles in the forward direction. The wall is made up by two series of 26 scintillator bars, respectively vertically and horizontally oriented, and it measures the time of flight on a 3 m distance. The bars are composed of NE110A and they are 11.5 cm wide and 3 cm thick. The time of flight resolution is $\mathcal{F}_{ToF} = 600\ ps$ for the detection of ultrarelativistic electrons or positrons. The detection efficiency is 100% if the particle energy is greater than a few MeV. An accurate description of the wall is given in [52].

The barrel of plastic scintillators (3)

A cylinder of 32 bars of plastic scintillator (NE110A) is installed between the cylindrical chambers (3) and the calorimeter (4). Each bar is 43.4 cm long, with a trapezoidal section ($h = 18\ mm$, $H = 19\ mm$). The bars are housed, four by four in a carbon fiber structure 0.5 mm thick. Each bar covers an azimuthal section of the calorimeter. The internal diameter of the barrel is 9.4 cm. The scintillators are 5 mm thick and they identify charged particles by energy loss measurement. Moreover the coincidence with the BGO allows the separation of neutral and charged clusters in the calorimeter.

2.5.4 The shower wall

A large acceptance lead-scintillator time-of-flight wall (8) has been installed to detect photons and neutrons. The time-of-flight resolution is $\mathcal{F}_{tof} \simeq 600\ ps$ and the position resolution is $\mathcal{F}_{pos} \simeq 11 - 18\ cm$. The wall is an assembly of 16 modules, mounted vertically and covering all together a sensitive area of $3 \times 3\ m^2$. The modules, aligned with respect to the beam are fixed 3.3 m from the target. Two central modules have half-circle holes (9 cm diameter) for the beam passage. Each module is a composition of four $4 \times 19 \times 300\ cm^3$ scintillator bars, separated by 3 layers 3 mm thick of lead converter. The efficiency of the neutron detection has been evaluated with the simulation: the neutron efficiency is about 22% for a 10 MeV threshold. A photon efficiency of 92-95% was obtained in a similar way. A detailed description of the shower wall and its features is reported in [57].

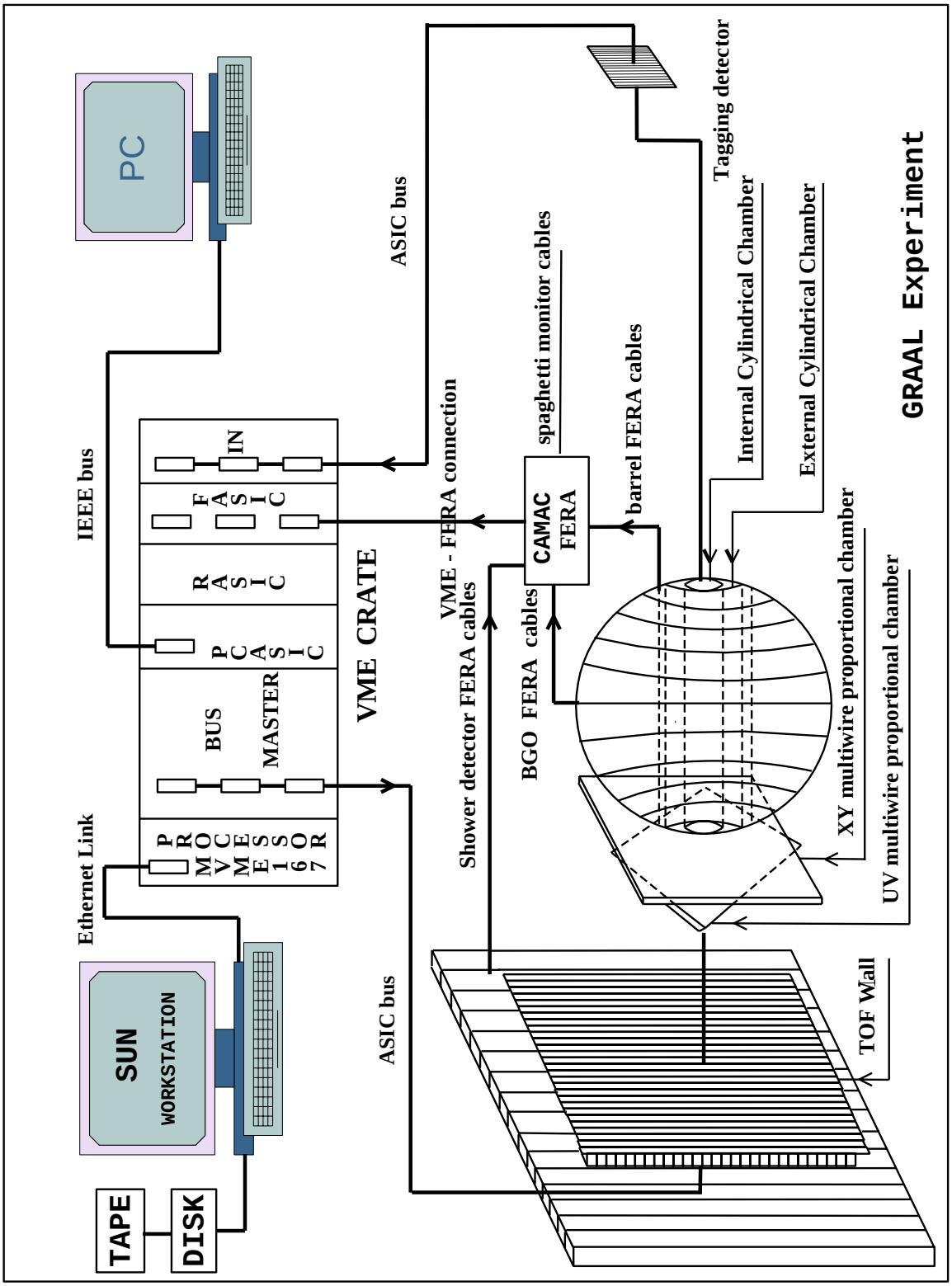

Figure 2.10: *Overview of the Graal experiment and its specific data acquisition system.*

2.6 Acquisition system

The Graal experiment scheme of the acquisition system (SAGA[7][58]) is shown in figure 2.10. Its main feature is a hardware event builder which associates compact and programmable ASIC[8] type electronics and standard electronics read by a FERA[9] bus.
ASIC circuits permit analog to digital signal processing for many types of particle detectors, such as anode wires and cathode strips of MWPCs, photomultipliers and drift chambers. The electronics is directly placed on boards and connected to the detector in order to reduce the number of interconnections and, therefore, the risk of failure due to connectors. The data transfer is performed by a 32 bit ECL bus, linking all the detectors. A SUN workstation controls all the detector settings by the ASIC bus. Once the buffer is transferred in the shared SUN memory, it can be recorded on tapes (10 *Gbyte* of size) or processed by the spectra building program, running on the station.
Six of the twelve detectors are controlled by the FERA electronic system. Their calibration and monitoring is performed by a traditional CAMAC system on an Alpha station, operating with VMS. The FERA bus is read by the ASIC bus through the FASIC module. A C program has been written to set the parameters of electronic modules (thresholds, delays, amplitudes, widths, channel connection on an oscilloscope, etc.) located on the different boards. It runs on the SUN station with a powerful graphical interface called SL-GMS.
The data acquisition time depends on the largest conversion time (4 μs for the audio converter), on the bus speed (5 ns/m) multiplied by two VME periods (125 ns). For about 100 events this time amount at 17.5 μs, giving, this way, a transfer rate of about 23 $Mbyte/s$, that has to be compared to the ETHERNET transfer limit (600 $Kbyte/s$). The trigger frequency being about 200 Hz, the number of lost events is thus negligible.

The trigger system

The acquisition system is composed of different triggers, which come from either physical or beam events. All of them are in coincidence with the TAGGING detector.
An energy deposition in the BGO larger than 200 MeV in coincidence with an electron in the TAGGING detector, triggers the data acquisition for the physical event. This energy threshold eliminates almost all the electromagnetic background radiating from the target. This trigger is used for the meson photoprodution that decays into photons.

[7] **S**ystème **A**cquisition **G**raal **A**sic
[8] **A**pplication **S**pecific **I**ntegrated **C**ircuit.
[9] **F**ast **E**ncode **R**eadout **A**DC.

Channels with three charged particles are triggered by the following condition: at least two particles in the forward hodoscope and at least one particle in the central barrel. This trigger allows to study the photoprodution of strange mesons ($K\Lambda$ et $K\Sigma$) as well as the charged decay of other mesons (η, ω).
Two other triggers rule the beam acquisition: the first is the coincidence between the second and third scintillators of the thin monitor in anticoincidence with the first one. The second is an energy threshold on the *spaghetti*. Another trigger starts events with the thin monitor and *spaghetti* coincidence. These triggers allow to calculate the monitor efficiency and the beam flux.

Data taking

Each period of data taking is divided into runs. The run length is four hours long, depending on the trigger and on the intensity of laser line. Each run is measured by alternating the two laser states with the bremsstrahlung mode. The actual timing is about 20' for each polarisation and 5' for bremsstrahlung.
For each trigger and each polarisation or Bremsstrahlung state the acquisition records on a module of scales the total number of events. In particular the monitor, *spaghetti* and time scales are read to calculate the beam flux for each polarisation and Breemsstrahlung state.
The maximum flux is limited by the ESRF. In fact the loss of electron beam life time due to Compton backscattering may never exceed 20% of the electron time of life.
The run are hence recorded on tapes with the IN2P3 binary format. The program **decode** digitises these information in a CWN[10] structure, which can be used by the PAW[11] software. At this point the calibration and control files of each detector are created and the run is ready to be processed by the preanalysis program.

2.7 Data preanalysis

Figure 2.11 displays the flow chart of the programs used by the collaboration to process simulated and real data. The structure was designed in order to have the same type of analysis (starting from the program **prean**) for both real and simulated data. The **prean** program receives digital outputs (ADC, TDC, signals from MWPCs,...) and transforms them into physical quantities. The number of charged tracks in the MWPCs is calculated

[10]Column Wise Ntuple
[11]Physics Analysis Workstation

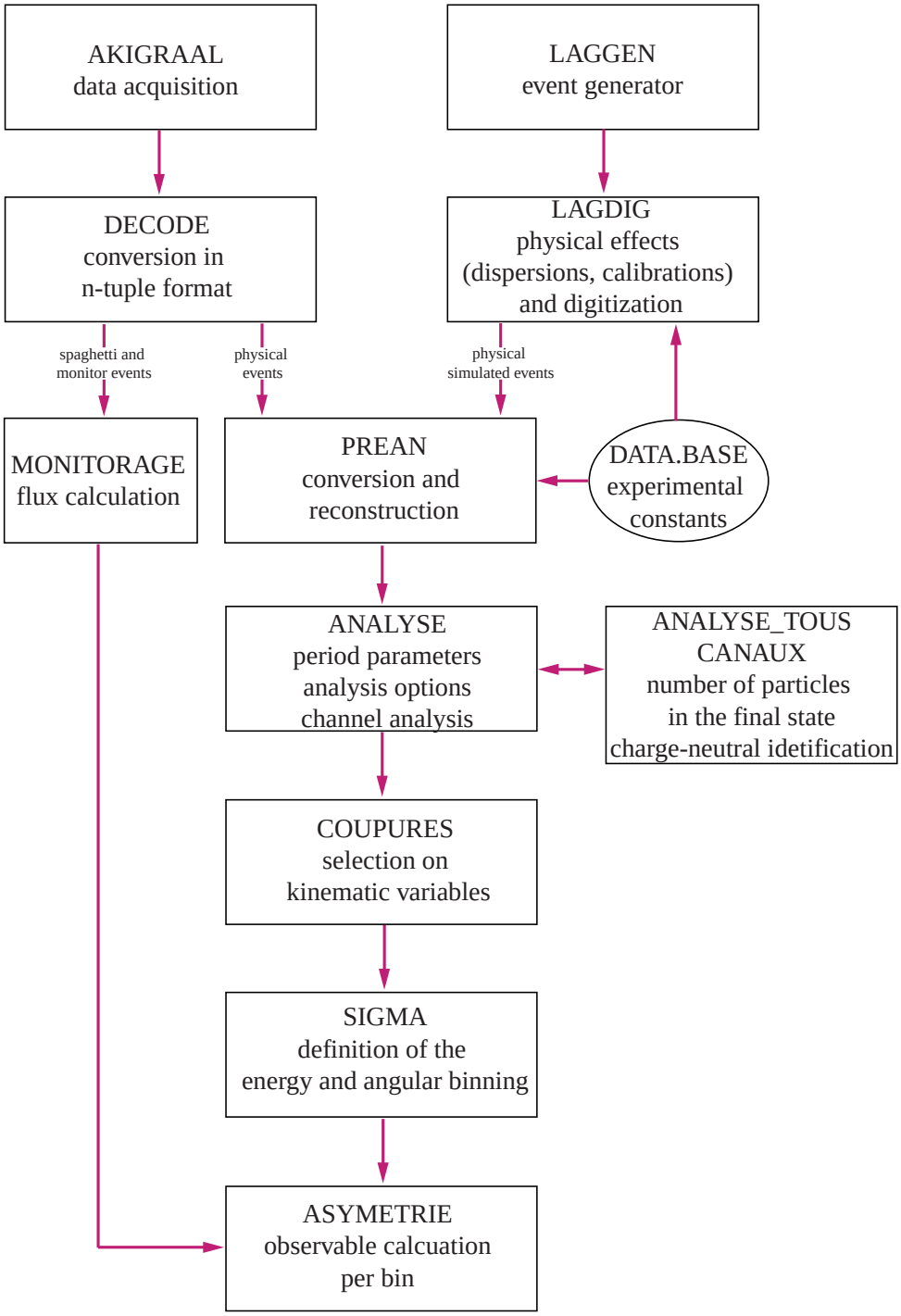

Figure 2.11: *Flow chart of the program used for the treatment of simulated and real data.*

together with their energy loss in the hodoscope or barrel and any energy released in the calorimeters (shower or BGO). Neutral particles are classified with their angles and energies measured by the calorimeters. The **analysis** program reads the output of **prean**

and its structure will be described in the dedicated chapter.
At the same time the **monitorage** program reads the beam triggers form the thin monitor, the *spaghetti* and the scales to calculate the photon flux.

2.8 Simulation

The **laggen** program is based on the GEANT3.21 package [59]. It generates a given reaction channel, describes the structure of the detector LAGRANγE and simulates the response of the apparatus to photoreactions on protons. The events are producted by a γ randomly generated using the energy distribution obtained with the beam simulation (not reported in the figure). The reaction channels can be chosen on a data base composed of 23 (for the proton) possible hadronic (and non hadronic) reactions, which are reported in the appendix B. The program includes the known cross sections for each channel: most of them are known with a 10% precision and rare reactions are approximated with a cross section of about 1 $\mu barn$. Some cross sections are also theoretically extrapolated in some kinematic regions. The particle kinematics is then randomly generated on the basis of these cross sections. The GEANT pakage simulates the detector geometry and, step by step, the interaction of particles with the matter. The electromagnetic decay of mesons has been optimized [55, 60] with the FLUKA pakage, a Monte Carlo code, which simulates hadron and lepton cascades from several TeV down to a few keV (thermal energies for neutrons). Moreover, the program preserves the initial momentum, energy and vertex of each primary particle.
Lagdig simulates the response of the LAGRANγE detector. It reads event files generated by **laggen**, applies the response of each detector (attenuation, dispersion, threshold,...), supplied by the **data.base** file, and converts the informations into digital format. Hence, a subroutine can then be used to select different triggers corresponding to different event classes.

Chapter 3

The cylindrical chambers

Introduction

The analysis of reaction channels with three charged particles in the final state is one of the main goals of the GRAAL collaboration. In particular, as explained in the theoretical chapter, the channels like $K\Lambda$ and ωN allow to access to new polarisation observables.

In the chapter on the apparatus we stressed that the angular resolution of the plastic scintillators and of the electromagnetic calorimeter in the central part of the detector are not sufficient if we want to use longer targets for channels with low cross section (as the kaon photoproduction, whose cross section is about 1 μbarn). The angular resolution of the BGO gets much worse with long targets, therefore the kinematic cuts, which are used to separate a given channel, have a selectivity largely reduced. In order to improve the situation it is therefore necessary to use the cylindrical MWPC[1]s which give a much better angular resolution and a higher selectivity of the kinematic cuts.

From this point of view an accurate study of the performances and an optimization of the detection efficiency of the cylindrical chambers have been necessary and it constitutes the main part of this thesis. Later on, in the analysis chapter, we will test the performance of the track reconstruction on the $K\Lambda$, η and ω photoproduction.

In the first section we will describe the operating principle, the geometrical structure and the readout system of the cylindrical MWPCs. The algorithms for the track reconstruction are, then, reported in the second section. In the third section we will test the simulation software of the chambers and to check its reliability in order to establish their spatial resolution and reconstruction efficiency. The fourth section is devoted to the main

[1]MultiWire Proportional Chamber

applications of the cylindrical chambers: at first, we will treat the identification of the reaction vertex, which is useful to correct the angles of the photons detected by the BGO, as well as to calculate the mean free path of baryons which decay weakly (as the Λ); at second, we will show how the beam misalignment is determined and corrected from the measurement of the azimuthal resolution of the cylindrical chambers.

3.1 Detector description

3.1.1 Geometrical structure

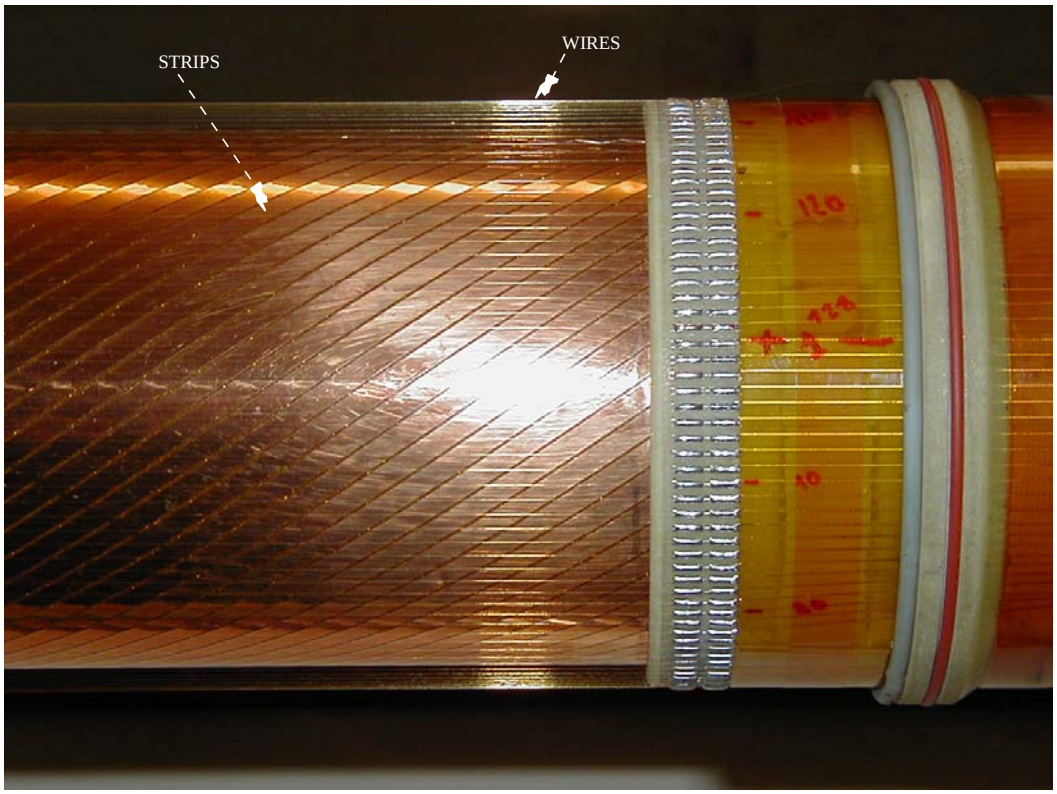

Figure 3.1: *Image of the cylindrical chamber: the wires and the internal cathode of the internal chamber are shown. The second cathode (not present) is superimposed with opposite helicity.*

Our detector is composed of two, concentric, cylindrical multiwire proportional chambers. For each chamber the anodes consist of gilt tungsten wires (20 μm diameter) stretched along the cylinder axis (corresponding to the beam one). The wires are surrounded by two cathodes made of strips with as shown in figure 3.1. The gap between wires and strips

is 4 mm.

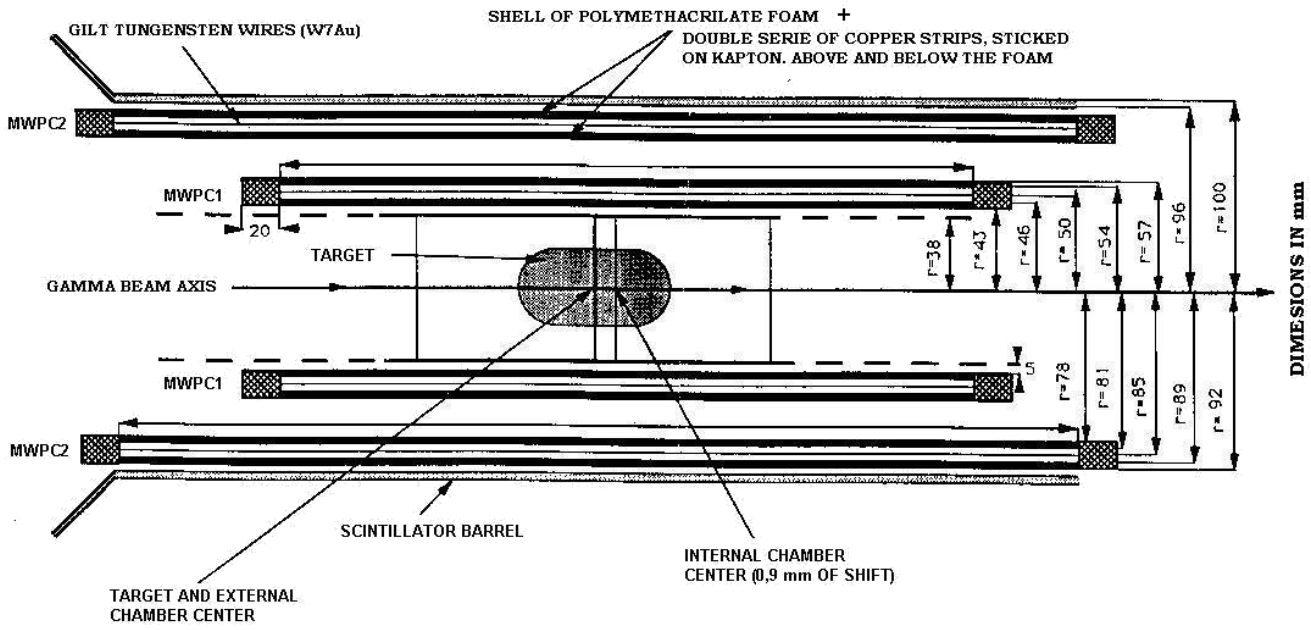

Figure 3.2: *Section of the cylindrical chambers along the beam axis.*

	Chamber 1		Chamber 2	
Length	400 mm		505 mm	
Diameter of the wire plane	100 mm		170 mm	
Number of wires	128		192	
Distance between wires	2.45 mm		2.78 mm	
	Int. Cath.	Ext. Cath.	Int. Cath.	Ext. Cath.
Cathode diameter	92 mm	108 mm	162 mm	178 mm
Number of strips	60	64	96	96
Polar orientation of the strips	33.86^o	-41.01^o	41.01^o	-46.63^o

Table 3.1: *Geometrical dimensions of the cylindrical chambers.*

The structure of each chamber is shown in figure 3.2 and their dimensions are reported in table 3.1. The cathodes are made of Copper deposited on Kapton sheets which are glued on a shell of polymethacrilate foam. The two cathodes of one chamber are structured in adjacent strips (3.5 mm wide, 0.5 mm between two strips) as spirals around the beam axis (figure 3.1) and with opposite helicity with respect to the beam (z) axis. The gas of the chamber is an Argon-Ethan (85 and 15 % respectively) mixture.

Operation principle

A high negative voltage is applied to the cathode strips and the electric field lines are similar to the case shown in figure 3.3.

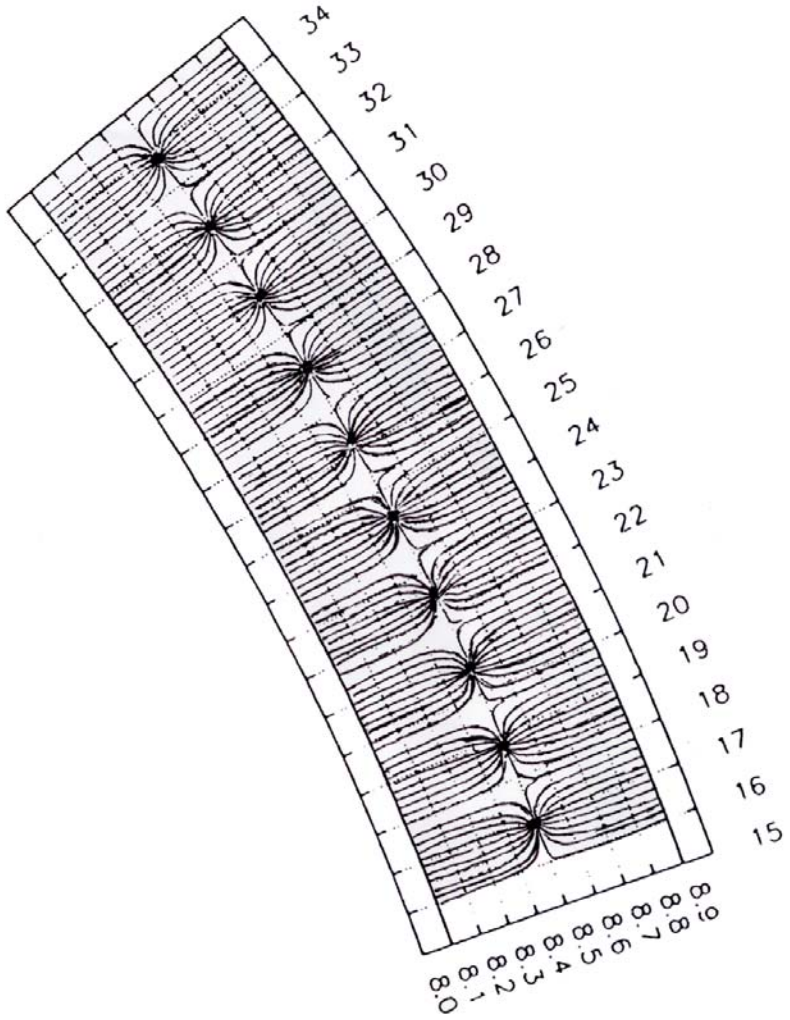

Figure 3.3: *Electric field lines in the cylindrical MWPC.*

Except for the region very close to the anode wires, the field lines are essentially parallel and almost constant. If a charged particle crosses the chamber, electrons and ions are created from the Argon molecules and they will drift along the field lines towards the nearest anode wire and opposite cathode respectively. Upon reaching the high field region (close to the wires) the electrons will produce an avalanche and generate a negative signal on the anode wires. The positive ions induce, by influence, a negative charge on the

anodes.
The azimuthal position of a given particle is directly deduced from the hit wire and the position along the chamber axis (z coordinate) is calculated from the charge distribution on the cathode strips (evaluation of the centroid [61, 62]).
The center of gravity of the charges is obtained from only three significant strips. A more complicated method involves a Gaussian curve fitting to the charges of three significant strips, but it will not be used in this work. So, if the charge distribution has a peak on the strip i with a charge S_i the centroid from the three significant strips is given by:

$$\delta_x = x_{centroid} - x_i = w\frac{-S_{i-1} + S_{i+1}}{S_{i-1} + S_i + S_{i+1}} \tag{3.1}$$

where $w = 4\ mm$ is the distance between the centers of two adjacent strips. The real distribution of influence charge is thus truncated. To take into account this effect we have to correct the value δ_x [56]:

$$\delta_x^c = 1.45 \quad \delta_x \tag{3.2}$$

Read-out system

Each wire is read by a single integrated circuit ASIC16, developed by the ISN[2][63] in order to satisfy the requirements of the GRAAL experiment. As we said in the previous chapter, the integrated circuit ASIC16 allows serial to parallel conversion, pattern recognition and validation of adjacent channels.
In figure 3.4 the readout system for a cylindrical chamber is shown. The signal of a wire (CIW) is processed by two ASIC types: the Wire Processor and the CPT32. In the first one the signal is amplified by a voltage amplifier, then a fast ECL comparator permits the amplitude discrimination (Discr) and a delay (Delay) between 30 and 500 ns can be programmed in order to assure the coincidence with the experiment trigger. During this delay a constant current is produced that provides a multiplicity signal by summing the currents of different channels in a resistor. Finally, a one bit memory can be set if a coincidence occurs. The second one (CPT32) contains 32 channels of 32 bit counters and controls the counting rate of each wire. The conversion time is typically $4\mu s$.
The read-out system for the cathode strips is also shown in 3.4 for the internal cathode (CIBI) and the lower part of the picture for the external cathode. The logic output signal

[2]Institut des Sciences Nucléaires (Grenoble, France)

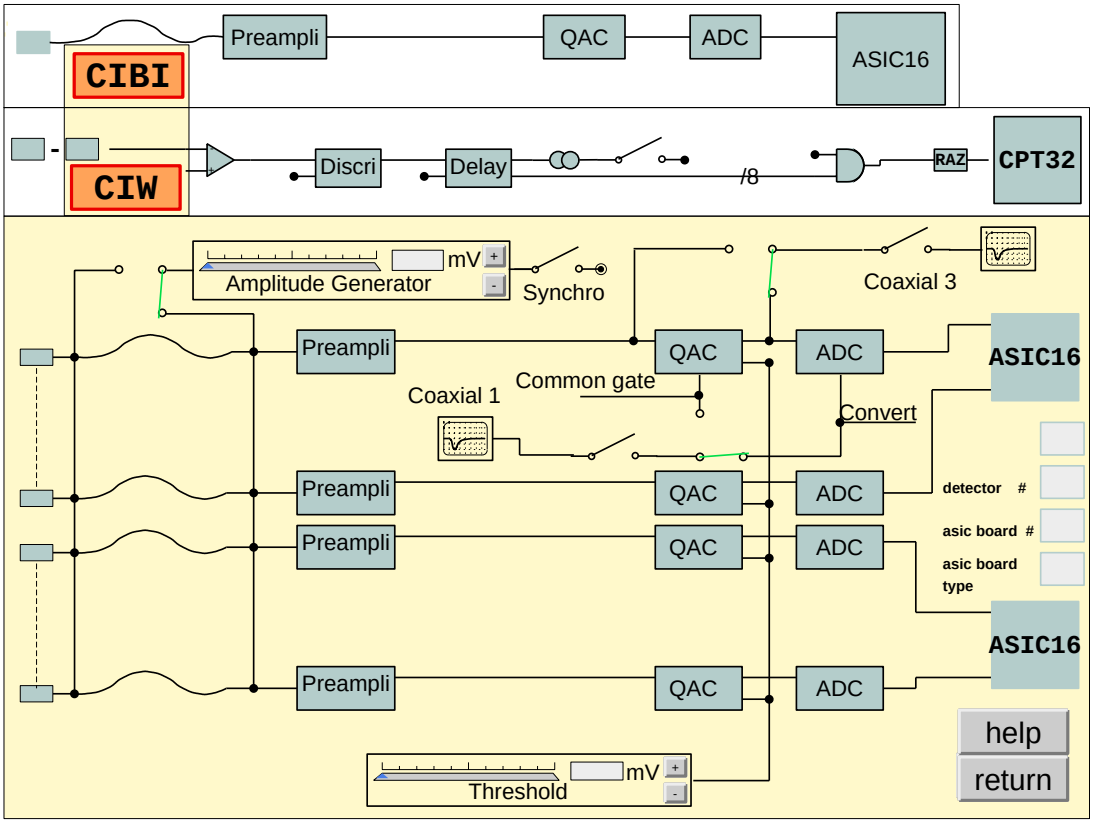

Figure 3.4: *Read-out system for wires and cathode strips of one chamber. CIBI is the compressed block diagram for the internal cathode, CIW is the block diagram for the wires and the lower part is the uncompressed block diagram for the external cathode.*

from the QAC (charge to amplitude converter) detects the strips carrying a charge greater than a fixed threshold, which is set above the pedestal level.

The "Bordurage" function

The pedestal of the signals read from the cathode strip have to be calculated and subtracted in order to have the right value of the charge. This value of the ADC channel is calculated when there is no voltage supply on the strips and it has the peculiarity to be very different from strip to strip due to the dispersion of each electronic component (amplifiers, resistors, etc). A fortran program fit all the pedestal peaks strip by strip in order to define the maxima of the distribution and their dispersion. An example of these value is given in figure 3.5 for the first cathode of the internal chamber (60 strips).
This calculation is performed at the beginning of each period of data taking (which is about one month long) but a check of the pedestal stability must be executed for each

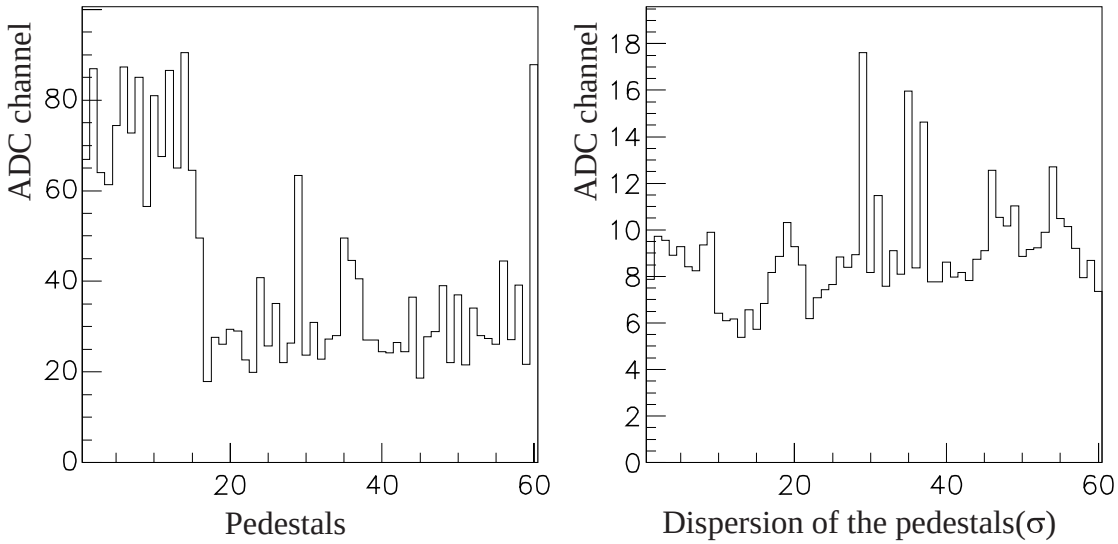

Figure 3.5: *Average value of the pedestals (on the left) and the dispersion (on the right) for the sixty strips of the fist cathode of the internal chamber.*

data run (which is 2-3 hours long). In the electronic set-up the same threshold is applied to all the strips. This solution, which has been chosen to simplify the electronics, may cause a loss of efficiency because of the pedestal is variation from strip to strip. In fact, if the pedestal is very high all the events in the ADC spectra will be over threshold; on the contrary if the pedestal is low most of the real distribution will be not detected.

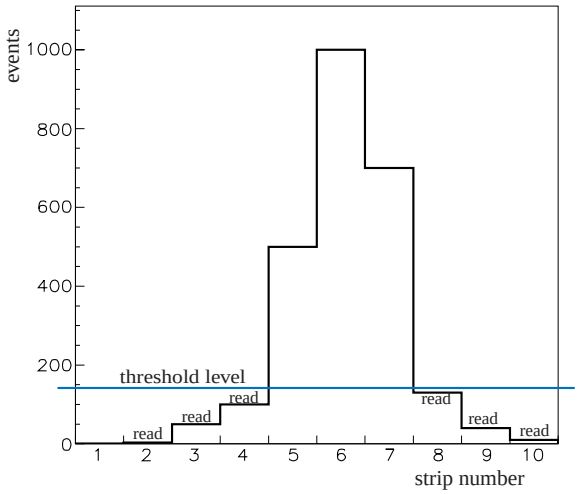

Figure 3.6: *Recovery of some strips which are under threshold. This way most of strips with a low pedestal will be read*

In order to recover all these signals a procedure, called *function bordurage*, is used: instead

of only considering strips above the fixed threshold on the charge, three strips under threshold are also read, as shown in figure 3.6. In this example the electronics will read, as well, the strips number 2, 3 and 4 as well as the strips 8, 9 and 10. This procedure will allow, this way, to recover strips with a too low pedestal. Another solution would be to read all the cathode strips at the same time, but this will cause a huge amount of data to be recorded.

3.2 Algorithms for the track reconstruction

When a charged particle hits one of the two chambers it will release a negative signal on a wire and a positive one on a cluster of strips on both cathodes. An example of the detector response for the simulation of a $p\eta(\pi^+\pi^-\pi^\circ)$ event is reported in figure 3.7.

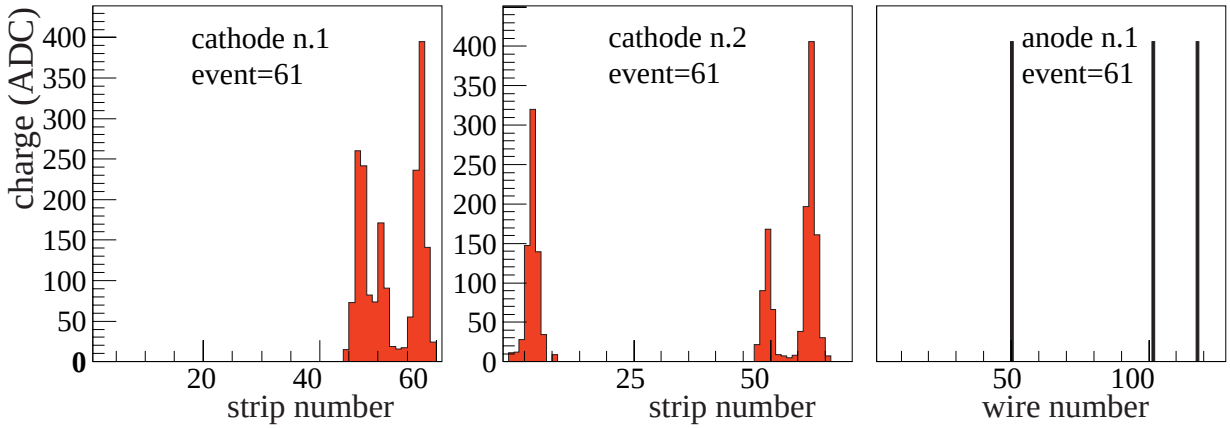

Figure 3.7: *Detection of a $p\eta(\pi^+\pi^-\pi^\circ)$ simulated event, where three charged particles are expected in the cylindrical MWPCs. Left and center: signals from the cathode strips (after pedestal subtraction). Right: signals from the anode wires.*

The programs which analyze and merge the response of each chamber and their association are presented in the diagram 3.8. The steps are:

1. cluster identification on each cathode and calculation of their center of gravity;
2. identification of the hit wires and calculation of the azimuthal coordinate of the tracks;
3. for each chamber, association of each wire with a cluster on the first cathode and a cluster on the second one; all the possible combinations are retained and then

we will choose the one that gives the lowest distance between the z coordinates reconstructed on the two cathodes;

4. at this step we have identified all the possible points in each chamber: each point corresponds to a wire (ϕ_1), a cluster (z_1) on the first cathode and a cluster (z_2) on the second one; we act to associate the points in the first and second chamber and to choose the solutions with the lower differences $\phi_1 - \phi_2$. The θ and ϕ for each track can then be calculated.

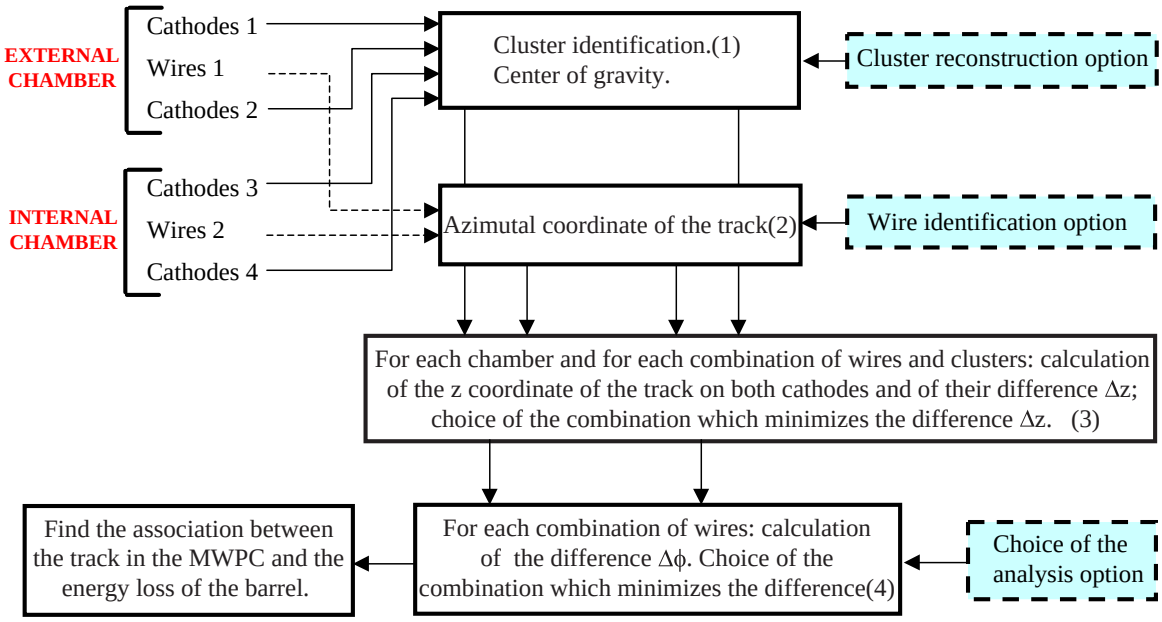

Figure 3.8: *All the programs for the track reconstruction. The name of the fortran programs are in italics.*

1. Cluster identification

A cluster consists in a sequence of adjacent strips which have a signal above the threshold. The program looks for relative maxima in each cluster. If it finds more than one maximum in the same cluster (that is the case of both cathodes in figure 3.7) it will separate the cluster in as many clusters as the number of relative maxima. Clusters with one or two strips are considered only if their total charge is greater than a fixed threshold.
For each cluster the centroid and the total charge are calculated by using equation (3.1). The coordinate x of the center of gravity of the cluster on the axis ν in figure 3.9 is given by:

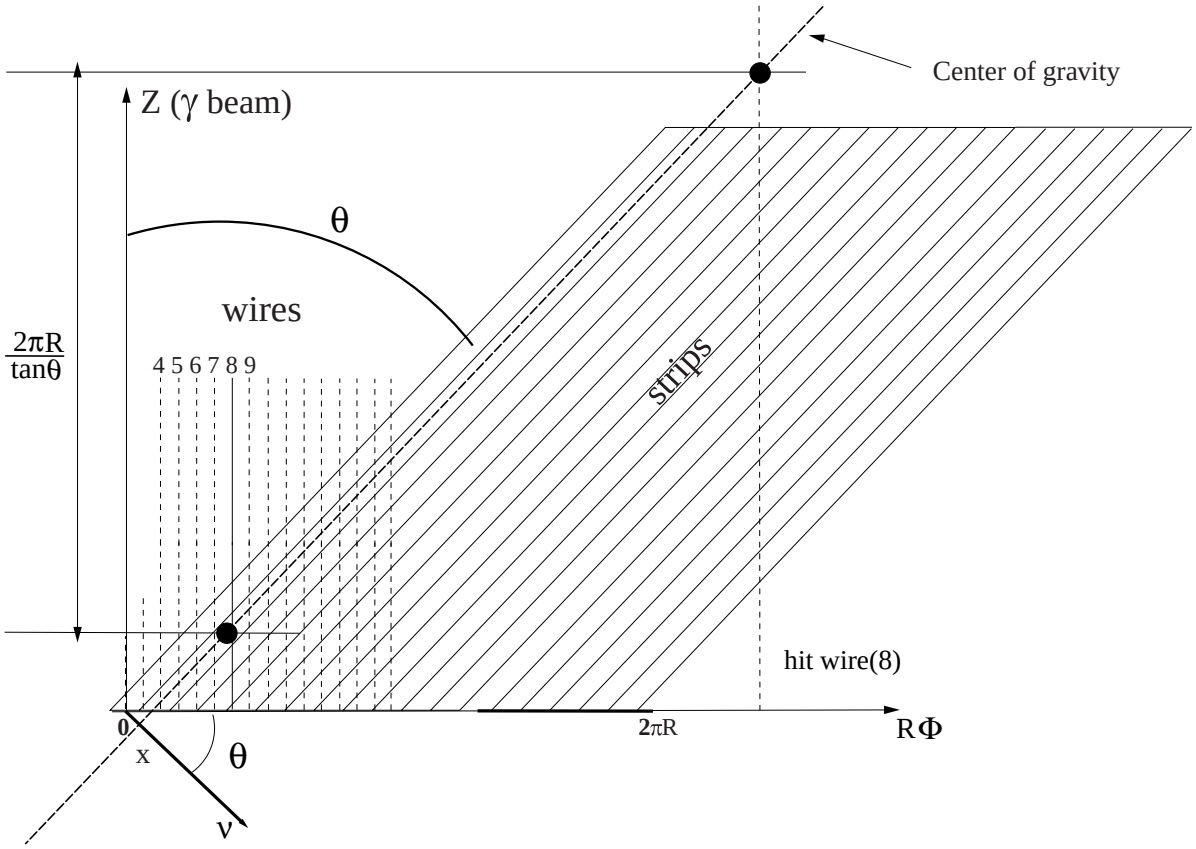

Figure 3.9: *Geometrical reconstruction of the z coordinate of one cluster. For simplicity the cluster is represented as point-like.*

$$x = \delta_x + (n_{peak} - 1) \cdot w \tag{3.3}$$

where n_{peak} is the strip number corresponding to the cluster maximum and w the distance between the centers of two adjacent strips. Cases with one or two strips per cluster are also considered. In the first case the center of gravity of the cluster corresponds to the single strip, while in the second one the center of gravity is the average on the number of strips weighed with their charges.

2. Wire identification

The hit wire directly gives the azimuthal coordinate of the track. If n is the total number of wires and i is the hit wire, ϕ is given by:

$$\phi = \frac{1}{2\pi}\frac{i-1}{n} \tag{3.4}$$

3. Wire-cathode association

Once ϕ is known, we calculate the intersection of each wire with each cluster on the cathode, by using the technique of figure 3.9. This intersection corresponds to the z coordinate of the cluster: if x is the center of gravity value on the axis ν perpendicular to the strips and $R\phi$ the coordinate of the wire on the axis perpendicular to the wires, the z coordinate of the cluster is given by the formula:

$$z = \frac{R\phi}{\tan\theta} - \frac{x}{\sin\theta} \tag{3.5}$$

where θ is the angle between strips and wires. If the intersection between the strip and the wire falls outside the domain of z corresponding to the chamber, the correction value will be:

$$\begin{aligned} z &= \frac{R\phi}{\tan\theta} - \frac{x}{\sin\theta} + \frac{2\pi R}{\tan\theta} \qquad if \qquad z < z^{min}_{cylinder} \\ z &= \frac{R\phi}{\tan\theta} - \frac{x}{\sin\theta} - \frac{2\pi R}{\tan\theta} \qquad if \qquad z > z^{max}_{cylinder} \end{aligned}$$

This way, for a given track and for each hit wire, we obtain a value z_1 for the first cathode and a value z_2 for the second one. The track coordinate, z, is the average between z_1 and z_2 and the charge associated to the chamber is the average of the cluster charges. When several tracks are present, all the possible values of z_1 and z_2 are calculated and only those which have the lowest values of $\mid z_1 - z_2 \mid$ are retained.

4. Chamber association

At this point we have n_i tracks, each one corresponding to a pair (ϕ_i, z_i), in the internal chamber and n_e, corresponding to (ϕ_e, z_e) pairs, in the external one.
A track in the first chamber is associated to another one in the second chamber if the difference[3] $\phi_i - \phi_e$ is close to 0. Once the best solution has been chosen, each track is identified by the pairs (ϕ_i, z_i) and (ϕ_e, z_e). The intersection of a given track with both chambers is then calculated in the cartesian coordinates.

3.3 Simulation of the chamber response

In the previous section we showed how the track identification is accomplished by the reconstruction software. The best way to test the efficiency of these algorithms has been

[3]The cut used in this work is $\phi_i - \phi_e \leq 8^\circ$

to use simulated events. The main problem is to define the efficiency of the single track reconstruction and, then, to extend this result to more complicated reactions that produce up to three charged particles in the cylindrical chambers.
In this context we chose to study the π° photoproduction which has only one charged particle in the final state and, then, to extend these results to the η decay in $\pi^+\pi^-\pi^\circ$. In the first case we have the advantage that this channel can be selected without the use of the cylindrical chambers. The result of our algorithms can so be tested on π° data in order to validate the simulation. The simulation of the second one is, hence, studied to extract the expected efficiencies for the two or three track reconstruction. The π° photoproduction is also a tool to estimate the angular resolution for the proton.
In addition to what is previously said, we will also show how some improvements of the algorithms have been necessary for the agreement between simulation and data: the most important of them are the separation of the overlapped clusters on the cathodes, the dependence of the z resolution on the shower mechanism in the gas chamber and the influence of the beam alignment on the azimuthal resolution. We will deal with them during this section, except for the beam alignment, which requires a separated section.
As first step we thus describe the simulation in order to highlight the parameters which play an important role in the spatial resolution as well as in the efficiency.
The flow chart of the simulation code is represented in figure 2.11 on page 36. For each primary and secondary particle of the event generator and for each chamber, the program records (see table C.1) the cartesian and cylindrical coordinates of the intersection between the track and the wire and the energy loss in the gas gap. The geometrical dimensions used in laggen are reported in figure 3.2. Each particle is followed from the moment it is produced in the target to the moment it reaches the anode, produces the electron avalanche and then most probably leaves the detector.
The program **lagdig** simulated the response of the chambers, i.e.:

- address of the hit wire;

- deposited charge on the strips of both cathodes.

The second item is, of course, the most difficult one because the avalanche process inside the chambers presents a large statistical dispersion, which must be reproduced as closely as possible. The energy loss of the particle inside the chamber, as given by laggen, is the starting point. The total energy deposited is converted into a total charge (by a conversion constant to be adjusted) and this value is randomized to reproduce the avalanche process.

The next step is, then, to determine the charge deposited on each strip. This is achieved by using the theoretical distribution [64]:

$$Q_i = \frac{-Q}{2\pi}\left[arctan\left(sinh\frac{\pi x}{2L}\right)\right]_{a_i}^{a_i+w} \tag{3.6}$$

where Q is the total charge, created inside the chamber, L the gap between the wire and the cathode, $w = 4\ mm$ the distance between the centers of two adjacent strips and a_i is the distance of the strip center from the cluster peak. The charge is hence shared out on nine adjacent strips. An **electronic noise** is randomly applied to each strip for all the cathodes. Later on, only strips with a charge greater than a fixed **threshold** are considered.

The informations are, hence, rewritten in digitized format for each chamber: the list of the active wires, together with their number, the list of active strips with their number and the collected charge per strip. All the **lagdig** parameters and variables are reported in table C.2.

3.3.1 Comparison between simulation and data

At this point we test if the simulation reproduces the data behaviour. To test the experimental response of the chambers, we use, as previously said, the π° events, selected by the BGO when the proton is emitted at central angles. The background in the selected events is lower than 1% [51], which is the most favorable condition to test the track reconstruction.

In figure 3.10 the charge per cluster on a cathode is reported. Data are represented by the full line, while simulation is represented by the dashed line. In both data and simulation we have already eliminated clusters with low multiplicity (that is to say clusters with only four strips), which produce a great peak at low channels. The selections applied on simulation and data consists in the cut on $\Delta z = |z_1 - z_2|$, as shown in figure 3.11, where z_1 and z_2 are the center of gravity coordinates for a cluster on the first and second cathode respectively. They are determined, as explained in the algorithm section by the intersection with the hit wire. The values used for simulation and data are $\Delta z = |z_1 - z_2| \leq 0.06\ cm$ and $\Delta z = |z_1 - z_2| \leq 0.3\ cm$ respectively (this difference will be explained below). The second selection on the simulation and data is $\Delta\phi = |\phi_i - \phi_e| \leq 8^\circ$ between the azimuthal angles of tracks in the internal and external chamber, as shown in figure 3.12. As we see the agreement between simulation and data is almost perfect, thus confirming the proper choice of the simulation parameters.

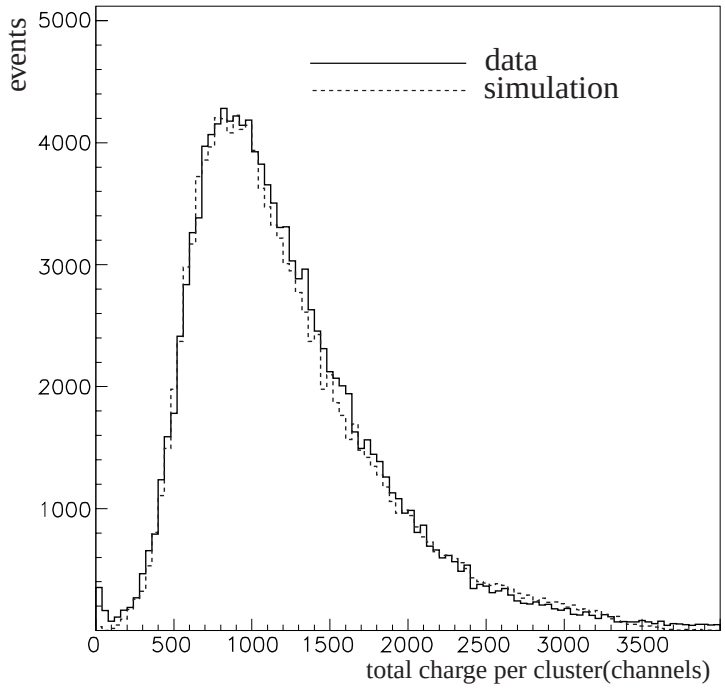

Figure 3.10: *The cluster charge of protons on a cathode for real (full line) and simulated (dashed line) data.*

Let us check now the quantities Δz and $\Delta\phi$, which are the cuts applied by our algorithms and which give an estimation of the z and ϕ resolution of the chamber.
The ϕ dispersion seems enough realistic. In fact, if we consider that for each chamber the resolution is the number of wires divided by 360°, by a simple calculation we obtain:

$$\sigma_\phi = \sqrt{\left(\frac{360/128}{2.35}\right)^2 + \left(\frac{360/196}{2.35}\right)^2} = 1.4^\circ$$

The simulation gives $\sigma_\phi^s = 1.971^\circ$ and the data $\sigma_\phi^d = 1.968^\circ$. The difference between the expected value 1.4° and the simulated and real ones is due to the particle straggling, which is included in the simulation. The cut applied on $\Delta\phi$ is thus suitable.
As we can see, the z resolution is much lower in simulation ($\sigma_z^s = 0.030\ cm$) than in data ($\sigma_z^d = 0.055\ cm$). It means that we underestimate some effects in the simulation. The effect coming from the particle straggling through different materials is already included in the simulation, so we must look for other neglected effects. One of them may be the approximation in the **electron avalanche mechanism**. The simulation program, actually, considers only the energy loss of the particle in the whole gas gap. In a more realistic picture the gas gap should be divided in a number of smaller gaps, that will

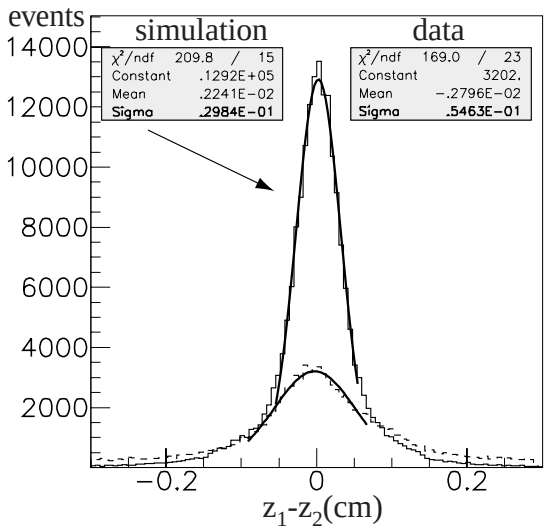

Figure 3.11: *Δz between the cathodes of one chamber for simulation (filled line) and data. Data have a much lower resolution.*

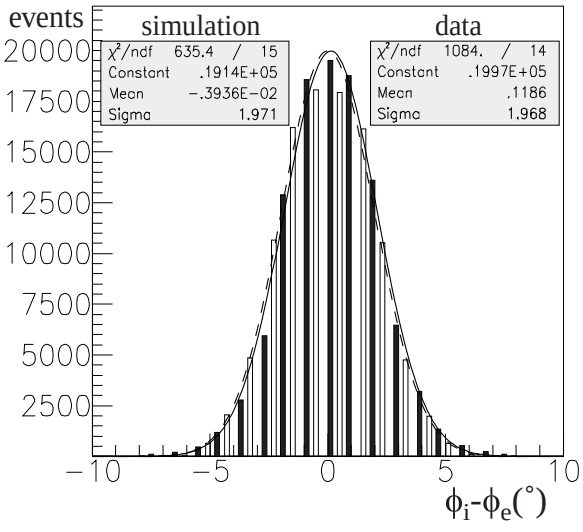

Figure 3.12: *$\Delta\phi$ between the two chamber for simulation (coloured line) and data. The azimuthal angle is directly determined by the wire and it is, thus, discrete.*

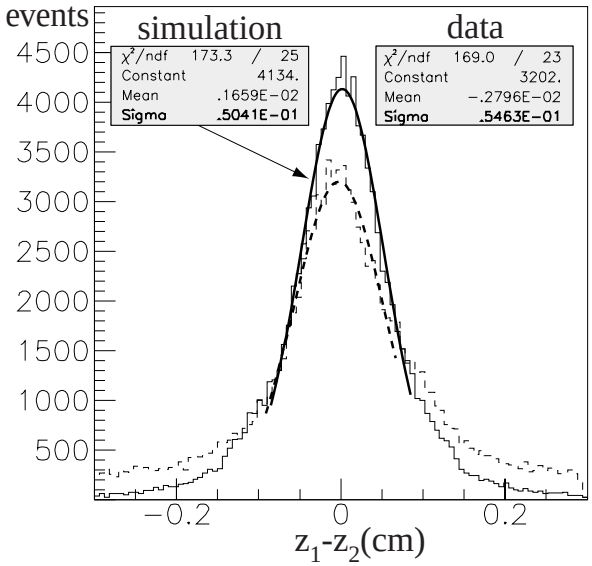

Figure 3.13: *Comparison of the new simulation with the data. The full line is the Δz of the new simulation while the dashed line are the data.*

independently produce an avalanche with their own statistical dispersions. The expected effect would be to enlarge the z dispersion and, as a consequence, the z resolution itself. At present, this modification has already been tested and it seems to give goods results,

the z resolution being now similar to the real one.
The preliminary result is shown in figure 3.13, where we compare again data and simulation. The effect produced by this new improvement of the simulation seems to approach the reality.

3.3.2 Spatial resolution

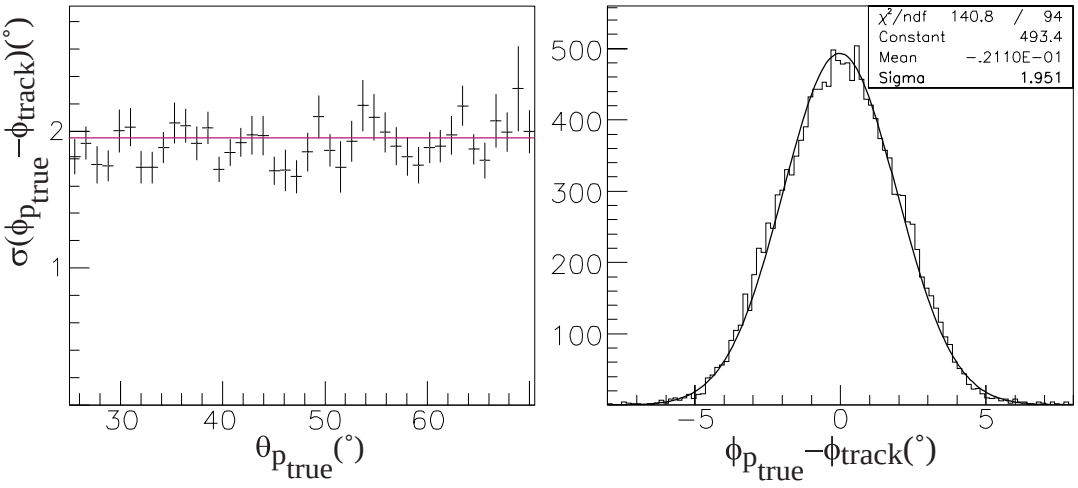

Figure 3.14: *Azimuthal resolution for the proton, extracted from the simulation. On the left the dispersion is plotted as a function of the true polar angle of the proton.*

In figure 3.14 and 3.15 we report for the simulation the difference between the true proton angle and the angle of the track. For both figures we show as well the dispersion σ as a function of the polar angle itself. In the ϕ case we observe the same resolution measured for $\phi_i - \phi_e$. That is evident because the ϕ coordinate is directly given by the hit wire (as explained in the algorithm section). Its evolution as function of $\theta_{p_{true}}$ is constant as expected.
The θ resolution depends on the z resolution itself and, thus, we infer it is underestimated. The θ dispersion ranges form 0.2 up to 1°. The rise at higher polar angles is due to the lower charge induced by the electron avalanche when the particle crosses smaller gas thickness (we thus expect the worst resolution at $\theta_{p_{true}} = 90°$). In this case, too, the new preliminary simulation seems to produce a more realistic resolution at about $\sigma_\theta \approx 2°$.
As we cannot properly estimate the θ resolution we can try to give anyway its limit. Let us compare, on data, the polar angle of the track, θ_{track} with the proton angle θ_p, calculated from the kinematics of the π° photoproduction: the two photons from the pion

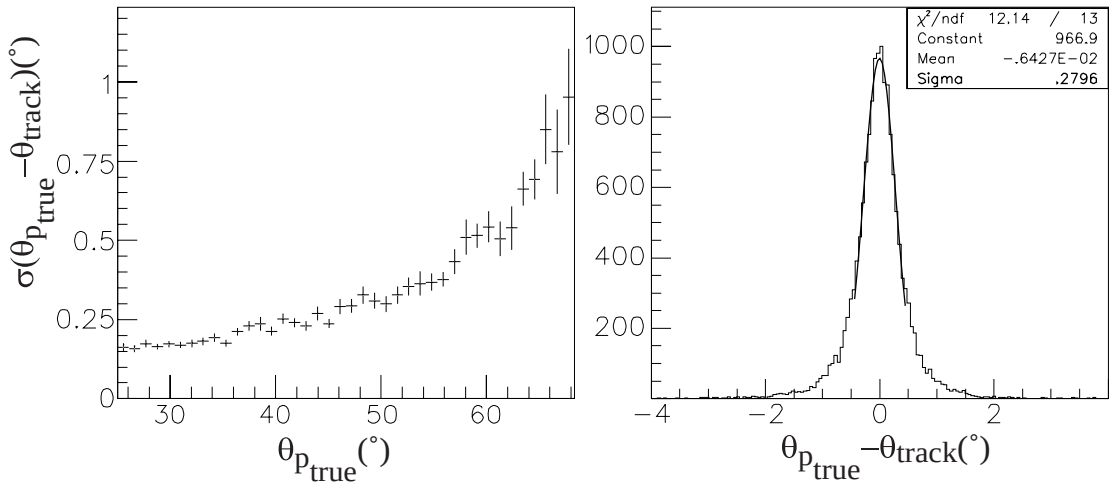

Figure 3.15: *Polar resolution for the proton, extracted from the simulation. On the left the dispersion is plotted as a function of the true polar angle of the proton.*

decay are detected in the BGO calorimeter, which gives information about their energy and angles. These values allow to calculate the pion invariant mass, together with its angular coordinates, energy and momentum. We can, thus, estimate the polar angle of the proton as a function of the meson momentum, its polar angle and the energy of the incident photon:

$$\cos\theta_p = \frac{E_\gamma - P_{\pi^\circ}\cos\theta_{\pi^\circ}}{\sqrt{{P_{\pi^\circ}}^2 + {E_\gamma}^2 - 2E_\gamma P_{\pi^\circ}\cos\theta_{\pi^\circ}}} \tag{3.7}$$

$\Delta\theta$ is shown in figure 3.16 and its dispersion is $\sigma(\Delta\theta) \approx 1.93°$. This value is an upper limit of the experimental θ resolution. In fact, $\sigma(\Delta\theta)$ is an optimized[4] convolution of the BGO angular and energy resolution for the two photons and of the energy resolution of the incident photon. $\sigma(\Delta\theta)$ is thus a convolution of the $\sigma(\theta_p)$ and $\sigma(\theta_{track})$ and we can consider it as an upper limit of the resolution.

The most proper way to measure the angular resolution would have been to measure the real resolution by using a source of charged particles in coincidence with a plastic scintillator. Notwithstanding, the installation of the cylindrical chamber in the GRAAL apparatus was requested very quickly and this test could not be accomplished.

[4]The π° angles are optimized (see in [51]) by an iteration on the kinematic solutions in order to reproduce the expected evolution of the momentum as a function of θ.

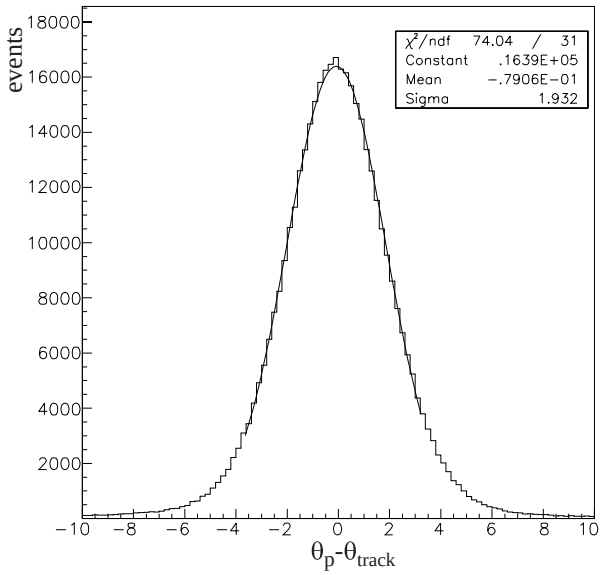

Figure 3.16: *The difference $\Delta\theta = \theta_p - \theta_{track}$ for protons. This is the convolution of the BGO and MWPC angular resolution.*

3.3.3 The chamber efficiency

Once the selections on the track reconstruction have been checked and the spatial resolution estimated, the following step is to estimate the efficiency of the track detection. We will calculate at first the efficiency for a single charged particle in the cylindrical MWPCs, as it is a direct consequence of the analysis reported in the previous paragraph. We will then estimate the efficiency for two and three charged particles by using the simulation of the η photoproduction in the decay channel $\pi^+\pi^-\pi^\circ$.

One charged particle efficiency

We will use again selected data from the π° photoproduction, which we used in the previous paragraph to estimate the spatial resolution. We select the π° events, where the proton has been identified in the cylindrical MWPCs and we calculate the number of tracks for which:

$$|\theta_p - \theta_{TRACK}| < 10^\circ \qquad\qquad |\phi_p - \phi_{TRACK}| < 10^\circ \tag{3.8}$$

The **proton efficiency** on the data is $\simeq 90$ %. The same calculation effectuated on the same simulated data with the same cuts gives $\simeq 95$ %.
The **pion efficiency** has been estimated [65] in the π^+ photoproduction. The neutron is detected with either the Shower Wall in the forward direction or the BGO calorimeter in

the central direction, while the charged particle is the result of the detection of a charged cluster in the BGO. The identification is accomplished by the correlations between the tagger energy and theta angles of both particles. The global efficiency is $\approx 90\%$.

Two and three charged particle efficiency (simulation)

The reconstruction of events with two and three charged particles in the final state is complicated by the fact that some clusters on the chamber cathodes can overlap. An example of overlapping has been given in figure 3.7. This effect (due to the kinematics of the reaction $\eta \to \pi^+\pi^-\pi^\circ$) occurs in about one half of the events for which three charged particles cross the cylindrical MWPCs. In fact, the track is lost when one cathode alone has an overlap and if a recovery algorithm is not applied.
Hence it has been necessary to recover these mixed cluster, as explained in the algorithm section: for each cluster the program looks for all the relative maxima and separates the cluster in as many clusters as the number of detected maxima. The improvement is shown in figure 3.17, where on the left we report the number of clusters after the association with the hit wire and on the right the cluster multiplicity. We uses the simulation of the η photoproduction, with its decay in $\pi^+\pi^-\pi^\circ$, which we will study in the analysis chapter.

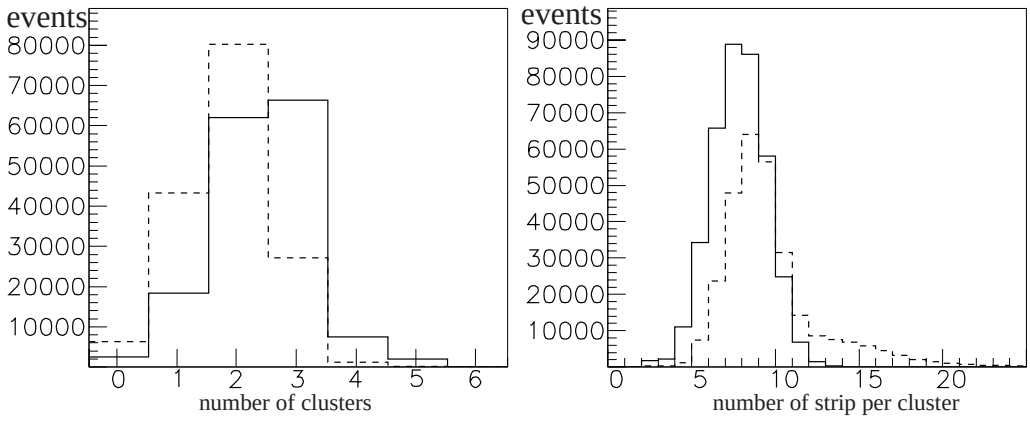

Figure 3.17: *On the left the number of clusters of the first cathode. On the right the number of strip per cluster on the same cathode. For each histogram the dashed line is the version of the program which does not separate mixed clusters, the full line is the version with the recovery of mixed clusters.*

The improvement is very satisfactory as we manage to double the number of association in each chamber. The multiplicity is also more reliable because all the clusters have the same average multiplicity, which is equal to seven, while in the previous version of the

program there were a lot of clusters with high number of strips (that means an overlap occurred).

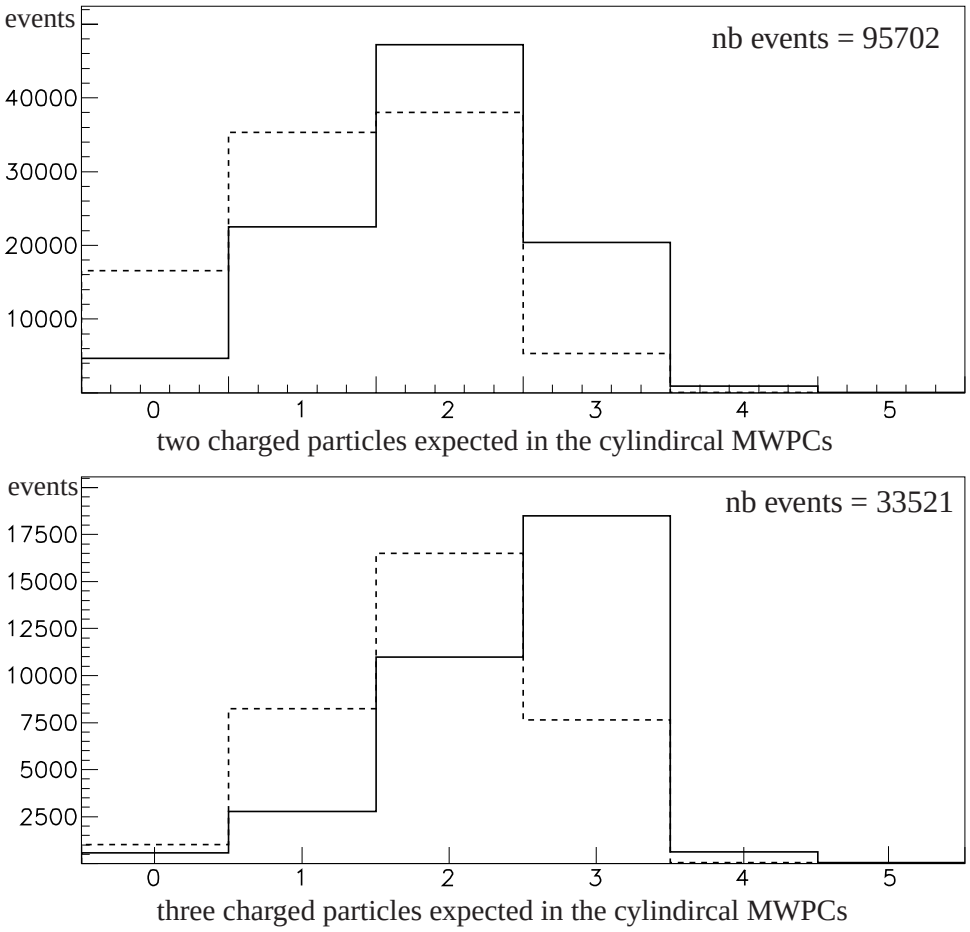

Figure 3.18: *Reconstruction efficiency of the cylindrical MWPC.*

We can now assess the value of the reconstruction efficiency for events with two or three charged particles in the final state. We use again the simulated events of the η photoproduction. In figure 3.18 we show the number of tracks detected in the cylindrical chambers, when two (above) or three (below) charged particles are respectively expected in the detector. We compare again the algorithm with (full line) and without (dashed line) the separation of the mixed clusters. In the two particle case the program identify respectively 71.6 % and 45.5% of the expected particles. In the three particle events we obtain respectively 57.2 % and 23.0%. The improvement is, therefore, significant.

3.4 Main benefits of the cylindrical MWPCs

3.4.1 The vertex reconstruction

One important feature of the cylindrical MWPCs is the reconstruction of the reaction and decay vertex. The vertex can, in fact, be extracted by calculating the intersection of two or more charged particles detected by the cylindrical and plane chambers. To show this feature we will use the simulation of the η photoproduction that decays in $\pi^+\pi^-\pi^o$ on a target 6 cm long:

$$\gamma + p \rightarrow \eta + p \rightarrow \pi^+ + \pi^- + \pi^\circ + p \tag{3.9}$$

Hence, we have the π^+ and π^- belonging to the decay vertex and the proton to the reaction vertex. The η decay is strong so that, in this case, the two vertices coincide. About half events of this channel have all the charged particles at $\theta \geq 25°$. This way, we will have a high statistic in order to perform the vertex reconstruction with three tracks.

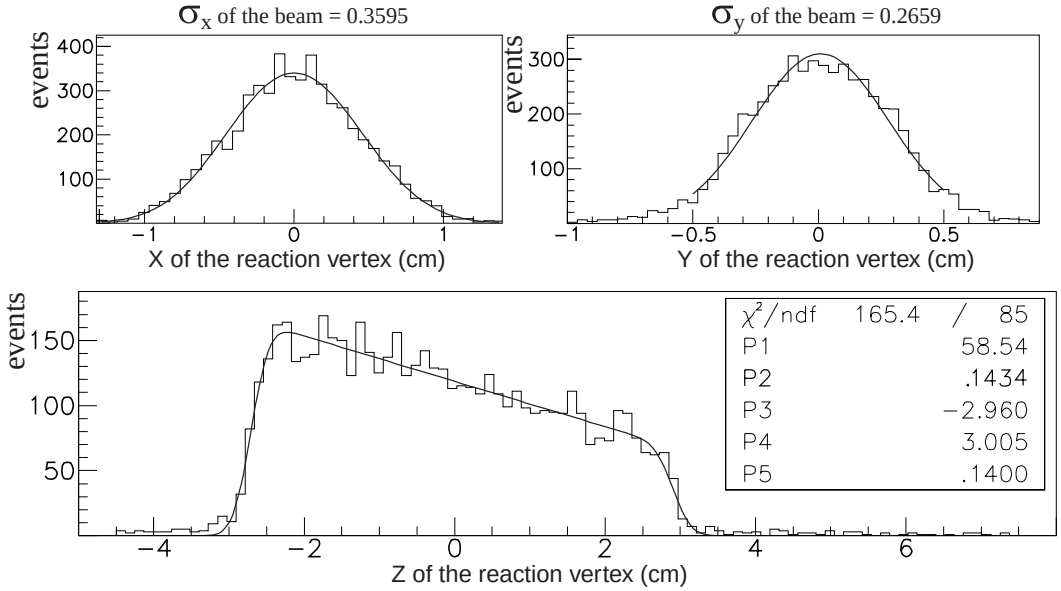

Figure 3.19: *Simulated reaction vertex for the channel (3.9), with the three charged particles in the cylindrical chambers. The fit of x and y coordinates is a Gaussian that gives the value of the beam dispersions. The fit on the z coordinate is from equation (3.10) and, in particular, P2 gives the Gaussian dispersion of the cartesian coordinate z.*

The reaction vertex is the intersection of the tracks corresponding to the three charged particles (π^+, π^-, p). The mathematical expressions for the vertex calculation are resolved

in appendix D.1 and in figure 3.19 the three cartesian coordinates of the reaction vertex (η,p) are shown. The X and Y distributions reflect the beam dispersion, while the Z one is projection of the target length. The increasing slope as a function of z is due to the particular kinematics, selected for the vertex reconstruction (all the three charged particles in the central detector). The fit used for the Z coordinate is the product of the error function erf, that describe the two target ends, and a decreasing line (only for the z coordinate), to take into account the slope along the z axis:

$$f(Z) = P1\Big[erf\Big(\frac{Z-P3}{P2\sqrt{2}}\Big) - erf\Big(\frac{Z-P4}{P2\sqrt{2}}\Big)\Big](1 - P5 \cdot Z) \tag{3.10}$$

where:

$$erf(X) = \frac{2}{\sqrt{\pi}} \int_0^X e^{-t^2} dt \tag{3.11}$$

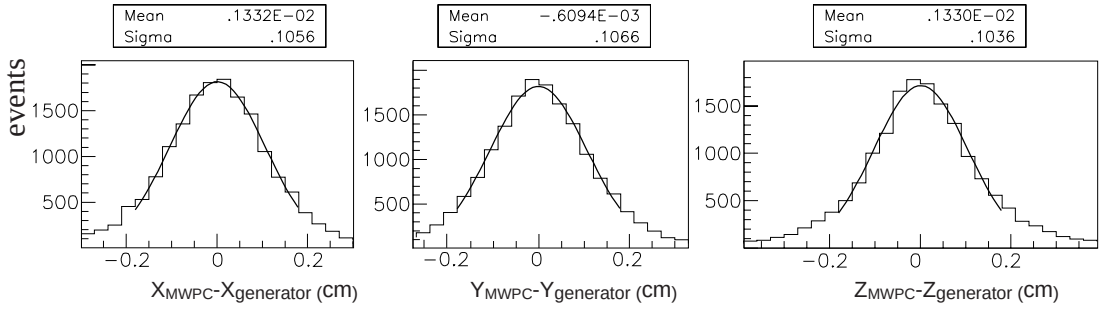

Figure 3.20: *Difference between the true reaction vertex and the one calculated by the intersection of the charged particle tracks. The reaction is always the (3.9) and the three charged particles have been detected in the cylindrical chambers. The fit is a Gaussian function.*

This way, $P3$ and $P4$ are the coordinates of the extremities (which correspond perfectly with the simulated values) of the target, while $P2$ is the relative dispersion. In order to check this calculation we compare the vertex coordinates of this method and the real vertex coordinates, as defined by the simulation. This difference is shown in figure 3.20. We have finally applied the method to the real data in figure 3.21 for the channel:

$$\gamma + p \rightarrow \pi^+ + \pi^- + p \tag{3.12}$$

The reason is that the selection of the η decay on data requires (as we will explain in chapter 4) a good identification of the π° in order to eliminate the background, which can influence the spatial resolution. The channel (3.12) is easier to be selected and, thus, the

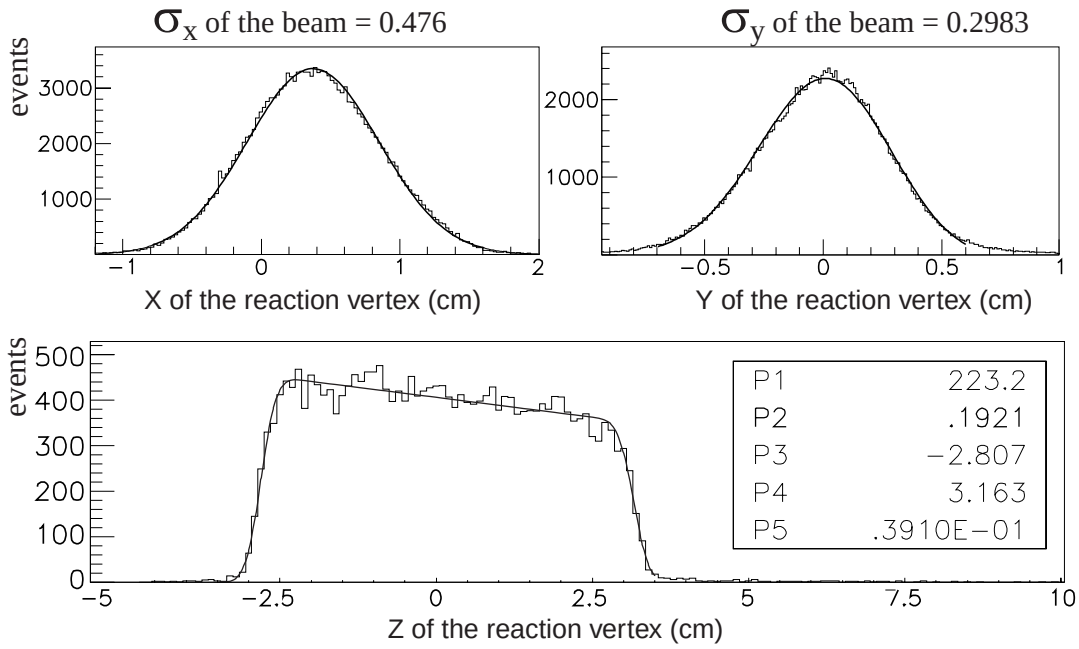

Figure 3.21: *Vertex coordinates on real data for the channel (3.12), with the three charged particles detected by the cylindrical MWPCs.*

resolutions of the cartesian coordinates will be more reliable. At a glance the target center is shifted in the x direction. This result shows that the beam is not perfectly centered in the BGO and cylindrical chambers. The comparison of different set of data shows that the beam position changes with time, due to small changes of the electron beam angles inside the intersection straight line of the experiment (between the two dipoles). This effect will be studied at the end of this section.

The dispersion in the x direction is greater than the simulated one in figure (3.19), due to a similar effect, while in the y direction we obtain comparable values. The z coordinate of the vertex is similar to the simulated one and we can estimate the target length as $P4 - P3 = 5.97\ cm$, which is in agreement with the true value ($6\ cm$). We can also observe that the z origin of the vertex is shifted in the forward direction of about $1.8\ mm$. This effect has been noticed and confirmed from the experimental set-up.

The z resolution from data is larger than the simulated one ($0.1921\ cm$ instead of $0.1434\ cm$). This effect is the same as the one we observed in figure 3.11 and it is due to the simulation of the cylindrical chambers itself. The charges, generated by a particle going through the chamber gas, are randomly created along the track inside the chamber, an effect which was not taken into account in the simulation. The recent preliminary version of the simu-

lation incorporates it and the agreement with respect to the data is improved, as we have already shown for the Δz cut in the previous section.

3.4.2 Effect of the vertex correction on the invariant masses

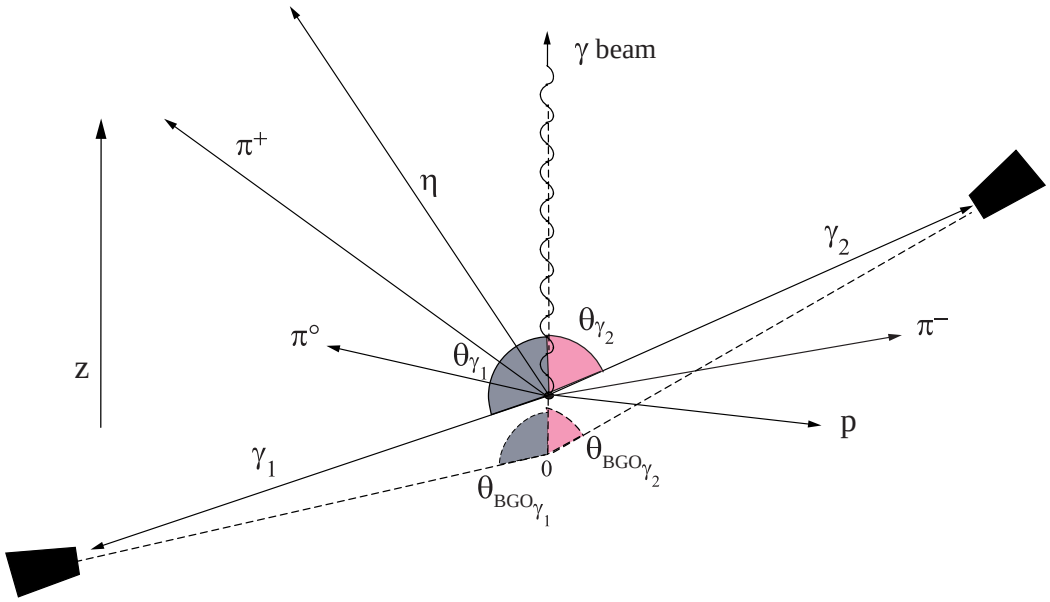

Figure 3.22: *An example of the kinematics of the η decay. θ_{γ_1} and θ_{γ_2} are the real angles of the photons which are different from the angles obtained by the BGO, $\theta_{BGO_{\gamma_1}}$ and $\theta_{BGO_{\gamma_2}}$, since we have to assume that the gammas are emitted from the center of the target. For simplicity we assume, in the picture, that the reaction and decay plane are equal.*

Let us consider again the η photoproduction and its decay into π^+, π^-, π°. If the location of the event inside the target is known (with a precision lower than the target length) we can improve the angular resolution of the BGO calorimeter for the photons produced in the π° decay and, as we will see, significantly improve the π° invariant mass. At the same time, if we correct the photon trajectories with the vertex information, the η invariant mass will also have a better resolution.

Once the reaction vertex has been calculated with the methods explained in the consecrated section we can correct the angles measured by the BGO. The photon angles is in fact determined by the BGO by taking as origin the target center (see $\theta_{BGO_{\gamma_1}}$ and $\theta_{BGO_{\gamma_2}}$ in the drawing). We have hence to reconstruct the real trajectories of the photons (θ_{γ_1} and θ_{γ_2}), which have as true origin the reaction vertex. In order to accomplish this correction we have to know the distance between the origin and the point at which the photon

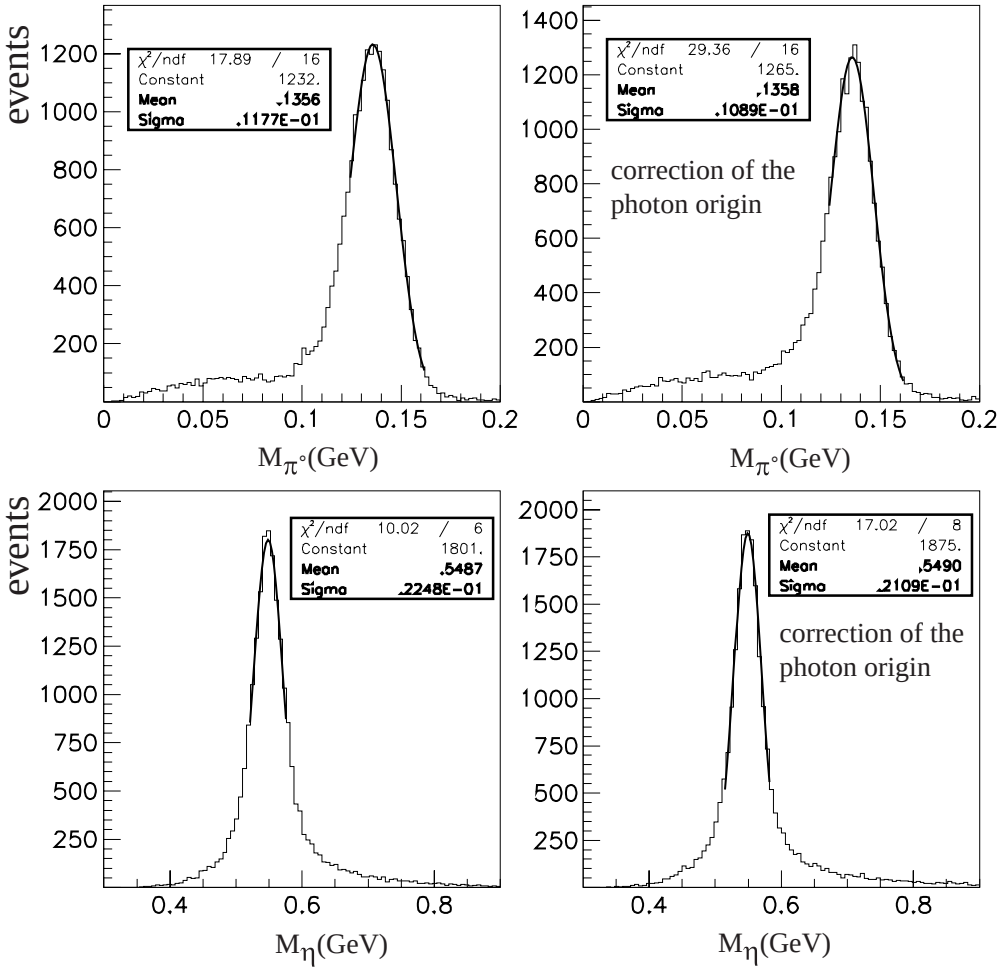

Figure 3.23: *Improvement in the invariant masses of π° (above) and η (below) with the vertex correction.*

shower is produced in the BGO. This value has been calculated with the simulation for different type of particles and we have estimated that the photon shower is statistically centered at $R = 16.9\ cm$ from the origin.

The invariant masses, calculated with and without this correction, for the π° and η are shown in figure 3.23. The invariant mass distribution for the π° shows some background but the width is significantly improved by a factor 8.1%. When a greater target will be used (12 cm) this correction will be absolutely necessary.

The invariant mass of the η shows a more limited improvement (6.2%) because the π° experimental information is combined with π^+ and π^- to calculate the invariant mass, reducing, this way, the global improvement.

3.4.3 Mean life of the Λ hyperon

As it is contains strange quarks, the baryon Λ has the feature to decay by weak interaction, with a life time of $2.632 \cdot 10^{-10} s$ and mean free path of 7.89 cm [6].
Since the cylindrical chambers can measure the reaction and decay vertices for a given channel with high precision if the final state has at least two charged particles, we can measure the Λ mean free path by studying its decay:

$$\gamma + p \rightarrow \Lambda + K^+ \rightarrow \pi^- + p + K^+$$

The kinematic is shown in figure 3.24. Once the tracks of the three charged particles has been detected, we can reconstruct the decay vertex from the π^- and the proton with the method described in the appendix D.1.

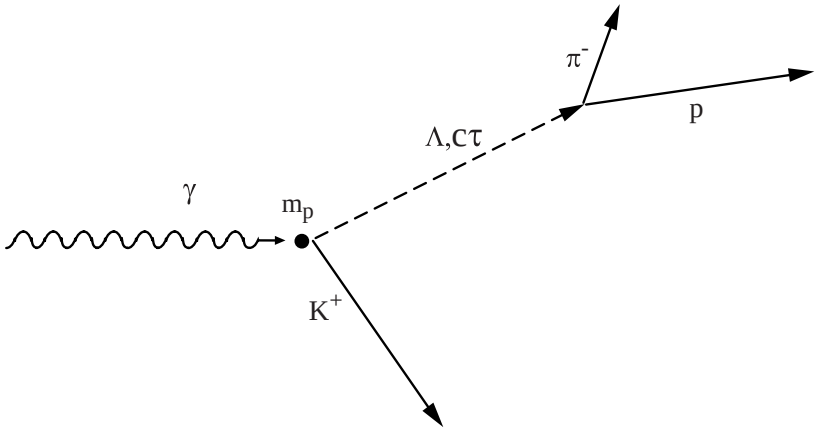

Figure 3.24: *An example of the $\gamma + p \rightarrow \Lambda + K^+$ kinematics.*

The measured angles and calculated momenta of the π^- and p give the spherical coordinates of the Λ. We can, then, use them to calculate the intersection with the kaon and, hence, the reaction vertex. The distance between the reaction vertex and the decay vertex gives the mean free path of the hyperon Λ, from which we can determine its life time τ. Such a life time is calculated in the reference system of the hyperon. The measurement is shown in figure 3.25.
We remember that the radius of the internal cylindrical MWPC is 5 cm long. It means that we cannot efficiently detect the pion and proton angles when the hyperon decays at a distance greater than 5 cm from the target. This effect produces a non linear behaviour of the free mean path in figure 3.25. We thus use only the first points to execute the linear and we obtain a mean life for the hyperon $c\tau_\Lambda = 7.584$ cm, which is close to the value reported in the literature.

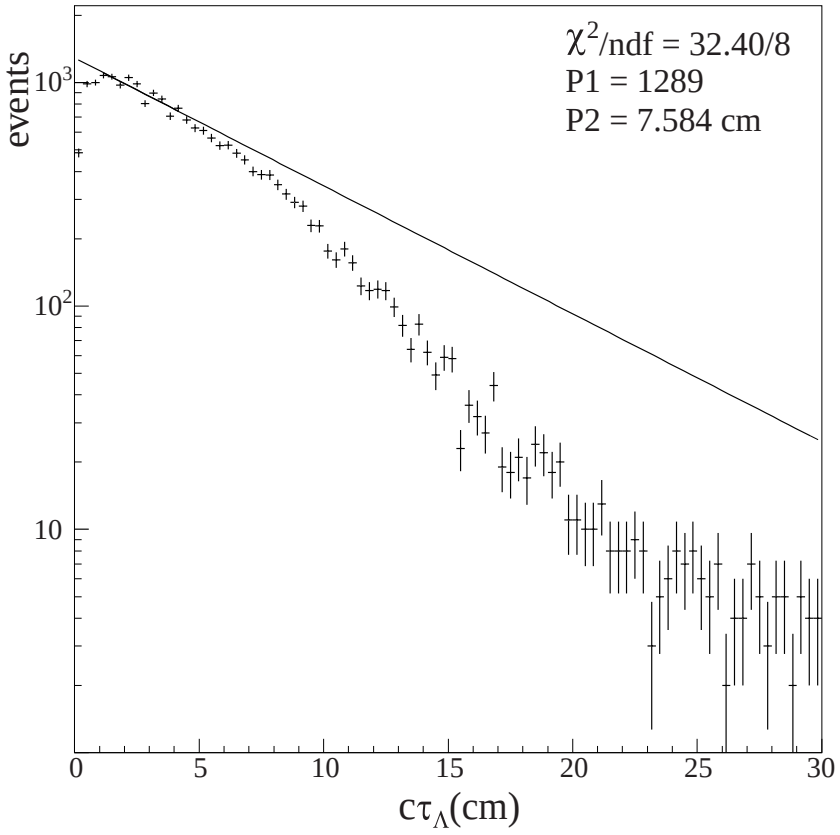

Figure 3.25: Λ *life time in the reference system of the hyperon.*

3.4.4 Monitoring of the beam alignment

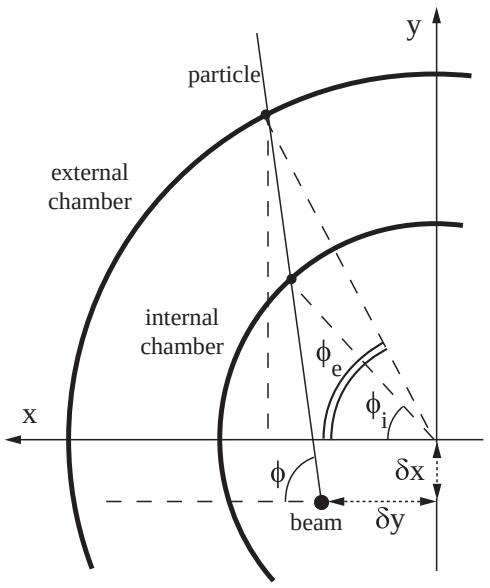

Figure 3.26: *Association between the two chambers.*

While in the simulation the beam is supposed centered at $x = y = 0$, in the data the beam misalignment with respect to the detector origin produces an additional dispersion in the azimuthal coordinates of the tracks, as we can see in figure 3.26. This broadening varies as a function of ϕ coordinate itself. In this section we will show that this effect can be corrected with the use of the cylindrical chambers.

If we see figure 3.26 we can notice that the difference $\Delta\phi$, studied in the previous sections, will be significant as soon as the beam is not centered. As a consequence the ϕ resolution will be in general greater than the simulated one. As example we show, in figure 3.27 on the left, $\Delta\phi = \phi_i - \phi_e$ for a particular period of data taking, when the beam was misaligned of few millimeters. The dispersion is $\sigma(\Delta\phi) = 2.56°$, which is greater than the simulated one previously calculated (1.93°). The evolution of $\Delta\phi$ as a function of ϕ_i (figure 3.27 on the centre) shows an oscillation which can be easily described by the following function:

$$\Delta\phi = \phi_e - \phi_i = \frac{R_e - R_i}{R_e R_i} \left(-\delta_x \sin\phi_i + \delta_y \cos\phi_i\right) \tag{3.13}$$

where R_i and R_e are respectively the internal and external radius of the chambers and δ_x and δ_y is the beam misalignment with respect to the origin (see figure 3.26). The demonstration of this equation is reported in the annex D.2. Hence the fit of the distribution gives the values of the beam misalignment, δ_x and δ_y. We can now correct ϕ_i and ϕ_e with respect to the new origin and calculate again the dispersion. The result is shown in figure (3.28) and, now, $\sigma(\Delta\phi) = 1.95°$, that is very close to the simulated one, thus confirming that the simulation properly reproduces the data. In the same way the azimuthal oscillation has disappeared.

This correction procedure is currently used for each period of data taking to take into account the small differences in the beam alignment. The data shown in figure 3.12 refer to a period in which the misalignment was lower than one millimeter.

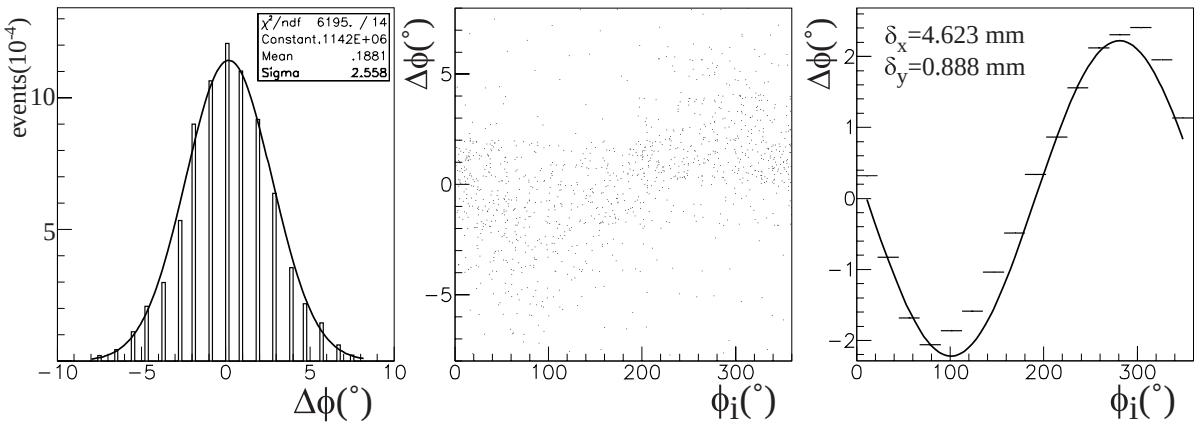

Figure 3.27: *Effect of the beam misalignment on the azimuthal resolution of the cylindrical MWPCs. On the left the difference between the azimuthal angles of the internal and external chambers. In the centre its evolution as a function of the ϕ_i of the internal function. On the right its fit with the function (3.13).*

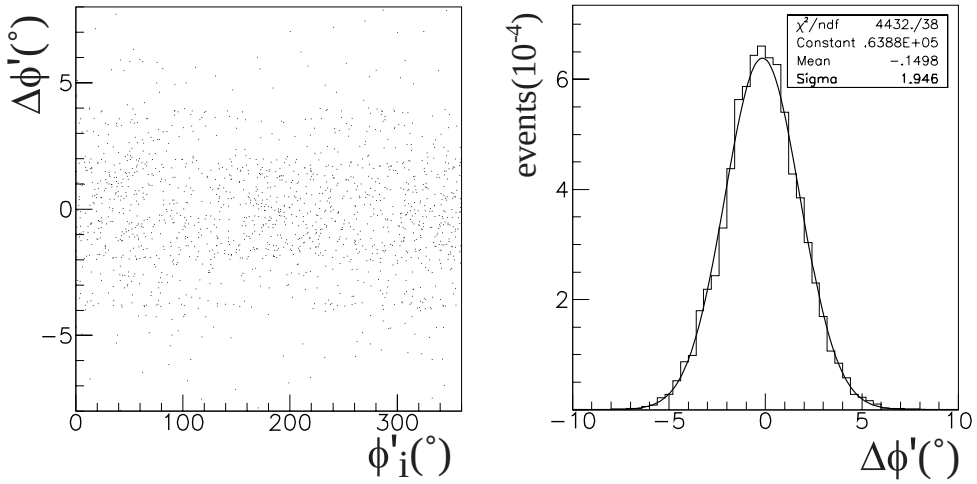

Figure 3.28: *Effect of the correction of the beam misalignment: on the left the evolution of $\Delta\phi'$ as a function of ϕ'_i is now constant. On the right the dispersion of $\Delta\phi'$ is now comparable to the one from the simulation.*

3.5 Conclusions

The cylindrical MWPCs offer to the GRAAL experiment new performances for the detection of charged particles. The particular structure of the cathodes, which are composed of helicoidal strips, allows to identify the intersection of the charged particles with the two cylinders.

After a general description of their structure as well as of their acquisition system, we have exposed the algorithms for the track reconstruction. We have underlined that the key problems for the reconstruction are the proper choice of the cut on the azimuthal angles of the track, measured by the two chambers, and the definition of their z coordinates with their cuts. The previous cuts have been compared to the simulation and we discovered that, while for $\Delta\phi$ simulation and data agree, the Δz value is unrealistic in the simulation. This effect produces as consequence an unrealistic polar resolution. As preliminary result we showed that a new, more realistic, description of the shower mechanism in the gas chamber produces a Δz that is almost equal to the experimental one. This result has still to be tested on the analysis but an improvement on the chamber efficiency is expected.
The efficiency of the single track reconstruction has been calculated on both the data and the simulation of the π° photoproduction (which is identified without the use of the cylindrical chambers) and a global 90% (data) and 95% (simulation) of the protons are detected. We have, hence, estimated the efficiency for the two and three particle reconstruction: we noticed an improvement (form 45.5% to 71.6% in the two track case and from 23.0% to 57.2% for the three track case) if we apply the procedure that separates the overlapped clusters on the cathodes.
We have then reviewed some main performances of the cylindrical MWPCs. The first one is the vertex reconstruction, which allows to use longer targets for reactions with lower cross section as the kaon photoproduction. As first result, in fact, we considerably improve the invariant mass width of the π° ($\simeq 8\%$) and of the η ($\simeq 6\%$) in the η decay into π^+, π^-, π°. As second result we can reconstruct the reaction and decay vertices of the $K\Lambda$ photoproduction, from which the life time of the hyperon can be calculated (and eventually used as selection cut for further analyses). Finally we showed how the eventual beam misalignment can be identified and subtracted by the measurement of the azimuthal angles of the track in the two chambers.
In conclusion, further improvements can be obtained with the new simulation, notwithstanding the global efficiency and spatial resolution of the cylindrical MWPCs are well defined to allow the reconstruction of channels with three charged particles in the final state or, as well, with low cross section.

Chapter 4

Data analysis

Introduction

In the first Chapter we pointed out the interest of studying the strangeness photoproduction. In particular we showed the recent measurements of the $K\Lambda$ cross section, effectuated by the SAPHIR collaboration, and its theoretical analysis in the framework of the isobaric models. Therefore we decided to measure the beam asymmetry observable of this reaction (reported in Chapter 5) in order to test if it could impose some constraints on the models. In this Chapter we will analyse the $K\Lambda$ photoproduction from its charged decay:

$$\vec{\gamma} + p \rightarrow K^+ + \Lambda \rightarrow K^+ + \pi^- + p \tag{4.1}$$

The main difficulty of this channel lies in the detection of three charged particles. Up to now the Graal program concerned only channels with one charged particle; this new analysis on the contrary requires an optimization of the track detectors for the charged particles. The installation of the cylindrical MWPCs in 1998 has allowed to reconstruct such complicated reactions. In Chapter 3 the optimization of the software of the reconstruction of the cylindrical MWPCs is reported and we have given an estimation of their efficiency and spatial resolution. We can thus use them to reconstruct this channel and the analysis procedure will be illustrated in this Chapter.
In order to test the performances of the cylindrical MWPCs we decided at first to study the η photoproduction with its charged decay:

$$\vec{\gamma} + p \rightarrow \eta + p \rightarrow \pi^+ + \pi^- + \pi^o + p \tag{4.2}$$

The η decay into two photons (branching ratio 39.21%) has already been analysed by the Graal collaboration and the beam asymmetry has been measured [15, 51, 66]. The new beam asymmetry that we will extract from the decay (4.2) in Chapter 5 will therefore be compared to the one extracted from the neutral decay. In this way the beam asymmetry will constitute a test of the analysis methods, that reconstruct the kinematics of channels with three charged particles, which are based on the informations from the cylindrical MWPCs.

Moreover, the reaction (4.2) has the same final state of the photoproduction as the ω meson:

$$\vec{\gamma} + p \rightarrow \omega + p \rightarrow \pi^+ + \pi^- + \pi^o + p \tag{4.3}$$

The theoretical study of the ω photoproduction is more complicated (the ω being a vector meson), as well as interesting, but in this thesis we will not measure its polarisation observables. Notwithstanding its charged decay mode is identical to the η one and testing its reconstruction efficiency is of great interest for further developments. The analysis of the ω channel will be thus reported in this Chapter.

From now on, in this Chapter, we will refer to the decays (4.1), (4.2) and (4.3) by calling them $K\Lambda$, η and ω, without specifying, for simplicity, the decay mode.

In the first Section the analysis of the detector responses is reported while in Section 2 we select the channel from the number of charged and neutral particles. In Section 3 we explain the two different analysis methods and the variables for the kinematic selection are reported in Section 4. In Sections 5 and 6 the results of these analyses are shown for the three channels above mentioned and we will estimate the analysis efficiency in section 7.

4.1 Preanalysis

In this Section we describe how each event is preanalysed to get information about the energy of the incident photons and the information (θ, ϕ, E or ΔE, T) associated with the detected charged and neutral particles. The preanalysis differs between forward ($\theta \leq 25°$) and central ($25° \leq \theta \leq 155°$) detectors[1], therefore we will treat these two cases separately.

[1]The geometrical and performance description of all the detectors is reported in Chapter 2

Tagging detector

The tagging system detects the electrons that have undergone Compton scattering and provides the identification numbers of the hit μstrips. The identification number of the hit plastic scintillators traversed by the electrons is also provided, together with their time response (TDC[2]).

As explained in Section 2.3.3 on page 24, the selection criteria applied on the response of the tagging detector are chosen as follows: only signals from plastic scintillators having timing information in the interval defined for the true coincidence are retained. For each selected plastic scintillator the time signal must be detected in the larger plastic scintillators in coincidence with one, or two adjacent ones, among the eight smaller scintillators. In addition, only one cluster, composed of adjacent hit μstrips, in geometrical coincidence with the smaller scintillators, is singled out.

Such a criterion allows to select only events in geometrical and time coincidence, corresponding to single hits. The photon energy is calculated from the cluster centre, measured on the μstrips, which corresponds to the position of the scattered electron. The photon energy is calculated as shown in Section 2.3.3. In addition the tagger position is chosen in each period of data taking in order to have the largest available energy spectrum for the channels to be analyzed.

Forward detectors

In the forward region the emission angles (θ, ϕ) of the charged particles are measured by the planar MWPCs, their energy loss and time of flight by the hodoscope. The planar MWPCs are composed of four planes of wires. A crossing particle can give a signal on one or more wires so that for each plane the hit wires are organized into clusters. The number of particles is, thus, given by the number of best associations among at least three planes out of the four planes.

The hodoscope response is, then, analyzed. For each bar i the subtraction of the pedestal PED_i and the conversion factor KC_i (mV/ADC[3]) and KT_i (ns/TDC) are applied on the ADC and TDC values measured by the photocathodes at the two sides of the bar (A and B):

$$U_i^{A,B} = KC_i^{A,B} \cdot (ADC_i^{A,B} - PED_i^{A,B})$$

[2]Time to Digital Converter

[3]Analog to Digital Converter

$$T_i^{A,B} = KT_i^{A,B} \cdot TDC_i^{A,B} - \frac{KW_i^{A,B}}{\sqrt{U_i^{A,B}}} - S_i^{A,B}$$

The TDC signal is also corrected to take into account the walk effect (KW_i), due to the leading edge discriminator, and the delay (S_i), due to the light propagation along the plastic scintillator. The energy loss and time of flight of each bar are then calculated from:

$$\Delta E_i = KPM_i^A \cdot \frac{U_i^A}{Att_i^A} + KPM_i^B \cdot \frac{U_i^B}{Att_i^B}$$
$$\Delta T_i = \frac{1}{2}(T_i^A + T_i^B - T_{prop})$$

where KPM_i is the conversion factor MeV/mV, $T_{prop} = l/V$ is the time taken by the light to cover the bar length and Att_i is the attenuation factor for the light along the distance to reach the photocathode.
The association between the hodoscope and the planar MWPCs is accomplished by projecting each track, detected by the chambers, on the plane of the hodoscope. If the corresponding horizontal and vertical bars have a signal, their response is associated to the track. Otherwise, the closest neighbour bars are analyzed. Since the particle can stop in the first layer, if there is a signal only in this layer, its value will be recorded and associated.
Neutral particles are detected by the shower wall which can distinguish between photons and neutrons by the time of flight information. The photon energy measured by the shower wall has low energy resolution and cannot be used in our kinematical selections. For this reason the shower wall response is only used as a veto for reactions in which the neutral particles are exclusively photons: in the particular case of the η and ω analyses we do not consider events which have at least one photon in the shower wall.

Central detectors

The central detectors are composed of the BGO calorimeter, the cylindrical MWPCs and the barrel. The information from the BGO crystals is analysed by reconstructing the clusters with the border method: each cluster is composed of adjacent crystals. Actually, the number of clusters can vary as a function of the applied energy threshold on each crystal, because clusters belonging to different particles can overlap. This effect is controlled by the simulation, so that we can estimate the number of overlaps occurring in a

given reaction. In our analysis we thus decided to apply a software threshold of 10 MeV to each crystal. The center of gravity of the cluster provides the polar and azimuthal coordinates of the particle with respect to the origin (target centre). The ADC signal of each crystal is converted into energy and a correction constant is applied in order to include non linear effects, which are relevant at higher energies. The cluster energy is the sum of the energies of all its crystals.

The ADC signal from each scintillator bar of the barrel is read and only the bar ADC signals above a fixed threshold are converted into energy. The conversion factor is calculated by comparing the simulated and real distributions of the proton energy in the π° photoproduction: the center of gravity of the experimental distribution can, in fact, drift, as a function of the photomultiplier gain variations; the difference between the calculated and simulated centres of gravity constitutes, therefore, the correction factor. The signal from the TDC is read and converted into time.

The number of tracks detected by the cylindrical MWPCs is reconstructed as follows: for each track a signal is required on all the four cathodes and one or two wires on each chamber. The algorithm of the association between cathode and wires and between the two chambers has been explained in Section 3.2. The cartesian and cylindrical coordinates are so recorded for each track.

Once the response of the three detectors has been analyzed, the identification of the number of neutral and charged particles is divided in two steps. At first the anticoincidence between the BGO and barrel classifies the clusters into charged or neutral: for each hit barrel bar, a program looks for the BGO cluster whose centre of gravity is in geometrical coincidence with it; if the association is successful the cluster is classified as "charged" (as "neutral" in the opposite case). The number of neutral particles is thus equal to the number of neutral clusters. The number of charged particles in the central detectors is provided by the association between the cylindrical MWPCs and the barrel. For each track in cylindrical MWPCs the program checks if the ADC of the barrel bar with the same ϕ has given a signal: the number of charged particles is thus equal to the number of successful associations.

4.2 Selection of the reaction channel

In this Section we will present the selection methods used for the channels with three charged particles, η, ω and $K\Lambda$: first we present the method for the identification of the π° (concerning the η and ω channels) and then the selection of the charged particles in the whole Lagranγe detector.

4.2.1 Selection of the neutral pion (η and ω channels)

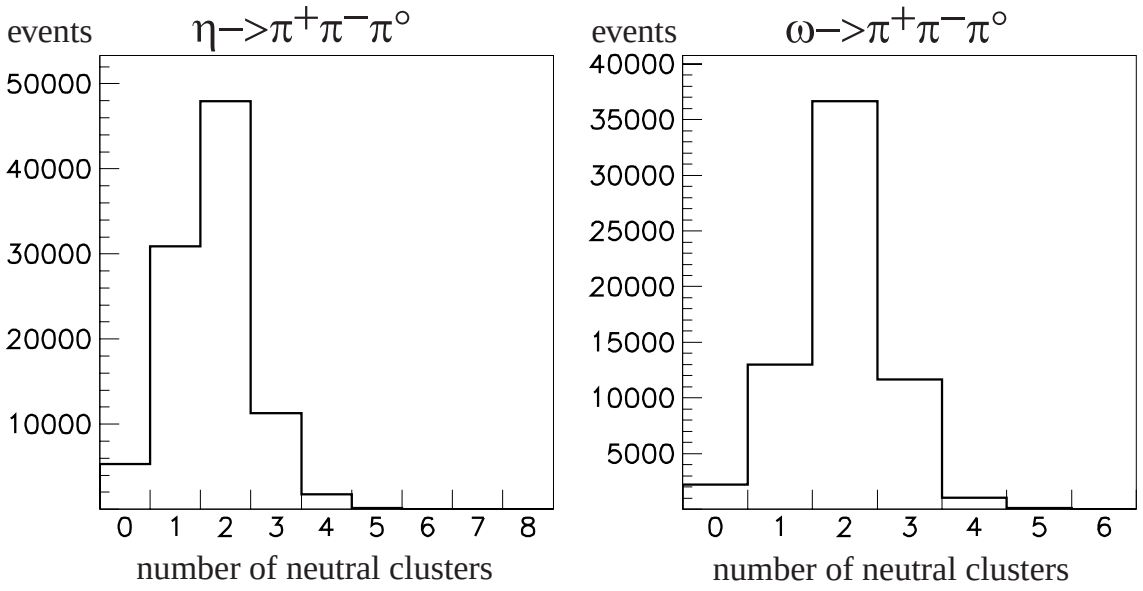

Figure 4.1: *Number of neutral clusters measured by the BGO for the η and ω decays. Both photons from the π^o decay are expected in the BGO, but only the $\approx 60\%$ and $\approx 50\%$ of the events for the η and the ω respectively have two neutral clusters in the calorimeter.*

The η and ω analyses are focused on events in which both photons from the π° decay are detected in the BGO. This limitation is due to the low energy resolution of the photons detected by the shower wall. Hence by eliminating events with at least one photon outside of the geometrical acceptance of the BGO we loose about $27\%(\eta)$ and $42\%(\omega)$ of the events but we preserve the resolution of the kinematical variables for the further selections.
The simplest way to select events with both photons in the central detectors is to have only two neutral clusters in the BGO. However, the simulations performed on the η and the ω channels show (see figure 4.1) that, when both photons are expected in the BGO, we can also observe either one or more than two neutral clusters. These effects are due

to different reasons: 1) some secondary electrons or photons from a developing shower could be emitted at large angles from the direction of the primary particle, giving rise to a secondary cluster, in time with the experimental trigger; 2) some secondary neutral particles could be produced in a crystal and not interact in the neighbour ones but further away, without getting out of the calorimeter, thus breaking the contiguity of energy release and creating more than one cluster; 3) in several cases, strictly related to the nature of the reaction channel, two or more individual particles could begin their interaction in near crystals and the showers that they individually develop could merge to some extent. These aspects have been widely studied [67, 68] and are linked to the cluster reconstruction method. It is necessary, therefore, to distinguish cases with one or two/three clusters and analyze them separately.

Cases with two or more cluster

In figure 4.1 the number of neutral clusters per event when both photons are expected in the BGO is shown for the η and the ω: a non-negligible part of them (13% for the η and 20% for the ω) have more than two clusters. This may be due to the reasons previously explained. In these cases the best procedure is to consider all the possible neutral cluster pairs and to choose the best combination, that is the one which provides an invariant mass as close as possible to the π° mass.
For each cluster pair we know the energy, E_{γ_1} and E_{γ_2}, and the angular coordinates of their center of gravity, $(\theta_{\gamma_1}, \phi_{\gamma_1})$ and $(\theta_{\gamma_2}, \phi_{\gamma_2})$. The pion energy, momentum and invariant mass can thus be calculated as follow:

$$\begin{aligned} E_{\pi^o} &= E_{\gamma_1} + E_{\gamma_2} \\ \boldsymbol{P}_{\pi^o} &= \boldsymbol{P}_{\gamma_1} + \boldsymbol{P}_{\gamma_2} \\ M_{\pi^o} &= \sqrt{E_{\pi^o}^2 - \boldsymbol{P}_{\pi^o}^2} \end{aligned} \tag{4.4}$$

where, for each photon:

$$\begin{aligned} P_{x_{\gamma_i}} &= E_{\gamma_i} \sin\theta_{\gamma_i} \cos\phi_{\gamma_i} \\ P_{y_{\gamma_i}} &= E_{\gamma_i} \sin\theta_{\gamma_i} \sin\phi_{\gamma_i} \\ P_{z_{\gamma_i}} &= E_{\gamma_i} \cos\theta_{\gamma_i} \end{aligned}$$

Some particular events with three photons can give more than one possible solution (this is a very rare case), that is to say two pairs of photons can give an invariant mass which is close to the true π° mass. In this case we will consider both pairs, we will solve the

equations of the energy and momentum conservation of the three charged particles and we will finally select the pair which best satisfies the energy conservation.

Cases with one neutral cluster

This case (23% for the η and 26% for the ω as shown in figure 4.1) is theoretically easier to be understood but it is more difficult to be solved, because the π° invariant mass cannot be calculated. The main problem is that the background of such events is greater because the cut on the π° mass cannot be applied. Hence, our main concern is to test if this case consistently improves the efficiency without increasing the background events.

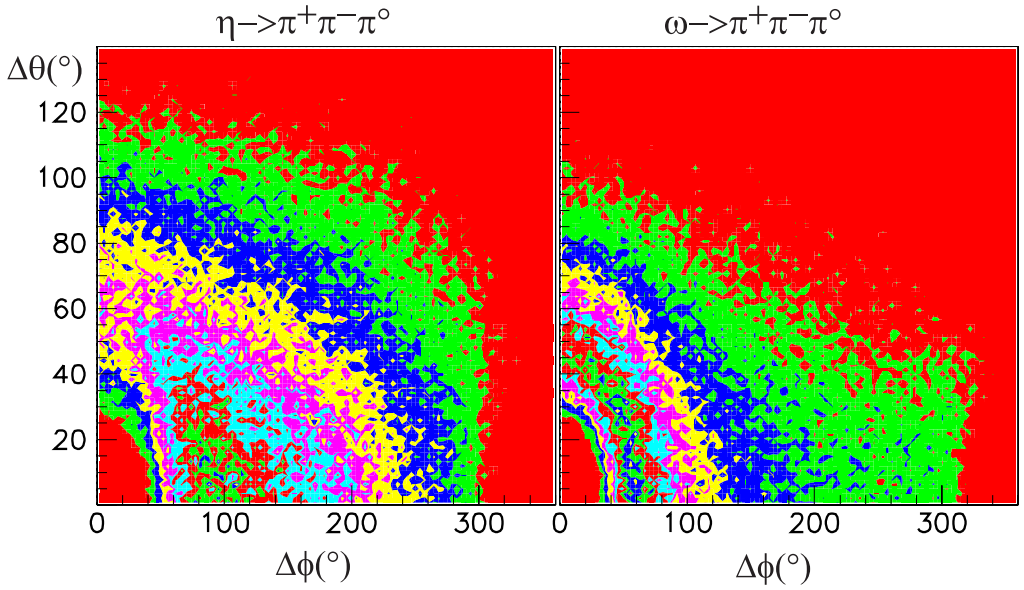

Figure 4.2: *Angular distribution, $\Delta\phi = \phi_{\gamma_1} - \phi_{\gamma_2}$ and $\Delta\theta = \theta_{\gamma_1} - \theta_{\gamma_2}$, of the photons in the BGO for the π^o decay of the η (left) and ω (right) photoproduction.*

In order to understand the origin of a single cluster in the π° decay, we show in figure 4.2 the polar and azimuthal differences between the two simulated photons from the π° decay in the η and ω cases respectively, when both photons are expected in the BGO. As we can see the lowest difference is about 25° for θ and $35 - 40°$ for ϕ in both reactions. If we consider that the BGO angular resolution is about 6° in θ and 7° in ϕ, events with a cluster overlap are rare. Hence, if we neglect the cluster overlapping, a neutral cluster alone means that the other photon has been lost because of its too low energy, the software threshold being fixed at 10 MeV. We expect, then, that the energy measurement is underestimated of 10 MeV at the most, while the θ and ϕ reconstruction is affected by

the loss of a low momentum particle.
For such events the θ, ϕ and the energy of the π° correspond to the ones of the single photon. The kinematical reconstruction of the event can be only achieved by the second of the two analysis methods that we are going to describe in the next Section. In this method the neutral pion energy is calculated by the linear system (4.8). In this way an expected value, $E_{\pi^\circ_c}$, for π° energy can be extracted. The event selection is, hence, on the absolute value of the difference between the calculated energy $E_{\pi^\circ_c}$ and the measured one, $E_{\pi^\circ_m}$.

4.2.2 Selection of the charged particles (η, ω and $K\Lambda$ channels)

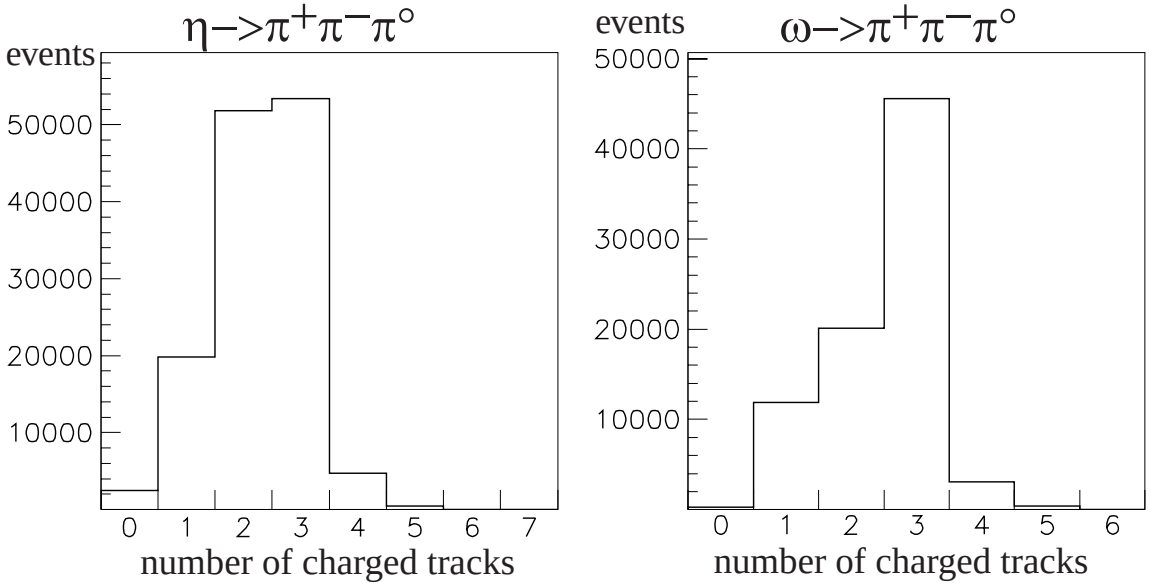

Figure 4.3: *Number of charged tracks detected by the MWPCs and the plastic scintillators for the η and ω decays. The charged particles are awaited either in the planar MWPCs and the hodoscope or in the cylindrical MWPCs and the barrel. For about 56%(η) and 39%(ω) of the events the total number of charged particles is lower than three. About 4% (η) and 5% (ω) of the events have more than three charged particles.*

The simulated total number of charged particles detected by the MWPCs and the plastic scintillators (as explained in the previous Section) for the η and ω channels are represented in figure 4.3. Only events with the three particles emitted in the geometrical acceptance of the detectors are selected. We observe the presence of some events with four or five charged tracks in the detectors. This may be caused either by a bad identification of

the neutral particles or by electromagnetic background due to the BGO calorimeter or to the chamber cathodes noise. Therefore, the analysis of the event kinematics will consider cases with three or four charged particles: for each event all possible permutations of the three particles are considered and the one which best satisfies the energy and momentum conservation is retained.

4.3 Kinematics analysis methods

In the following we shall explain the two methods used for the kinematic analysis; the kinematical variables will be, then, defined in order to apply the selection cuts.
In both methods we use the angles θ and ϕ of the three charged particles, measured by the MWPCs (π^+, π^-, p for η and ω and π^-, K, p for $K\Lambda$) and the measured energy of the incident photon.
In the η and ω cases the informations on the π° are differently used according to the two methods: in the first one the π° energy and momentum are estimated with equations (4.4) by the knowledge of the photon angles and energies, both measured with the BGO calorimeter, as previously said; in the second one we use only its angles θ and ϕ and we hence calculate the expected values of its energy and momentum.
The general aim of both methods is to solve the equations of the energy and momentum conservation and to get the expected momenta and energies for the three charged particles, together with their identification (p, K, $\pi^\pm$). Later on, we can use these values to calculate the missing and the invariant masses (η, ω or Λ) together with the expected time of flight (ToF) and energy loss (ΔE) of the three charged particles.
We emphasize that the particle identification is provided by the difference between the expected and the measured ΔE and ToF. The traditional selections based on the comparison $\Delta E, E$ or $\Delta E, T$ are, in fact, not suitable for large momentum ranges, which produce overlaps among the particles. The method we use allows to compare the measured and the expected values of the energy loss and time of flight of the three charged particles. The permutation which best satisfies these requirements, by preserving as well the energy conservation, is thus selected.

4.3.1 First method: the three body system

The following systems are solved:

$$\begin{cases} E_{\pi_1} + E_{\pi_2} + E_p &= E_\gamma + m_p - E_{\pi_o} \qquad \text{for the } \eta \text{ and } \omega \\ \boldsymbol{P}_{\pi_1} + \boldsymbol{P}_{\pi_2} + \boldsymbol{P}_p &= \boldsymbol{P}_\gamma - \boldsymbol{P}_{\pi_o} \end{cases} \tag{4.5}$$

or

$$\begin{cases} E_\pi + E_k + E_p &= E_\gamma + m_p \qquad \text{for the } K\Lambda \\ \boldsymbol{P}_\pi + \boldsymbol{P}_k + \boldsymbol{P}_p &= \boldsymbol{P}_\gamma \end{cases} \tag{4.6}$$

The angles of the three charged particles and E_{π° and $\boldsymbol{P}_{\pi^\circ}$ from equations (4.4) are used to solve the equation for the momentum conservation for each possible permutation of three charged particles (3! or 4! possibilities for three or four charged particles respectively). The minimization on the energy conservation will allow to choose which permutation is the best solution, providing, in this way, a first identification of the particles.

Once the kinematics is defined we calculate the expected values of ΔE and ToF (the latter for the forward charged particles only) and compare them to the ones measured by the detectors (their extraction will be explained in the following Section). These procedures determine if it is necessary to reject the solution and to take a new one with a worse (but reasonable) energy balance and a better value for the mass and the energy loss (or time of flight).

4.3.2 Second method: three and two body systems

This method is divided into two steps: **the first step** (the two body system) uses, as the only known parameters, the polar angle θ of the proton (for the η or the ω photoproduction) or the kaon (for the $K\Lambda$ photoproduction) and the incident photon energy E_γ. Starting from these measured values, the equations for the energy and momentum conservation are solved to calculate the energy E_X of the intermediate particle (η, ω or Λ):

$$\begin{cases} E_X + E_{p,K} &= E_\gamma + m_p \\ \boldsymbol{P}_X + \boldsymbol{P}_{p,K} &= \boldsymbol{P}_\gamma \end{cases} \tag{4.7}$$

By first squaring and then subtracting both equations and by squaring again, we obtain a simple second order equation in the energy $E_{K,p}$. Two physically correct solutions are

in general possible. This is the case in which the meson velocity in the centre of mass of γ, p system is lower than the velocity of center of mass itself. If it is greater there will only be one solution. Each possible solution gives a value to P_X which is identified as η, ω or Λ:

$$\begin{aligned} \boldsymbol{P}_X &= -\boldsymbol{P}_{K,p} \\ E_X &= \sqrt{\boldsymbol{P}_X^2 + M_i^2} \qquad \text{where } i = M_\eta, M_\omega, M_\Lambda \text{ is the true mass of } X \end{aligned}$$

The two possible solutions $E_X, \boldsymbol{P}_X$ are used (**second step**) in the η and ω cases to solve the energy and momentum conservation of the decay products of the particle X:

$$\left\{ \begin{array}{rcl} E_{\pi_1} + E_{\pi_2} + E_{\pi^o} &=& E_X \\ \boldsymbol{P}_{\pi_1} + \boldsymbol{P}_{\pi_2} + \boldsymbol{P}_{\pi^o} &=& \boldsymbol{P}_X \end{array} \right. \tag{4.8}$$

where we use the angles measured from the MWPCs for π_1 and π_2 and those of the π° from equation (4.4). These equations are solved as those of the previous method: for each possible solution (E_X,$\boldsymbol{P}_X$) we will have different possible combinations of the two charged pions. The selection is, therefore, applied on the energy and momentum conservation of the three body system. We observe that, in this method, we will evaluate an expected value for the π° energy, that will be a further kinematical variable for the cuts, by comparing its value with the measured one.
The **second step** for the $K\Lambda$ channel is to solve for each possible (E_X,$\boldsymbol{P}_X$) the two body problem, that will give the expected momenta and energies for the pion and the proton of the Λ decay:

$$\left\{ \begin{array}{rcl} E_\pi + E_p &=& E_\Lambda \\ \boldsymbol{P}_\pi + \boldsymbol{P}_p &=& \boldsymbol{P}_\Lambda \end{array} \right. \tag{4.9}$$

These equations are solved as the (4.7) ones but, in this case, we use the measured polar angle of the remaining two charged particles (π, p). The second order equation in energy is, then, separately solved for the proton and the pion. We obtain, hence, two solutions for the proton and two for the pion. The best solution is the one that gives the best momentum balance for the following quantity:

$$| \Delta p_x | + | \Delta p_y | + | \Delta p_z | \;=\; 0 \tag{4.10}$$

4.4 Variables for the kinematical selection

The described solution of the previous equations provides the momenta of the three charged particles, allowing their identification. Once the events with no kinematical solutions have been rejected, we proceed to select the events for which the total energy and momentum are conserved. Further selections can be achieved by using the global variables, as the invariant and missing masses and also the expected energy loss and time of flight for each charged particle, which are extracted from the system solutions. The time of flight and energy loss in the forward direction can, as well, be used to calculate the real mass of the charged particle, which will constitute a further selection on the events. In the following we will explain how we define and calculate each cut for the event selection.

Energy and momentum conservation (channel selection)

As previously explained, in both methods we apply the momentum conservation law, to calculate the momenta of the charged particles as a function of their angles. We identify the three particles by choosing the solution that better satisfy the energy conservation law. After that we apply selective cuts on the energetic balance to separate the reaction from the background. In the $K\Lambda$ case the events from the second method are selected by equation (4.10).

π° invariant mass (neutral particle identification)

For the η and ω channels the π° is identified by the selection on its invariant mass:

$$m_{\pi^\circ} = \sqrt{E^2_{\pi^\circ} - \boldsymbol{P}^2_{\pi^\circ}} \tag{4.11}$$

where, as we said, E_{π° and $\boldsymbol{P}_{\pi^\circ}$ are calculated from the photon angles and their energies measured by the BGO. As we previously said, if there are at least three photons, the different combinations can give a value for the π° mass close to the true one. In this case the energy balance will select which among these combinations best satisfies the energy conservation.

The solution of the second method gives the calculated value of the pion energy and its difference with the measured one provides the second cut:

$$E_{\pi^\circ_c} = E_{\pi^\circ_m} \tag{4.12}$$

The importance of the cut (4.12) is to understand if we are able to select, with a low background, events from the η and ω decay, where only a single photon has been detected in the whole apparatus (and the other one is supposed in the geometrical acceptance of the BGO, but it has been lost). We will, then, face this case in the efficiency and background Section.

Energy loss, time of flight and real masses of the three charged particles (charged particle identification)

At this step we can use the informations coming from the plastic scintillators in order to verify if we selected the true charged particles. Energy loss and time of flight are a function of the particle momentums:

$$\begin{aligned} \Delta E &= \int_{\Delta x} \frac{dE}{dx}(p)\, dx \\ ToF &= T_{light}\frac{\sqrt{m^2+p^2}}{p} \quad , \quad T_{light} = \frac{l}{c} \end{aligned} \tag{4.13}$$

where dx is the thickness of scintillator crossed by the particle, l is the distance of the plastic scintillator from the target and T_{light} is the time of the light to cross the distance l. If the particle momentum is high enough, the variation of the energy loss can be neglected and the simplest form can be used:

$$\Delta E = \left(\frac{dE}{dx}\right)\Delta x \tag{4.14}$$

By using equations (4.13) and (4.14) we can calculate, for each particle and from the calculated momentum p_c, the expected values for the mass, m, the time of flight, ToF_c, and the energy loss, $(dE/dx)_c$. In the forward direction we calculate:

$$\begin{aligned} m &= p_c\sqrt{(ToF/T)^2-1} \\ (ToF)_c &= T_{light}\sqrt{(m_0/p_c)^2+1} \\ \left(\tfrac{dE}{dx}\right)_c &= f(\beta\gamma) = h_1\left(\frac{2\log(\beta\gamma)+h_2-\Delta}{\beta^2}-1\right) \end{aligned} \tag{4.15}$$

where the mass m is calculated using the measured ToF and m_0 is the true mass of the expected particle. The expression for the energy loss is calculated as a function of the momentum variable $\beta\gamma = p_c/m_0$, where we have defined:

$$\begin{cases} \Delta = & 0 & \text{if } x < (x_0 \log 10) \\ \Delta = & \frac{1}{2}\left(2x + c + a\left(x_1 - \frac{x}{\log 10}\right)\right) & \text{else} \end{cases} \tag{4.16}$$

and

$$x = \log \beta\gamma;$$

$$x_0 = 0.1464;\ h_1 = 0.1754\ MeV/cm;\ h_2 = 9.504;\ x_1 = 2.49;\ c = -3.2;\ a = 0,1610$$

In the barrel (central part) the particle mass is estimated, with a lower resolution, with an approximated Bethe-Block formula, obtained from the fit of simulated data:

$$m = \sqrt{\left(\frac{dE}{dx} - a\right)\frac{p_c^2}{b}} \tag{4.17}$$

where $a = 1.664\ MeV/cm$ and $b = 1.583\ MeV \cdot c^2/cm$. By using the previous equation we can calculate the pion and proton masses and we can also apply cuts on the differences between the measured and the calculated values of the time of flight and energy loss:

- ΔT for the forward charged particles;
- $R\left(\frac{dE}{dx}\right)$ for forward and central charged particles.

The three variables, m, ToF and ΔE are dependent and the mass value is thus used to check the other selections.

Invariant and missing mass

The following step is to construct the invariant, M_{inv}, and missing, M_{miss}, masses. The first is calculated from the products of the meson (η, ω) or baryon (Λ) decay, while the latter is determined by the proton (or kaon for the $K\Lambda$) detection (via its polar angle). The invariant mass, thus, is given by:

$$M_{inv} = \sqrt{E^2 - P^2} \tag{4.18}$$

where P and E are sum, respectively, of the momenta and energies of the decay products. The missing mass is calculated from equations:

$$M_{miss} = \sqrt{(E_\gamma + m_p - E_{p,K})^2 - \left({P_{p,K}}^2 + {E_\gamma}^2 - 2P_{p,K}E_\gamma \cos\theta_{p,K}\right)} \tag{4.19}$$

The invariant mass is calculated by using the kinematical solution of the two methods. In the first method, where there is no calculated value for $P(\pi^{\circ})$, we use the measured value of the momentum (calculated from the energy and the angles of the two photons). The missing mass can be calculated by using either the solution of the energy and momentum conservation or the measured ones. In the first case we will obtain M_{miss_c} by using E_c and P_c, the solutions of the energy and momentum equations of the two methods. In the second case we calculate M_{miss_m}, by using the energy and momenta extracted from the measured ToF and ΔE. M_{miss_m} is used only for events with the proton in the forward direction, because the measurement of the time of flight is better. The energy and momentum are thus given by:

$$P = \frac{m_0}{\sqrt{(ToF/T)^2 - 1}} \tag{4.20}$$

$$E = \sqrt{(m_0^2 + P^2)} \tag{4.21}$$

where m_0 is the true mass of the charged particle.

4.5 Selection on data from η and ω photoproduction

Let us see now the results of the data selection, previously explained, for the η and ω channels. We do not report the results of the second method if only one photon from the π° decay is detected in the BGO: the remarks concerning this particular case are reported in Section 4.7.

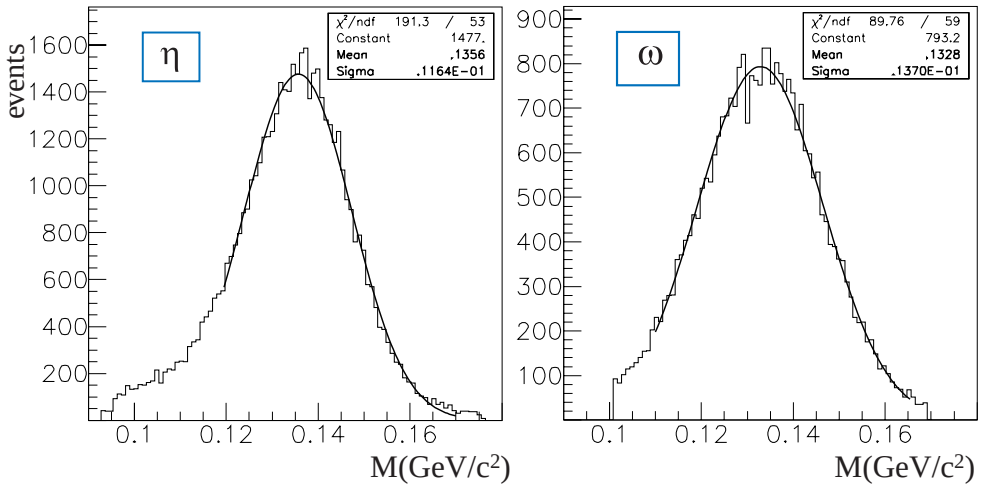

Figure 4.4: *π° mass on data for the η (left) and omega (right) channels.*

We show at first the cut on the π° mass in figure 4.4 for the η and ω channels, respectively. The Gaussian fit gives the same mean value for the two methods, but a difference of about 18% exists between the dispersion for the two channels: the width is in fact a function of the π° energy, whose distribution is different for the two reactions.

In figure 4.5 the identification of the charged particles for the η channel in the forward and central detectors, respectively, is shown. The result is similar for both methods. The proton resolution is worse than the pion one because of systematic effects of the scintillation mechanism inside the plastic scintillators. Furthermore, the proton mass in the central detector is a little underestimated. This may be due to the not perfect calibration of the barrel response. The energy measurement is, in fact, calibrated with the π° photoproduction (which does not cover the full bar length).

Let us see now the mass distribution of the charged particles in the ω channel. In this case we can merge the events containing pions detected in the forward and the central detectors, because the proton has been selected only in the forward direction. We emphasize, instead, the difference between the first (full line) and second (dashed line) method. As one can see, even if the efficiency of the second method is lower, it has a better resolution for

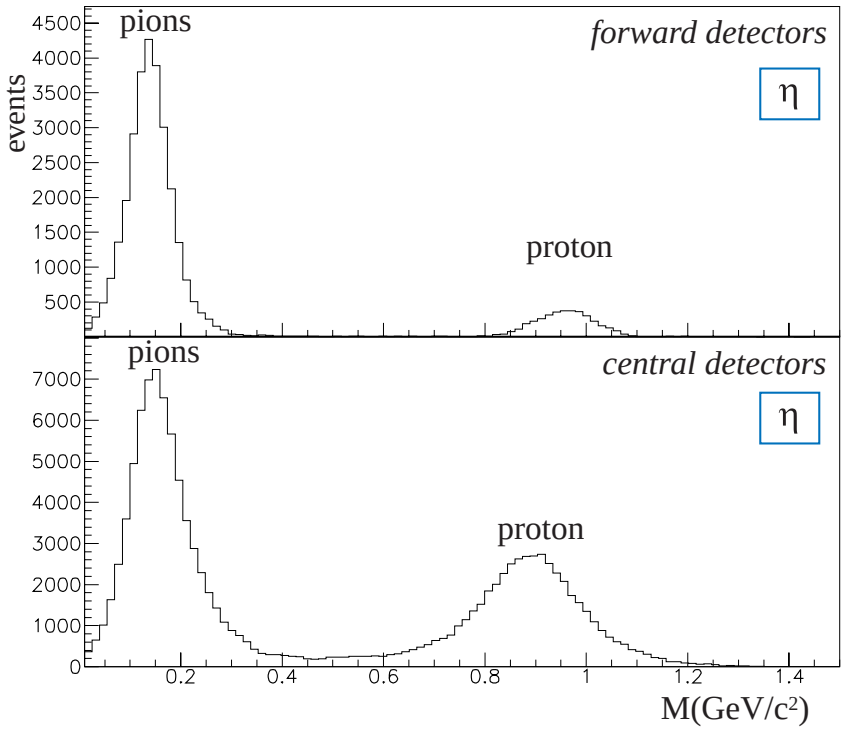

Figure 4.5: *Masses of the charged particles for the η channel. The forward and central detectors are shown separately.*

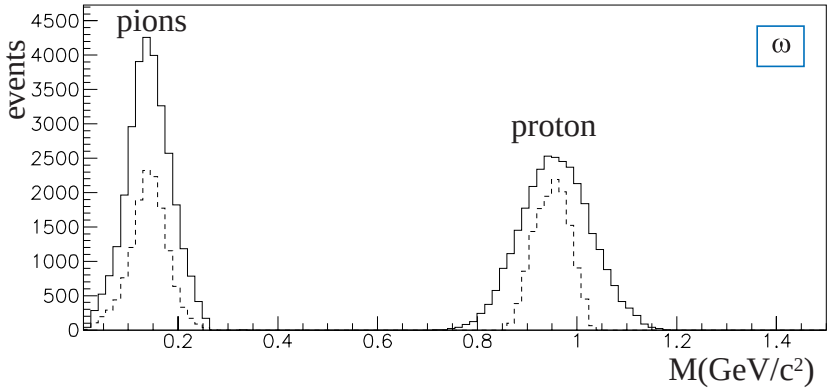

Figure 4.6: *Identification of the charged particles in the ω channel. The full line is the first method while the dashed line is the second one.*

the proton mass. This method, in fact, is based on the detection of the proton, which is better identified in the forward direction by the cut on its time of flight.

In figure 4.7 we show now the calculated invariant and missing masses for the η channel. The largest distribution (solid curves) of each plot are the masses after the selection of the decay products (π° mass, time of flight and energy loss of the π^+, π^- and proton).

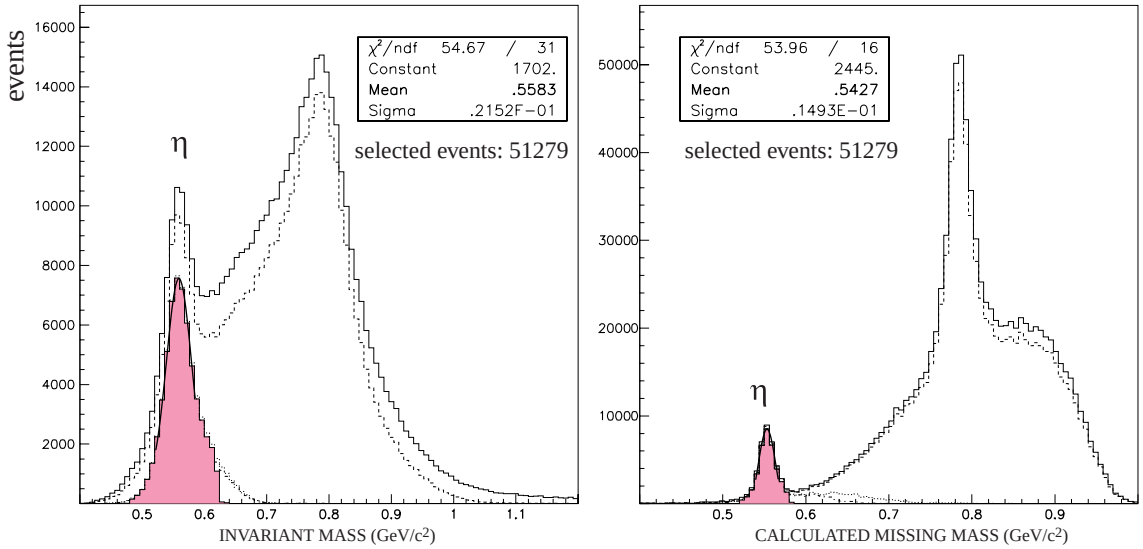

Figure 4.7: *Calculated invariant (on the left) and missing mass (on the right) for the η photoproduction. The result is from the first method (as we said the calculated missing mass is a delta for the second method).*

The superimposed curves are as follows: cut on the energy balance (dashed curves), cut on the calculated missing (dotted curve on the left) or invariant (dotted curve on the right) mass, cut on the measured missing mass (dashed-dotted curves). As one can see in both cases the η mass is properly reconstructed. These results are from the first method, whose efficiency (as we will see in the consecrated Section) is higher. The bold curves (filled histogram) are the fits to the final data, where a final cut on the calculated invariant (left) and missing (right) masses have been applied.

The same order of cuts is applied on the ω distributions of the invariant and missing masses in figure 4.8. In this case we observe that the peak height after that all the cuts have been applied is much lower. This effect is due to the fact that the selection is limited to events with the proton in the forward direction. A new cross section, with more realistic values for events with $\theta_p \leq 25°$, is recently available for the simulation analysis, that will allow to define the cuts for this kinematic region.

In both channels the main background is the direct photoproduction of π^+,π^-,π°,p as we can infer from the spectra as well as from the simulation (the background contribution will be discussed in the next section).

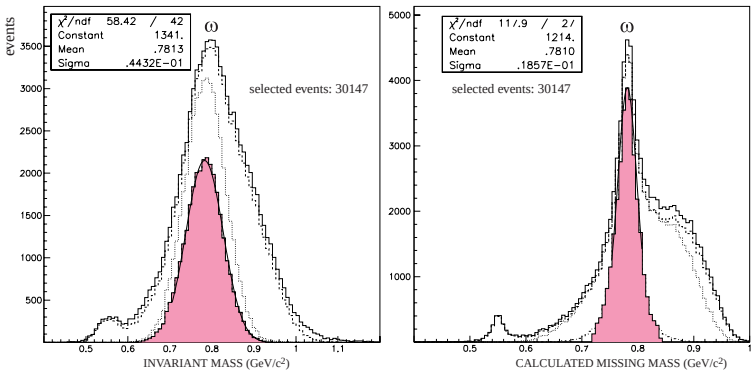

Figure 4.8: *Invariant mass (on the left) and calculated missing mass (on the right) for the ω photoproduction. The result is from the first method.*

4.6 Selection on data from $K\Lambda$ photoproduction

In the following we present the selection of the channel $K\Lambda$ [69]. In figure 4.9 we show the identification of the three charged particles, as detected in the forward (above) and central (below) detectors, respectively. The particles are properly identified even if we observe an underestimation of the kaon and proton masses in the central detectors: this is due to the same reasons explained in the previous Sections.

The calculated missing mass of the hyperon Λ is reported in figure 4.10. The hyperon is properly reconstructed with the same cuts of the previous channels (except for the π° mass). The efficiency is 8.8% and 11.4% for the first and second method, respectively, with a background of 10.7% and 7.9%. This background is estimated with the simulation and its main cotribution is given by the $\pi^+\pi^- p$ photoproduction.

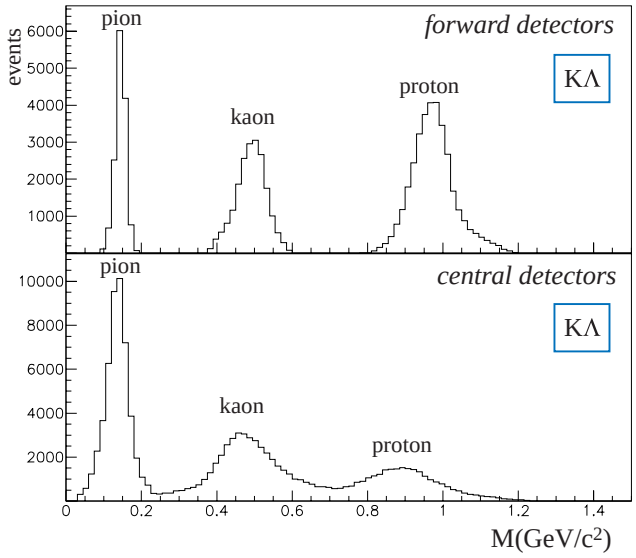

Figure 4.9: *Data selection of the charged particles in the $K\Lambda$ channel.*

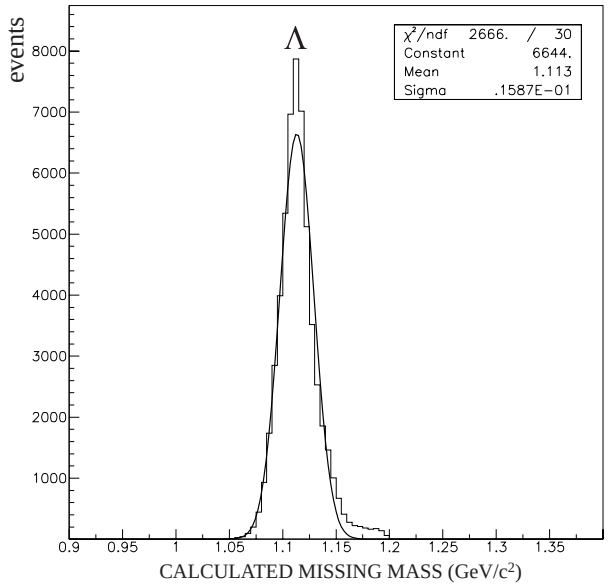

Figure 4.10: *Calculated missing mass of the hyperon Λ after all the selection in the first method case.*

4.7 The efficiency of the analysis procedure

The efficiency of a channel identification is the ratio between the number of selected events and the number of the expected ones. The reconstruction efficiency of a physical channel is function of different factors. At first each detector introduces its own inefficiency, which may be caused either by its intrinsic resolution or by the method used to reconstruct the signals in the detector itself. The geometrical efficiency is the second component, that is to say the Graal detector does not cover the whole solid angle. Last but not least, the analysis cuts, whose optimization plays the fundamental role in our concern, put limitations on the selection efficiency. We will consider the first two factors as "preanalysis efficiency" and we will treat them in the first part of this Section. In the second part we will discuss the efficiency of each method, by taking into account its evolution in function of the energy. In this Section we will treat the efficiency and background for the η and ω channels. A global efficiency for the $K\Lambda$ has been given in the previous Section.

4.7.1 Preanalysis efficiency

Tagging: the tagging detector analysis rejects events with two or more clusters on the strips. The value of the corresponding efficiency has been estimated [51] at about 65% (with respect to 100 electrons detected by the plastic scintillators), but it has to be considered on the whole Compton spectrum and, therefore, it also depends on the channel threshold.

Forward detectors: Neutral particles in the forward direction are rejected because the photon energy resolution of the shower wall decreases with the photon energy up to 100%. The fraction of rejected events in the π° reconstruction is about 27% for the η and 42% for the ω.

Central detectors: Both neutral and charged clusters produce a signal in more than one crystal of the BGO calorimeter. The center of gravity method looks for the highest energy among the crystals of the clusters. If there is more than one maximum in our analysis the event is rejected. The inefficiency due to this cut is very low: 1.1% and 2.4% on neutral clusters for the η and the ω, respectively; about 5.8% and 10.4% on charged clusters for the η and the ω, respectively.

Overall geometrical inefficiency: In figure 4.11 the planar and cylindrical MWPCs, the barrel and hodoscope scintillators are represented. It shows that a small region of inefficiency arises for angles $\Delta\theta = \theta_2 - \theta_1 \simeq 7^\circ$ between $\theta_1 = 19.5^\circ$ and $\theta_2 = 26.3^\circ$, when

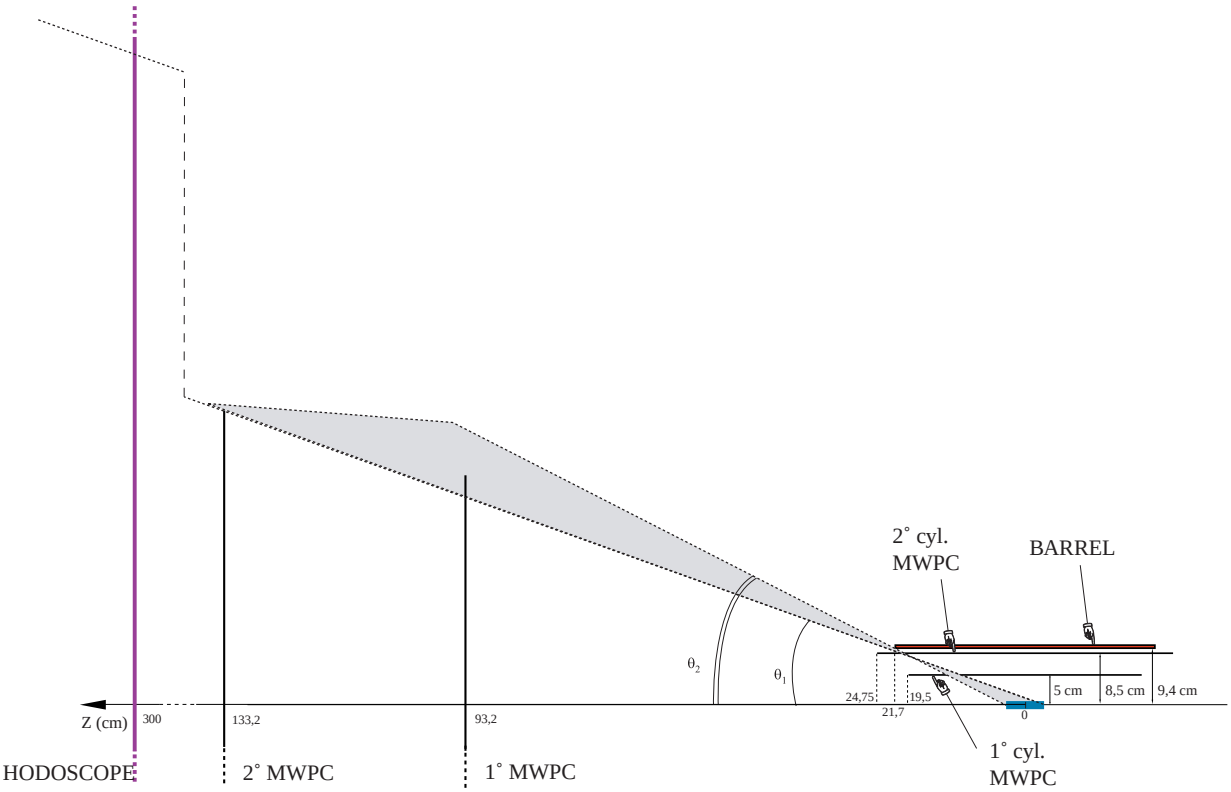

Figure 4.11: *Inefficiency region between the forward and the central detectors.*

the trajectories do not enter all the forward detectors. This inefficiency region has been recently recovered by the installation of a new greater planar MWPC. Anyway, data analyzed in this thesis concern the previous configuration, where this inefficiency plays an important role, as a considerable part of the proton distribution falls in it.

In the backward direction there is, as well, an inefficiency region, which is not covered by any detector (recently two scintillator disks have been installed for the detection and/or rejection of neutral and charged particles). The boundary of this region is symmetric with respect to the forward one and is therefore defined by $\theta_{back} = 180° - \theta_2 = 153.7°$.

Number of particles: as shown in figure 4.1, 23%(η) and 26%(ω) of the events have less than two clusters in the BGO, when both of the photons are expected in the calorimeter. Therefore we have decided to analyze also events with a single photon detected in the BGO. According to figure 4.3 about 53% η and 39% ω events have less than three charged particles, when three are expected. The ω efficiency in this case is better because most of the events are produced with a proton in the forward direction, that are subsequently selected by the analysis. For these events (with only a maximum of two pions in the

cylindrical MWPCs) we have a higher efficiency (as explained in Chapter 3). Finally, we will consider only events with the number of neutral cluster $n = 1, 2, 3$ and with the number of charged tracks $m = 3, 4$.
In conclusion, we can now estimate that the total efficiency at the preanalysis level is about 15% and 37% for the η and the ω respectively.

4.7.2 Analysis efficiency and background

As performed in the previous works [51], we estimated the efficiency and background from the simulation for the η and the ω channels. Previous Graal results [15, 66] have shown an excellent agreement between simulated and real data, thus confirming the good simulation knowledge. The background of the channels we are concerned with are nevertheless not well reproduced by the simulation. Both the η and ω channels presents the direct photoproduction of π^+, π^-, π° as the main background contribution. The cross section of this reaction is unknown and the theoretical predictions are difficult to be found. It is thus necessary, in this case, to evaluate at the same time the background components from the data. We will then give an estimation of this background, which will have to be studied more accurately if we deal with cross section measurements.
In table 4.1 we report the estimation of efficiency from simulated data for the different methods and for the two reactions.

Methods	$\eta \rightarrow \pi^+\pi^-\pi^o$	$\omega \rightarrow \pi^+\pi^-\pi^o$
Method 1	≈ 10 %	≈ 12 %
Method 2	≈ 3 %	≈ 2 %
Method2 (1 and 2 γ)	≈ 9 %	≈ 6 %

Table 4.1: *Summary of the efficiency for the η and ω decay for the three methods.*

The efficiency of both channels is lower with respect to the previous studied by the Graal collaboration. These two channels have in fact five particles in the final state and their efficiency is lower for the reasons explained in the previous paragraph. In general the first method works better, with higher efficiency. In the preanalysis paragraph we estimated an overall efficiency of 15% and 37% for the η and the ω respectively. The results presented in this table are, therefore, reasonable for the η but too pessimistic for the ω. A greater effort should then be done for the ω photoproduction to analyse also protons at larger angles.

In Chapter 4 we said that the second method can be also used when only one neutral cluster has been reconstructed in the BGO calorimeter. From table 4.1 we learn that in the ω case the second method with one or two neutral clusters considerably improves (from 1.5% to 6.0%) the efficiency in the ω channel. The same method for the η channel improves the efficiency but the background estimated from the data is greater than 50%. At this regard, we report in figure 4.12 the cut of equation (4.12), which compares the calculated and measured π° energy.

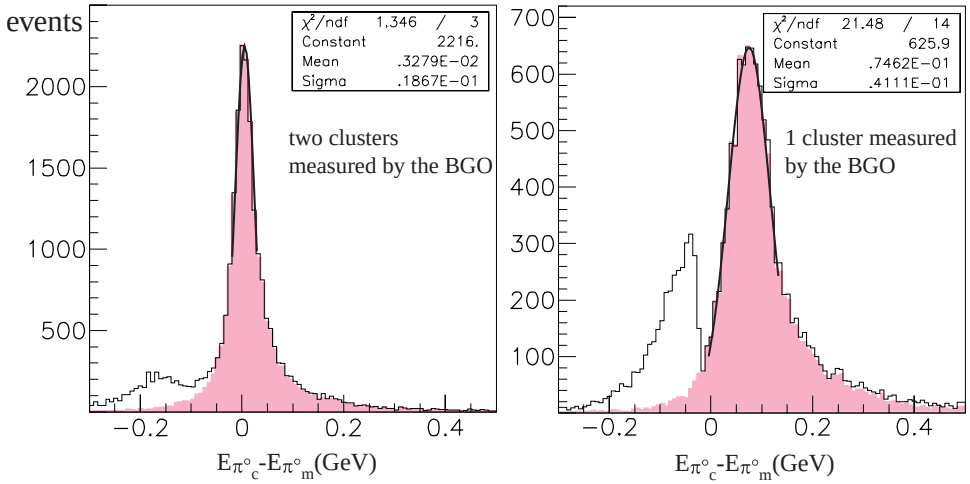

Figure 4.12: *Cut on the difference between $E_{\pi^\circ_c}$ and $E_{\pi^\circ_m}$ (see equation (4.12)). On the right events with only one of the two expected clusters from the π° decay are plotted. On the left the same difference for events with two clusters is shown. The full curves represent the same distribution after the cuts.*

On the left we show this cut for events with two or more clusters in the calorimeter, whose energy is fully measured by the BGO: in this case the distribution is centered around zero. On the right the same cut for events with a single cluster in the BGO is reported. We ascertain for the latter a shift on the right of about 70 MeV. The lost photon can, thus, have an energy up to 70 MeV. The selection of events with a single cluster can be, therefore, achieved with the cut shown in this figure, but the energy shift will cause a greater background noise in the selection of the reaction. The conclusion is that, for the η decay, we decided to use only events with two neutral clusters in the BGO.
The evolution of efficiency has been also studied as a function of the photon energy in the laboratory system. In the η case and in all the methods the efficiency decreases with the energy. The first method seems to be the most performing as we have already pointed out in the Section on the invariant mass.

As explained at the beginning of this paragraph, the confidence level of the simulation for these two reactions is lower than the one of the previous results of the Graal collaboration, in particular the neutral decays of the η and π°. So we have to estimate the background contribution from the data. We can calculate it from figures 4.7 on page 87 and 4.8 on page 88, where we choose in particular the calculated missing mass. The tails of both distributions, after all the cuts, are calculated and the background contribution is found to be about 20% for both the η and the ω channels.

Chapter 5

Experimental results

Introduction

In this chapter we will present the measurement of the beam asymmetry for the following reactions:

$$\vec{\gamma} + p \quad \rightarrow \eta + p \quad \rightarrow \pi^+ + \pi^- + \pi^o + p \tag{5.1}$$

$$\vec{\gamma} + p \quad \rightarrow K^+ + \Lambda \quad \rightarrow K^+ + \pi^- + p \tag{5.2}$$

For the reaction 5.1, one goal is to compare the asymmetry values extracted from the η charged decay channel with the beam asymmetry already extracted at Graal from the η neutral decay, $\eta \rightarrow \gamma\gamma$. This will allow to check the validity and quality of the software of the track reconstruction of cylindrical MWPCs, reported in chapter 3.
The asymmetry of the $K^+\Lambda$ photoproduction is a new measurement. It contributes to the existing data base of the strangeness photoproduction, providing data for two different polarisation observables, which could help to emphasize the contribution of known and/or missing resonances and, in the latter case, eventually extract their characteristics (masses and widths). In the first chapter, we already discussed the most important theoretical models concerning this subject, and the role played by the polarisation observables, as the beam asymmetry $\mathbf{\Sigma}$, in the extraction of the baryonic resonances.
The first section of this chapter is dedicated to the beam asymmetry definition from an experimental point of view. Afterwards, in the second section, we will show the extraction method of this observable from the Graal data. In the third section the evolution of the asymmetry, as a function of the photon energy in the laboratory frame and of the meson

polar angle in the center of mass, is shown for the η photoproduction and compared to the beam asymmetry of the decay $\eta \to \gamma\gamma$ measured at Graal. In the fourth section the beam asymmetry is shown for $K^+\Lambda$ photoproduction. We will, hence, compare this beam asymmetry with a model from the isobar analysis [27, 28, 70].

5.1 Definition of the observable Σ

In the appendix A we defined the beam asymmetry as the averaged transformation of the photon spin operator in the Pauli-spinor space of the baryon. The experimental beam asymmetry $\mathbf{\Sigma}$ is derived from the polarised differential cross section:

$$\frac{d\sigma}{d\Omega}^{(\pm,0,0)} = \frac{d\sigma}{d\Omega}^{(0,0,0)} [1 + \mathbf{\Sigma} \cdot \mathbf{P}^S] \tag{5.3}$$

where $\pm$ superscript indicates the general choices for the photon polarisation; $(0,0,0)$ means the unpolarised differential cross section and $\mathbf{P}^s$ is the direction and degree of polarisation of the photon as determined by the experimental set-up. The Graal photon beam is linearly polarised with the particular choice $\mathbf{P}^S = \pm 1\hat{x}$. The two possible states $\phi = 0(\|)$ and $\phi = \pi/2(\perp)$ are eigenstates of the matrix $\mathbf{P}$ and, thus, the equation simplifies to:

$$\frac{d\sigma}{d\Omega}^{(\pm,0,0)} = \frac{d\sigma}{d\Omega}^{(0,0,0)} [1 \pm P\mathbf{\Sigma} \cos 2\phi]$$

where P is the experimental degree of the linear polarisation. If we measure the number of events selected for a given channel and for each polarisation state, $N_\|$ and $N_\perp$, with an efficiency ϵ and their relative fluxes, $\Phi_\|$ and $\Phi_\perp$, we obtain:

$$N_\|/\Phi_\| = \epsilon \frac{d\sigma}{d\Omega}^{(\|,0,0)} = \frac{d\sigma}{d\Omega}^{(0,0,0)} (1 - P\mathbf{\Sigma} \cos 2\phi)\epsilon \tag{5.4}$$

$$N_\perp/\Phi_\perp = \epsilon \frac{d\sigma}{d\Omega}^{(\perp,0,0)} = \frac{d\sigma}{d\Omega}^{(0,0,0)} (1 + P\mathbf{\Sigma} \cos 2\phi)\epsilon \tag{5.5}$$

If our detector was fully symmetric (in geometry and response) in the azimuthal angle ϕ, the efficiency ϵ would be a function of the polar angle of the meson in the c.m. system, θ_{cm}, and of the photon energy, E_γ. Equations (5.4) and (5.5) are calculated for fixed values of θ_{cm} and E_γ: in this case ϵ can be considered as a constant. A slight dependence of ϵ on the azimuthal angle can originate from small asymmetries in ϕ of the detector response, but, as this dependence is the same for both polarisation states, it is possible

to cancel this efficiency in the formulas that provide the experimental asymmetry $\mathbf{\Sigma}$. We can therefore add equations (5.4) and (5.5) to calculate the unpolarised cross section:

$$\frac{d\sigma}{d\Omega}^{(0,0,0)} = \frac{N_{\parallel}/\Phi_{\parallel} + N_{\perp}/\Phi_{\perp}}{2\epsilon} \tag{5.6}$$

The unpolarised cross section can thus be replaced in equations (5.4) and (5.5) to obtain two equations, where the only unknown is $P\mathbf{\Sigma}$:

$$\frac{N_{\parallel}/\Phi_{\parallel}}{N_{\perp}/\Phi_{\perp} + N_{\parallel}/\Phi_{\parallel}} = \frac{1}{2}\left(1 - P\mathbf{\Sigma}\cos 2\phi\right) \tag{5.7}$$

$$\frac{N_{\perp}/\Phi_{\perp}}{N_{\perp}/\Phi_{\perp} + N_{\parallel}/\Phi_{\parallel}} = \frac{1}{2}\left(1 + P\mathbf{\Sigma}\cos 2\phi\right) \tag{5.8}$$

A third equation can also be used to extract the beam asymmetry and it is obtained by the difference between (5.5) and (5.4) divided by (5.6):

$$\frac{N_{\perp}/\Phi_{\perp} - N_{\parallel}/\Phi_{\parallel}}{N_{\perp}/\Phi_{\perp} + N_{\parallel}/\Phi_{\parallel}} = P\mathbf{\Sigma}\cos 2\phi \tag{5.9}$$

Equations (5.7), (5.8) and (5.9) allow the extraction the beam asymmetry $P\mathbf{\Sigma}$ with the same procedure. We emphasize that ϵ disappeared from these equations, so that we do not have to know the detector efficiency to extract the beam asymmetry.
The number of events, $N_{\parallel}$ and $N_{\perp}$, are the result of the kinematic selections, reported in the previous chapter, while $\Phi_{\parallel}$ and $\Phi_{\perp}$ are the number of total incident photons, evaluated for the whole period of data acquisition, separately, for both polarisations, as explained in section 2.3.4 on page 27 and calculated in [51].

5.2 $\mathbf{\Sigma}$ extraction on data

The $\mathbf{\Sigma}$ value can be extracted by a simple fit $f = P_1 \cos 2\phi$ of the distribution (5.9), where $P_1 = P\mathbf{\Sigma}$. In order to extract the asymmetry (or other observables) from selected data, we have to divide the phase space into bins. Each bin size should be chosen in order to have enough statistics for each bin. The second requirement is that the bin of one variable must be larger than the resolution of the variable itself. We will, then, report in the following paragraphs the resolution of each kinematical variable, E_γ, θ_{cm} and ϕ_{cm} in order to establish, for each kinematical variable, the appropriate division. For each variable we have also to apply some corrections, deriving from different causes:

- some kinematical solutions can give, because of the resolution, a θ_{cm} greater than the maximum possible value defined by the kinematics;

- the fit of the asymmetry is accomplished on a finite number of points;

- the ϕ resolution alters the fit value if a low number of bins is chosen.

We will describe more precisely all these points in the following paragraphs.

E_γ resolution

The resolution on the energy of the incident photons has been extracted by the simulation and experimentally measured. Its value is $\mathcal{F}_{E_\gamma} = 16MeV$ (of the order of 1%). The energy resolution being good, the number of bins must be chosen in order to have enough statistic. Hence we have divided into seven bins in the range $0.5 - 1.5\ GeV$.

θ_{cm} correction and resolution

The polar angle of the meson η (or of the kaon for $K^+\Lambda$) in the center of mass is calculated from its momentum in the laboratory system:

$$\theta_{cm} = \arccos\left(\frac{p_{z\,cm}}{p_{cm}}\right) \tag{5.10}$$

where

$$\begin{aligned} p_{x_{cm}} &= p_x \\ p_{y_{cm}} &= p_y \\ p_{z_{cm}} &= \gamma(p_z - \beta E) \\ p_{cm} &= \sqrt{{p_{x_{cm}}}^2 + {p_{y_{cm}}}^2 + {p_{z_{cm}}}^2} \end{aligned}$$

and

$$\beta = \frac{p_{cm}}{E_{cm}} = \frac{E_\gamma}{E_\gamma + m_p}\ ; \qquad \gamma = 1/\sqrt{1-\beta^2}$$

The meson momentum $p = (p_x, p_y, p_z)$ is the solution of the two methods, explained in the analysis chapter. If we use the first method for the selection of the events the resolution on θ_{cm} of the η meson is mainly affected by the resolution of the π° angle, measured by the BGO. In order to improve this resolution we can reconstruct the θ_{cm} using θ_p measured by the MWPCs and E_γ. In figure 5.1 we show the difference between the θ_{cm} and the

true value θ_{cmtrue}, coming from the simulation: the empty and full histograms represent the resolution on the same sample of events before and after the new calculation of θ_{cm}, respectively, showing the improvement of the resolution.

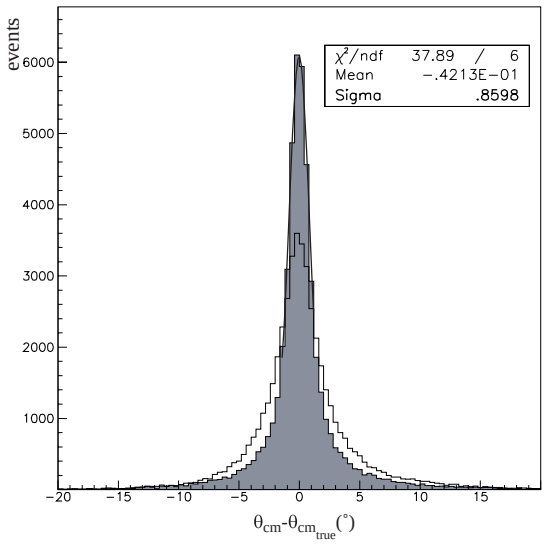

Figure 5.1: *Resolution of the meson θ_{cm} on simulated events from the η channel. The empty histogram is the resolution of the θ_{cm} calculated from the first analysis method (4.5). The full histogram represents the resolution of θ_{cm} on the same events, when it is reconstructed from the θ_p measured by the MWPCs.*

A minor correction must also be accomplished on those events whose angle θ_p (or θ_K for $K^+\Lambda$) measured by the MWPCs is greater than the maximum value $\theta_{p_{max}}$ allowed by the kinematics. This effect is due to the angular resolution of the MWPCs and is corrected by replacing the θ_p with $\theta_{p_{max}}$.
The average resolution, estimated after both the corrections, is $\mathcal{F}_{\theta_{cm}} \simeq 2.0°(FWHM)$. We have then decided to divide the polar angle into seven bins from 0° to 180°.

ϕ_{cm} correction and resolution

The direction of the photon beam is along the z axis, so that $\phi_{cm} = \phi_{lab}$. The resolution of the azimuthal angle of the meson has been experimentally measured and confirmed by the simulation. Its value is $\mathcal{F}_{\phi} \simeq 4.5°(FWHM)$. We have thus decided to divide the ϕ range in 16 bins, in order to have enough statistics for each bin.
The resolution of the azimuthal angle of the meson modifies the value of the asymmetry. The function $\cos 2\phi$ is in fact given by the integral weighed with the Gaussian distribution

of the resolution:

$$\cos 2\phi \rightarrow \cos 2\phi \int_{\phi'=-\pi}^{\pi} \cos 2\phi' \mathcal{G}(\phi') d\phi' \tag{5.11}$$

where $\mathcal{G}$ is a Gaussian function with $FWHM = \mathcal{F}_{\phi'}$. The correction factor to be applied to the beam asymmetry depends, therefore, on the azimuthal resolution itself and it has been estimated [51] to be ranging between 0.98 and 1.
The second systematic error is produced by the choice of the number of bins. In fact, by fitting the equations (5.9), with a function $\cos 2\phi$ on a finite number of bins the Σ value is overestimated. The correction factor to be applied with 16 bins, extracted from the simulation [51], is $\Sigma_c = 0.9745\Sigma$.

Polarisation extraction and Bremsstrahlung correction

We explain now how the polarisation P is calculated and the correction to be applied to subtract the Bremsstrahlung contribution.
The events, selected to extract the beam asymmetry, belong to different periods of the acquisition. Each period corresponds to different values of the laser emission lines (515, 351 and 330 nm). The value of the polarisation is calculated for each event, as shown in figure 2.3 on page 22, and is specific to the different laser lines.
The γ beam is partially unpolarised because there is always a component of Bremsstrahlung photons produced by the electrons in the storage ring. The physical events produced by a Bremsstrahlung photon can be confused with a true event if it is in coincidence with the experimental trigger. As the polarisation of these photons is 0 they will produce on average an underestimation of the asymmetry. This systematic error is estimated with the acquisition of data with the laser off. A standard acquisition run is composed by cycles of about 20 minutes for each polarisation state and about 5 minutes of acquisition with the laser off (Bremsstrahlung mode). In the Bremsstrahlung mode the events satisfying all the kinematical cuts are therefore selected. The Bremsstrahlung flux is integrated over all the periods and its contribution, B, to both polarised Compton fluxes ($N_{\gamma_\perp}$ and $N_{\gamma_\parallel}$) is then calculated. The corrected polarisation for each energy bin, $\overline{P}_c(E_\gamma)$, is therefore given by:

$$\overline{P}_c(E_\gamma) = a\overline{P}(E_\gamma)\left(1 - \frac{B}{N_{\gamma_\parallel} + N_{\gamma_\perp}}\right)$$

where $\overline{P}(E_\gamma)$ is the calculated one. The factor $a = 0.98$ takes into account the polarisation loss along the beam optics (in particular the Beryllium mirror). The polarisation loss has been measured with a polarimeter at the exit of the laser cavity (where $P = 1$) and after all the optics (where we found $P = 0.98 \pm 0.01$).

Fit and normalization

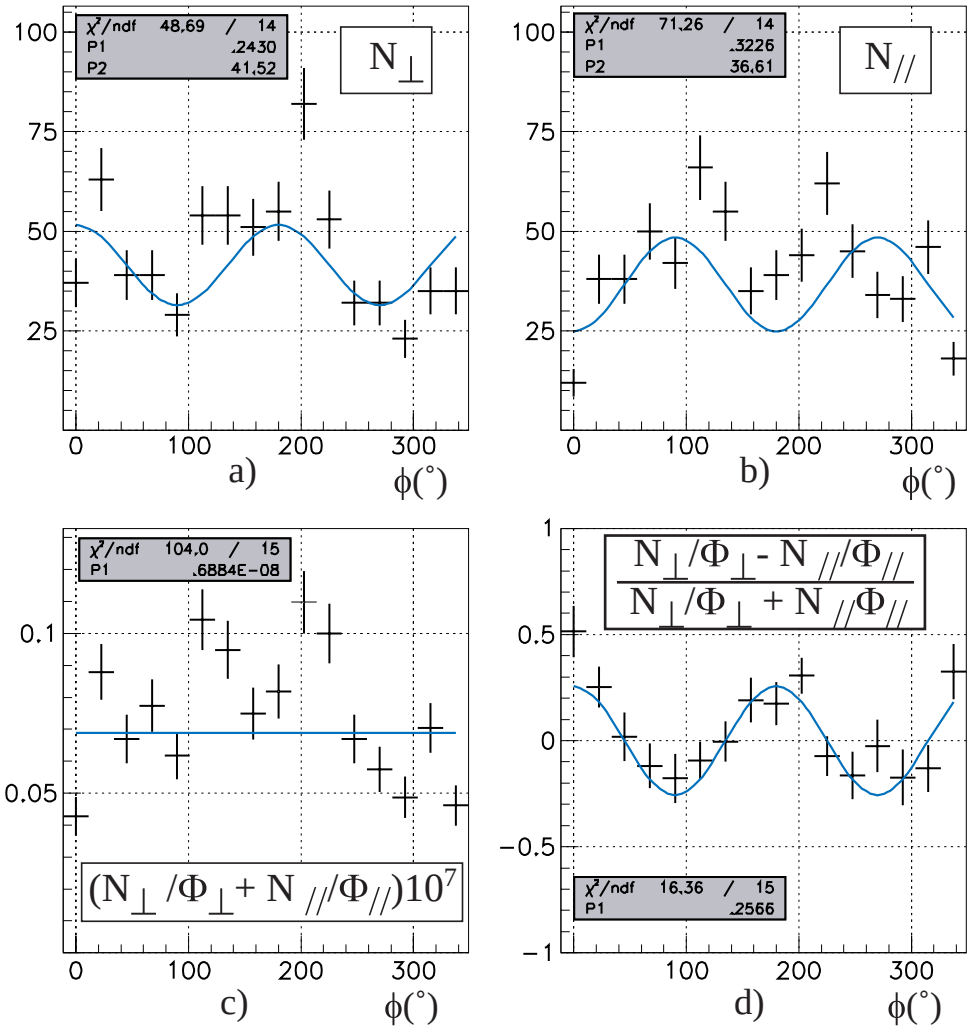

Figure 5.2: *Asymmetry extraction on preselected data from the η decay 5.1. a) and b): the distribution of the events from the two polarisation states, normalized to their respective fluxes. c): the unpolarised cross section (times 2ϵ); d): fit of the distribution of equation 5.9 where $P_1 = \Sigma P$ gives the beam asymmetry.*

In figure (5.2) we show the fit procedure for a given bin (E_γ, θ) in the η channel. As explained in the first section, we directly measure the two polarised differential cross sections of equations (5.4) and (5.5) (a and b in the figure) and we add them together to obtain the unpolarised cross section of equation (5.6) (c). The obtained values are used to calculate equation (5.9)(d). The fit with the function $f = P_1 \cos 2\phi$ gives the value $P_1 = P\mathbf{\Sigma}$, from which we can extract the $\mathbf{\Sigma}$ value for the bin.
The background, which is present in the selected events, can alter the asymmetry values. The background can be of hadronic or electromagnetic origin or it can be produced by materials other than the target. If it has not a particular asymmetry, it will introduce a systematic shift of the asymmetry towards to zero, because we overestimate the unpolarised cross section. The estimation of the background has been accomplished from the data and in principle we cannot say anything on its asymmetry. The main channel in the background contribution to the η and ω channels, as estimated from the simulation, is the direct photoproduction of $\pi^+\pi^-\pi^\circ$. This reaction has a threshold lower then both the reactions but, in principle, it should not have resonant contributions, that could modify the asymmetry. Notwithstanding its cross section is expected to increase with the energy of the photon and this, as we will discuss later in this Chapter.

5.3 Asymmetry of the η photoproduction

The extraction of the asymmetry was performed on selected data for the decay channel (5.1) of the η meson. The period of data taking started in April 1998, when the cylindrical MWPCs were installed, up to the millennium end. We have 1475 runs: 322 of them have been acquired by using the green line of the laser at 514 nm, 1153 by using the UV line at 351 nm. The total number of events selected with the first method is 51279 and 26088 with the second one, whose efficiency is lower as explained at the end of chapter 4.
We do not report the asymmetry for the second analysis method with one photon from the π° decay, as its background is too high, producing, in this way, an asymmetry value systematically shifted towards zero.
As previously said, we divided the meson azimuthal angle in 16 bins, the meson polar angle in the center of mass system in 7 bins and the photon energy in the laboratory system in 13 bins. Let us compare, at first, in figure (5.3) the asymmetry calculated with the two different analysis methods. The first and second method are in perfect agreement. We pointed out in Section 4.7 that the efficiency of the events selected with the first method is higher than the efficiency of the second one. For this reason we decide to

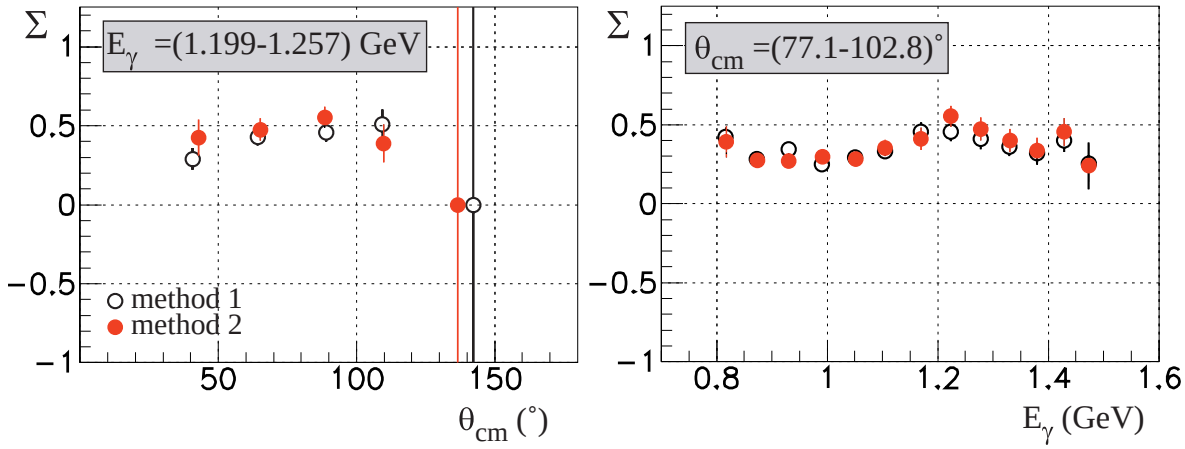

Figure 5.3: *Comparison of the asymmetry extracted from the two different methods used on selected data for the η decay. For each method we show the asymmetry, as given by equation (5.9). We chose one bin in θ_{cm} and one in E_γ.*

use the beam asymmetry calculated from the first method, for the comparison with the asymmetry extracted from the neutral decay $\eta \rightarrow 2\gamma$.

The result is shown for four energy bins in figure 5.4. The agreement between the two η decays seems to be good but for the last two bins a difference at the lowest θ_{cm} is observed. This effect is due to the increasing background for higher photon energies, as we can observe by plotting the missing mass as a function of the photon energy itself. The increasing background produces, as explained above, an underestimation of the beam asymmetry. This effect can be further illustrated by the behaviour of the asymmetry as a function of the photon energy, as shown in figure 5.5.

We can then conclude that in the kinematical region where the background is lower (that is up to 1 GeV, where the background is lower that 20%) the analysis methods give a beam asymmetry for the η charged decay in agreement with the neutral one. This result confirms that the method of the track reconstruction in the cylindrical MWPCs has been properly defined and that we can use them to select channel with lower cross section (as the $K^+\Lambda$ in the following section).

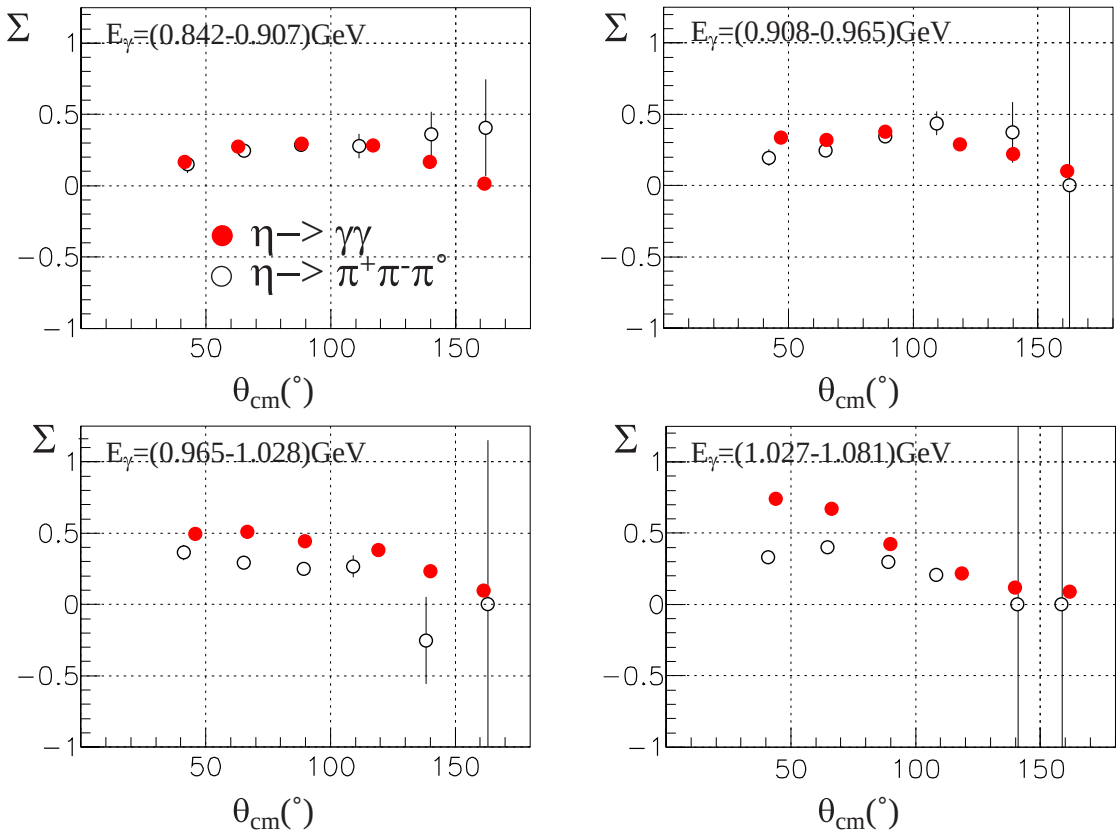

Figure 5.4: *Beam asymmetry* $\boldsymbol{\Sigma}$ *for the channels* $\eta \to \pi^+\pi^-\pi^\circ$ *(in black) and* $\eta \to 2\gamma$ *(light-coloured), as a function of the polar angle of the meson in the centre of mass system.*

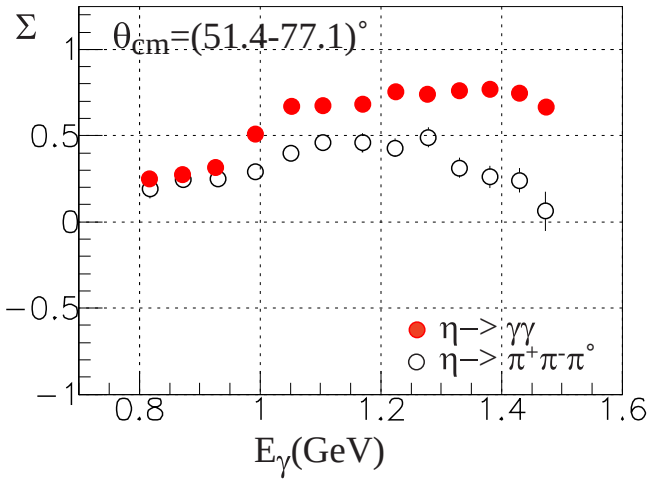

Figure 5.5: *Beam asymmetry* $\boldsymbol{\Sigma}$ *for the channels* $\eta \to \pi^+\pi^-\pi^\circ$ *(in black) and* $\eta \to 2\gamma$ *(light-coloured), as a function of the photon energy.*

5.4 Asymmetry of the KΛ photoproduction

In this section we will show the results obtained for the asymmetry of the channel (5.2). No previous results existed for the $K^+\Lambda$ photoproduction beam asymmetry.
We divided the kaon azimuthal angle in 16 bins, the kaon polar angle in the c.m. system in 7 bins and the photon energy in the laboratory system in three bins. Figure 5.6 shows the comparison between the asymmetry values extracted from the two different analysis methods. As we can see the agreement is excellent.

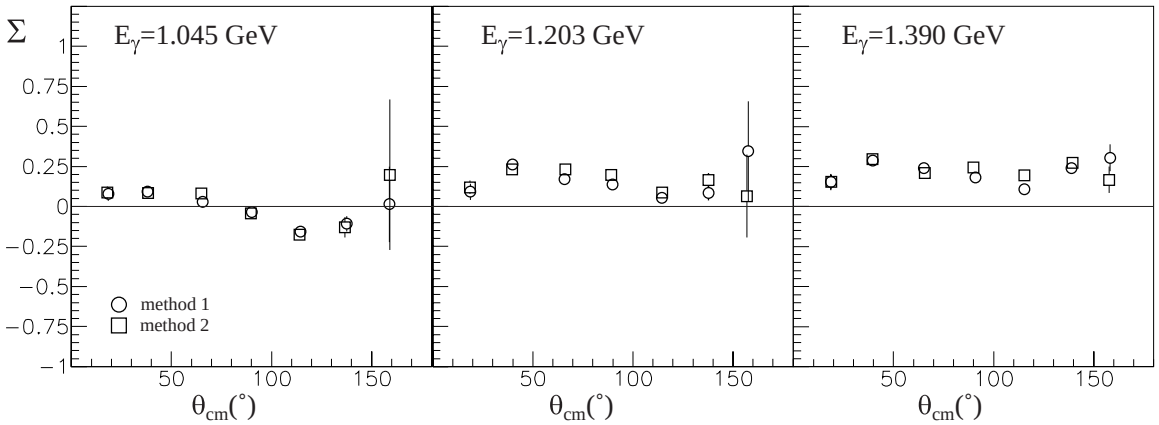

Figure 5.6: *Beam asymmetry* $\mathbf{\Sigma}$ *for the* $K^+\Lambda$ *photoproduction as a function of the polar angle of the kaon,* θ_{cm}*, and for both analysis methods [69].*

The asymmetry is in general smaller than 25%. In the first energy bin it is positive for angles smaller than 90°, it crosses 0 for this value and it becomes negative for the backward angles. In the other two bins the asymmetry is always positive.
In figure (5.7) the two curves show the results from the isobar models SL[27] and C[28] (see Section 1.4), based on experimental data from the Graal beam asymmetry (present results) and old data of Λ recoil polarisation asymmetry. As we explained in the first Chapter, the SL model included all the nucleonic resonances with spin 3/2 and 5/2 to the previous model [26]; only a combination of few of them gave a χ^2_{red} reasonable with the coupling constants compatible with the SU(3) requirements. The C model is an implementation of the SL one: the off-shell treatement have been applied to all the hyperonic and nucleonic resonances with spin= 1/2. The resonances resulting from these two models are listed in table 5.1 (a part from the t-channel given by $K^*(892)$ and $K1(1270)$).
The curves from both models are compared with the Graal beam asymmetry data, which clearly select the SL model. This model includes more nucleonic resonances than the C model and gives to the curve a more pronounced nodal structure [71].

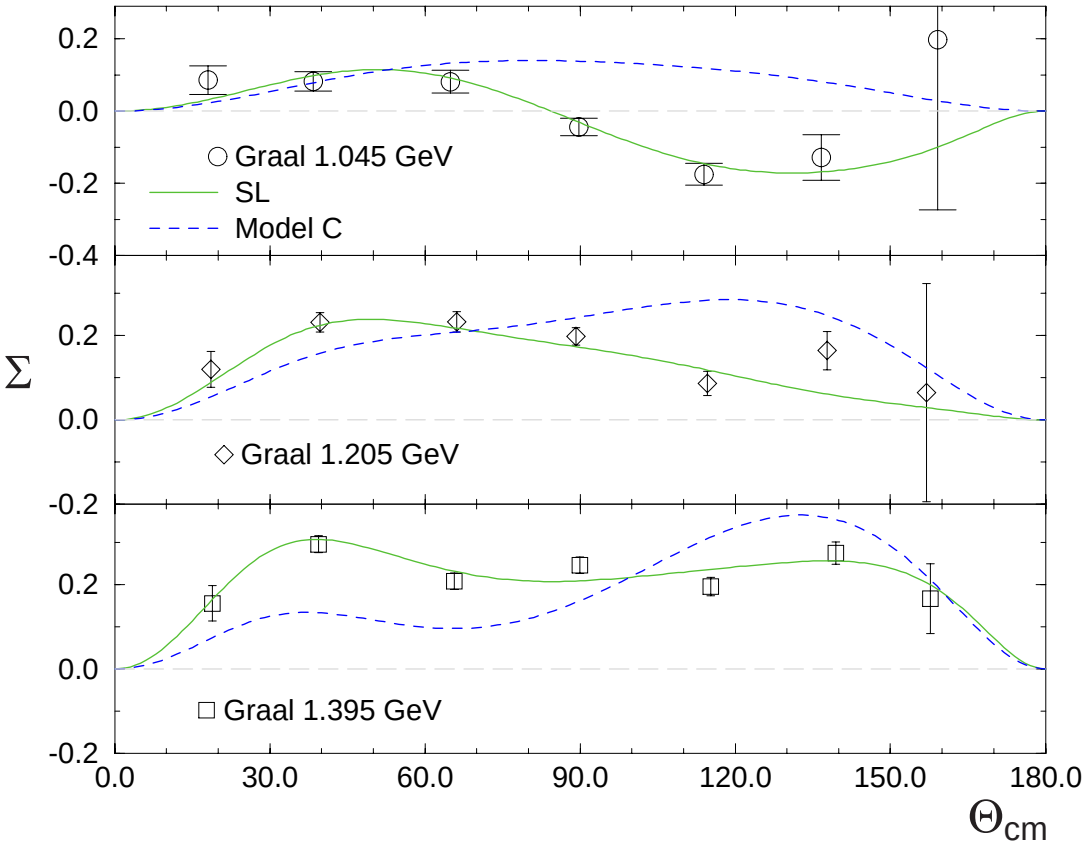

Figure 5.7: *The beam asymmetry* $\mathbf{\Sigma}$ *for the* $K^+\Lambda$ *photoproduction as a function of the polar angle of the kaon,* θ_{cm}*, measured at Graal is compared with two curves from models SL and C.*

In figure 5.8 are shown the results from the same models for the recoil polarisation asymmetry compared to the old experimental data. The recoil polarisation observable seems to be less selective on these models than the beam polarisation asymmetry. This result urges us to take new data in order to increase the statistics. A greater number of smaller bins in the photon energy and in the θ_{cm} of the meson in the c.m. system could further emphasize and claim the contribution of these resonances. Moreover the measurement of the recoil polarisation and of the double polarisation observables recoil-photon, O_x and O_z, foreseen in the Graal program could improve the quality of the present database and give some more information on these last obsevables.

SL				
s	$N[1(1/2^+)](1440)$	$N[1(3/2^+)](1720)$	$N[2(5/2^-)](1675)$	
u	$\Lambda[0(1/2^-)](1405)$	$\Lambda[0(1/2^-)](1670)$	$\Lambda[1(1/2^+)](1810)$	
u	$\Sigma[1(1/2^+)](1660)$			
C				
s		$N[1(3/2^+)](1720)$		
u	$\Lambda[0(1/2^-)](1405)$	$\Lambda[0(1/2^-)](1670)$	$\Lambda[1(1/2^+)](1810)$	$\Lambda[1(3/2^+)](1890)$
u	$\Sigma[1(1/2^+)](1660)$			

Table 5.1: *Resonance contribution in the s and u channel for the two models SL[27] and C[28].*

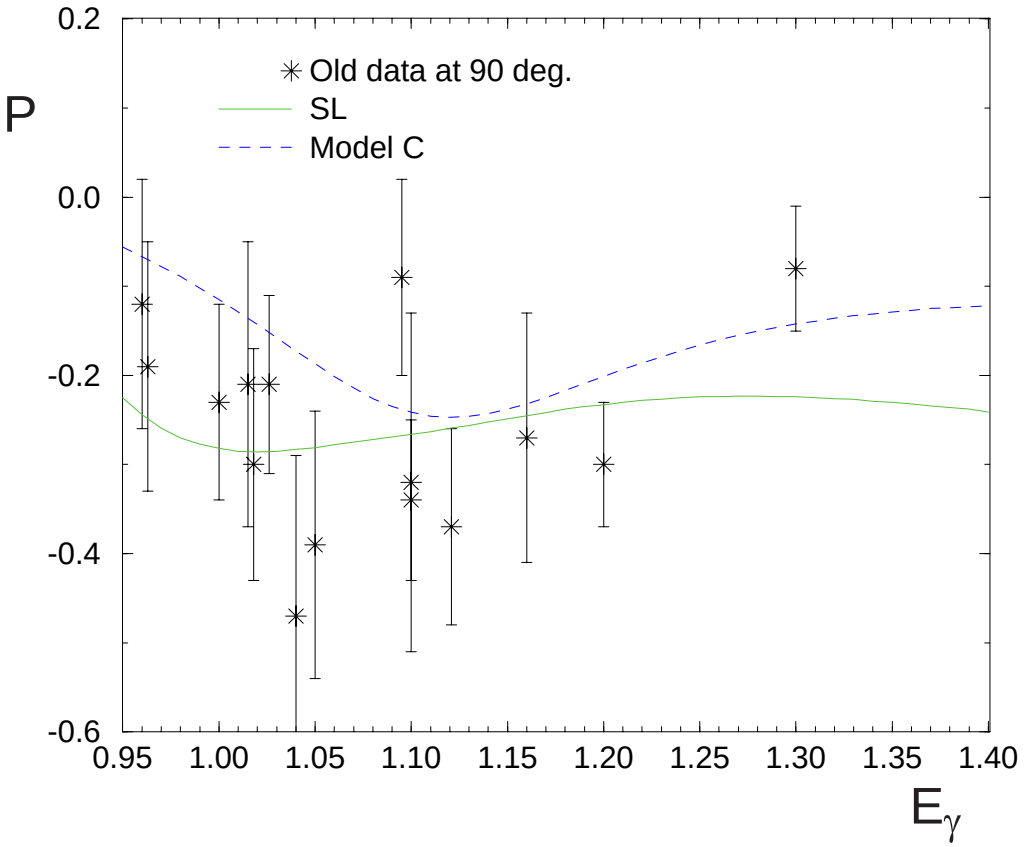

Figure 5.8: Λ *recoil polarisation asymmetry* $\boldsymbol{P}$ *for the* $K^+\Lambda$ *photoproduction as a function of the photon energy* E_γ*: the points are the results from old experimental data, the two curves show the results from the SL and C models.*

Conclusion

Dans cette thèse nous avons étudié et amelioré les méthodes de reconstruction de traces d'un détecteur constitué de deux MWPC cylindriques. Le but était d'utiliser ce détecteur pour l'analyse de canaux à trois particules chargées.

La méthode de reconstruction des traces, l'étude de la résolution spatiale et de l'efficacité associées à ce détecteur ont été décrites dans le chapitre 3.

Nous avons d'abord étudié la réponse du détecteur dans le cas d'une seule trace et nous avons montré que l'efficacité de reconstruction est d'environ 90%, en accord avec la simulation. La résolution azimuthale des données est bien reproduite par la simulation mais celle de la coordonnée z reste sous-estimée. Nous avons observé que cet effet est dû à une simulation trop simpliste de l'avalanche des électrons. Nous avons donc cherché à reproduire de façon la plus réaliste possible ce phénomène. La nouvelle simulation conduit maintenant à une résolution spatiale très voisine de la résolution expérimentale.

Nous avons ensuite étudié, à l'aide de la simulation, la reconstruction de plusieurs traces dans les chambres cylindriques. Nous avons noté une baisse importante de l'efficacité globale de reconstruction des événements à deux ou trois traces. Une méthode de traitement du recouvrement des clusters sur les cathodes a été développée. Cette amélioration permet d'augmenter d'un facteur deux l'efficacité de reconstruction des traces pour les événements à trois particules chargées.

A la fin du Chapitre 3 nous avons étudié la reconstruction du vertex de production des particules. En particulier, nous avons montré qu'il est possible de vérifier la durée de vie du Λ par la mesure de la distance entre la position des vertex primaire et secondaire. Nous pouvons donc conclure que les performances et la méthode d'analyse des chambres cylindriques permettent d'améliorer la sélection des canaux avec trois particules chargées.

Deux méthodes d'analyse, présentées dans le Chapitre 4, ont été developpées pour l'analyse des canaux à trois particules chargées. L'efficacité d'analyse et la sélectivité de ces deux méthodes ont été présentées afin de tester laquelle de ces deux méthodes donne l'efficacité la meilleure avec un bruit de fond limité. Nous avons aussi developpé une méthode permettant d'identifier le π^0 à partir des événements avec un seul cluster neutre dans le calorimètre. Nous avons montré que ces événements peuvent être récuperés dans

le cas du canal $\omega \rightarrow \pi^+\pi^-\pi^o$.

Pour tester les méthodes d'analyse des canaux à trois particules chargées et de reconstruction des chambres cylindriques, nous avons étudié en particulier les décroissances chargées $\eta \rightarrow \pi^+\pi^-\pi^o$ et $\omega \rightarrow \pi^+\pi^-\pi^o$, l'asymétrie faisceau Σ mesurée à partir de ces canaux pouvant être comparées avec celles obtenues pour les décroissances neutres $\eta \rightarrow \gamma\gamma$ et $\omega \rightarrow \pi^\circ\gamma$. Les asymétries du η sont comparées dans le chapitre 5; nous avons observé un bon accord entre les deux dans le domaine d'énergie où le bruit de fond reste peu élevé dans le cas de la décroissance chargée ($E_\gamma \leq 1\ GeV$). Cependant, la très faible efficacité empêche une exploitation physique des données en dessous de 1 GeV.

Nous avons mis à profit ces résultats pour l'analyse du canal $K\Lambda$ pour lequel l'analyse repose entièrement sur l'utilisation des chambres cylindriques. Malgré la difficulté d'extraction de ce canal, nous avons obtenu une efficacité raisonnable (10%) pour un bruit de fond limité à 10%. Nous avons ainsi présenté dans le Chapitre 5 la mesure de l'asymétrie faisceau pour ce canal et nous avons comparé ces données à un modèle isobarique récemment developpé par la collaboration Saclay-Lyon. Ce modèle a mis en évidence que l'asymétrie faisceau est très sélective sur les différentes hypothèses du modèle et favorise la contribution des résonances nucléoniques par rapport aux résonances hypéroniques.

Dans le cadre du travail effectué au cours de cette thèse nous pouvons donc conclure que le détecteur de trace fournit de bonnes performances pour la reconstruction des canaux à trois particules chargées. La nouvelle simulation des chambres cylindriques reproduit désormais la résolution spatiale expérimentale et peut être incorporée dans la nouvelle chaîne d'analyse.

Lors des prochaines prises de données il est prévu de complèter la statistique des événements $K\Lambda$ pour l'extraction des observables Σ, P, O_x, O_z. Nous pourrons donc calculer ces observables avec des pas en énergie et en angle plus petits, en imposant ainsi plus de contraintes sur les modèles théoriques.

Les méthodes d'analyse développées au cours de cette thèse pourront aussi être utilisées pour la reconstruction du canal de photoproduction de l'hyperon Σ, dont l'état final présente trois particules chargées et un photon. Ce canal permettra de pouvoir accéder aux résonances Δ^*, le Σ étant un baryon d'isospin 3/2.

Enfin, l'étude de la photoproduction du méson vecteur ω est prometteuse. La prochaine étape dans le cadre du projet Graal sera d'étudier les méthodes d'extraction des observables (en particulier les observables de double polarisation) dans la photoproduction des mésons vecteurs.

Appendix A

Photoproduction polarization observables

Let us consider the reaction $\gamma + N \rightarrow M + B$, where N is the neutron or the proton, M is a pseudoscalar (spin 0) meson (π, K, η) and B is a baryon with spin 1/2 (proton, Λ, Σ). The coordinate system is defined in figure A.1. The photon polarization vector is $\epsilon_\lambda(k)$, where k is the photon momentum and λ is its helicity. The quantization axis is z, corresponding to the beam direction. The projection of the spin of the nucleon and of the baryon are respectively m_s and $m_{s'}$. Hence, the interaction matrix is:

$$\langle \mathbf{q}, m_{s'} \mid T \mid \mathbf{k}, m_s, \lambda \rangle = \langle m_{s'} \mid F_\lambda \mid m_s \rangle \tag{A.1}$$

where the scattering amplitude F_λ is a rank one spherical tensor operator $F_\lambda = \mathbf{J} \cdot \hat{\epsilon}_\lambda(\mathbf{k}) = J_{1\lambda}$ in the Pauli-spinor space of the nucleon and the baryon. The current $\mathbf{J}$ can be expressed in term of four CGLN ([13]) amplitudes f_1, f_2, f_3 and f_4:

$$\mathbf{J} = i f_1 \boldsymbol{\sigma} + f_2 \frac{(\boldsymbol{\sigma} \cdot \mathbf{q})(\boldsymbol{\sigma} \times \mathbf{k})}{qk} + i f_3 \frac{\boldsymbol{\sigma} \cdot \mathbf{k}}{qk} \cdot \mathbf{q} + f_4 \frac{\boldsymbol{\sigma} \cdot \mathbf{q}}{q^2} \cdot \mathbf{q} \tag{A.2}$$

These functions have been calculated by [13] in order to satisfy the following requirements:
-the matrix elements must be function of Lorentz invariants;
-the matrix elements must be linear and homogeneous in ϵ;
-gauge invariance;
-if the meson is pseudoscalar the factor γ_5 must be included;
-the independent possible combinations of the isotopic spins must be either Hermitian of anti-Hermitian;
-crossing symmetry (exchange between the incoming nucleon and the outcoming baryon);

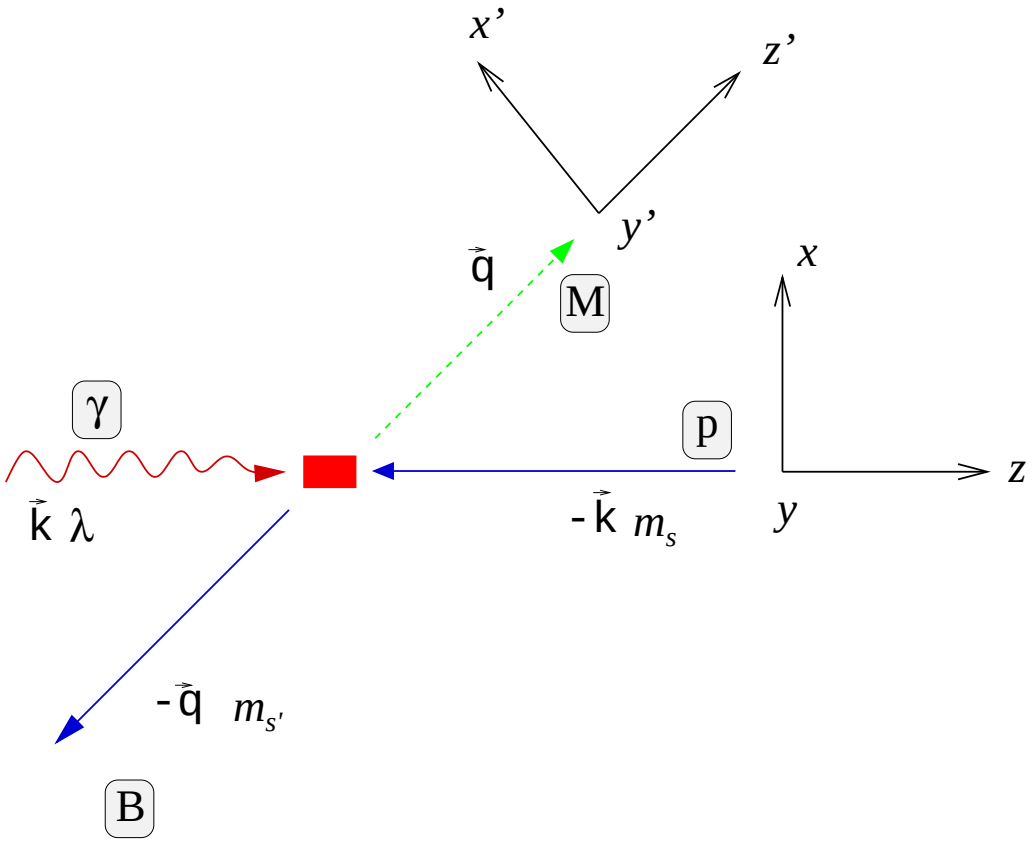

Figure A.1: *Definition of the kinematic variables for the photoproduction of pseudoscalar mesons [14].*

-unitary, that relates the phase of an outgoing state of defined momentum, isotopic spin and parity to the phase of the corresponding scattering amplitude.

The number of degrees of freedom is eight because we have two polarization states for the photon ($\lambda = \pm 1$), two initial states of the target spin and two final spin state of the recoil baryon. Only four of them are independent if we apply the rotational and parity invariance. These four amplitudes are complex so that we have to measure eight real numbers. It has been shown by [72] that, in addition to the measurement of differential cross section and single polarization observables (beam, target and recoil asymmetries, which we will define later on and which we call respectively PB, PT and PR), three double polarization observables are needed in order to completely measure all these amplitudes. The possible classes are: polarized beam-polarized target(PB-PT), polarized beam-recoil polarization (PB-PR) and polarized target-recoil polarization (PT-PR). All of these double polarization measurements cannot come from the same class.

By using the coordinate system of figure A.1 the current $\mathbf{J}$ simplifies to the form:

$$\begin{aligned} J_x &= A\sigma_x + B\sigma_z \\ J_y &= C + D\sigma_y \\ J_z &= 0 \end{aligned}$$

where

$$\begin{aligned} A &= i(f_1 - f_2\ cos\theta + f_4\ sin^2\theta) \\ B &= i\ sin\theta(f_2 + f_3 + f_4\ cos\theta) \\ C &= -f_2\ sin\theta \\ D &= i(f_1 - f_2\ cos\theta) \end{aligned}$$

The functions f_1, f_2, f_3, f_4 are the CGLN[1] amplitudes defined by [13]. So the scattering amplitude is:

$$\begin{aligned} F_\lambda = \mathbf{J}\cdot\boldsymbol{\epsilon}_\lambda = &= i\ f_1\boldsymbol{\sigma}\cdot\hat{\boldsymbol{\epsilon}}_\lambda + f_2(\boldsymbol{\sigma}\cdot\hat{\mathbf{q}})\ \boldsymbol{\sigma}\cdot(\hat{\mathbf{k}}\times\hat{\boldsymbol{\epsilon}}_\lambda) \\ &+ i\ f_3(\boldsymbol{\sigma}\cdot\hat{\mathbf{k}})(\hat{\mathbf{q}}\cdot\hat{\boldsymbol{\epsilon}}_\lambda) + i\ f_4(\boldsymbol{\sigma}\cdot\hat{\mathbf{q}})(\hat{\mathbf{q}}\cdot\hat{\boldsymbol{\epsilon}}_\lambda) \end{aligned} \tag{A.3}$$

In the density matrix approach one can demonstrate (see [14]) that the differential cross section can be written as:

$$\frac{d\sigma}{d\Omega} = \rho_0 \sum_{\alpha\lambda m_s'} P_\lambda P_\alpha |\langle m_s'|F_\lambda|\alpha\rangle|^2 = \rho_0 \frac{Tr(\rho_F)}{Tr(\rho_I)} \tag{A.4}$$

where $\rho_I \equiv \rho_N\rho_\gamma$ is the initial state density matrix, $\rho_F \equiv F\rho_I F^\dagger$ is the final one and $\rho_0 = q/k$ is the phase space. The trace is effectuated over the photon helicity and the initial and final baryon spin projections. The density matrix of the nucleon and the photon are defined on a complete set of eigenstates, each of them with a different probability:

$$\rho_N \equiv \sum_\alpha |\alpha\rangle P_\alpha \langle\alpha| \qquad and \qquad \rho_\gamma \equiv \sum_\lambda |\lambda\rangle P_\lambda \langle\lambda| \tag{A.5}$$

This simple expression can now be used to extract the polarization observables. We will report only the formalism for the PB (polarized beam) and PB-PR (polarized beam-polarized recoil), which can be measured by GRAAL (the polarized target will be installed in 2002). Let us recall that the photon density matrix can be expressed as:

$$\rho_\gamma = \frac{1}{2}[1 + \mathbf{P}^s\cdot\boldsymbol{\sigma}^\gamma]$$

[1] Chew Goldberger Low Nambu

where $\mathbf{P}^s$ is the Stokes vector, which gives the direction and degree of polarization of the photon beam, as measured by the experimental set-up. In this case and with the coordinate system of figure A.1 the cross section is:

$$\frac{d\sigma}{d\Omega}^{(\pm,0,0)} = \frac{\rho_0}{4} Tr(F[1 + \mathbf{P} \cdot \boldsymbol{\sigma}^\gamma]F^\dagger) = \frac{d\sigma}{d\Omega}^{(0,0,0)} [1 + \boldsymbol{\Sigma} \cdot \mathbf{P}^s] \tag{A.6}$$

where we have defined the beam asymmetry as:

$$\boldsymbol{\Sigma} \equiv \frac{Tr(F\boldsymbol{\sigma}^\gamma F^\dagger)}{Tr(FF^\dagger)}$$

The $\pm$ symbol is the beam polarization. For example, if we choose a linear polarized beam in the direction $\theta = 0(\|)$ and $\theta = \pi/2(\perp)$:

$$\boldsymbol{\Sigma} = \Sigma_x = \frac{\sigma^{(\perp,0,0)} - \sigma^{(\|,0,0)}}{\sigma^{(\perp,0,0)} + \sigma^{(\|,0,0)}} \tag{A.7}$$

In the same way we can define the other two single polarization observables, the recoil polarization asymmetry $\mathbf{P}$ and the polarized target asymmetry $\mathbf{T}$:

$$\mathbf{P} = \frac{\sigma^{(0,0,+y')} - \sigma^{(0,0,-y')}}{\sigma^{(0,0,+y')} + \sigma^{(0,0,-y')}} = \frac{Tr(\boldsymbol{\sigma}_y^b F F^\dagger)}{Tr(FF^\dagger)} \tag{A.8}$$

$$\mathbf{T} = \frac{\sigma^{(0,+y,0)} - \sigma^{(0,-y,0)}}{\sigma^{(0,+y,0)} + \sigma^{(0,-y,0)}} = \frac{Tr(F\boldsymbol{\sigma}_y^n F^\dagger)}{Tr(FF^\dagger)} \tag{A.9}$$

where b means the baryon and n the nucleon.

We have so defined three single polarization observables. The extraction of the four PB-PT$(\pm,\pm,0)$, four PB-PR$(\pm,0,\pm)$ and four PT-PR$(0,\pm,\pm)$ is also possible. Together with the unpolarized cross section we have, thus, the sixteen observables which are required to resolve the scattering matrix. As we said, the GRAAL experiment can measure the PB-PR observables via the $\gamma + p \to \Lambda + K^+$ reaction, because the Λ polarization is determined from the distribution of its decay products. The differential cross section for the four different polarization (two for the recoil baryon and two for the photon) is:

$$\frac{d\sigma}{d\Omega}^{(\pm,0,\pm)} = \frac{d\sigma}{d\Omega}^{(0,0,0)} [1 + \boldsymbol{\Sigma} \cdot \mathbf{P}^s + \mathbf{P} \cdot \mathbf{P}^b + P_i^b P_j^S C_{ij}^{BR}] \tag{A.10}$$

where

$$C_{ij}^{BR} \equiv \frac{Tr(\sigma_i^b F \boldsymbol{\sigma}_j^\gamma F^\dagger)}{Tr(FF^\dagger)}$$

and $\mathbf{P}^b$ are the Stokes parameters which give the baryon polarization.

There are different possibilities to express these observables:

- the amplitudes can be written for $J = 1/2$ and $J \leq 3/2$ to study the node structure and to establish some rules to define their presence;

- a multipolar expansion and a scattering length approximation allow to study the evolution of the nodes in function of the momentum;

- one can study the effect of one or more amplitudes dominating or resonating.

As example we report [73] the multipolar expansion for the observable $\mathbf{\Sigma}$ with $L \leq 2$:

$$\begin{aligned}
\hat{\mathbf{\Sigma}} &= \mathbf{\Sigma} I = -\frac{sin^2\theta}{2} Re\{|f_3|^2 + |f_4|^2 + 2|f_1^* f_4 + f_2^* f_3 + x f_3^* f_4|\} \\
&= Re\{\sum_{m=0}^{3} a_m x^m\}
\end{aligned}$$

with $x \equiv \cos(\theta_{cm}^{meson})$ and:

$$\begin{aligned}
a_0 &= [\,9\,|E_1^+|^2 - 3\,|M_1^+|^2 + 3\,|E_2^-|^2 - 9\,|M_2^-|^2 + 18\,|E_2^+|^2 - 9\,|M_2^+|^2 \\
&\quad -6\,E_0^+[E_2^- + M_2^- + E_2^+ - M_2^+]^* + 6\,M_1^-[E_1^+ - M_1^+]^* - 6E_1^+\,M_1^{+*} \\
&\quad +E_2^-[21\,E_2^+ + 6\,M_2^+]^* + 9\,M_2^-[E_2^+ + 2\,M_2^+]^* - 6\,E_2^-\,M_2^{-*} - 9\,E_2^+ M_2^{+*}\,] \\
a_1 &= 3\,[\,10\,M_1^-[E_2^+ - M_2^+]^* + 6\,E_1^+[-2\,E_2^- + 3\,E_2^+]^* \\
&\quad +M_1^+[-12\,M_2^{-*} - 10\,E_2^+ - 8\,M_2^+]^*\,] \\
a_2 &= 45\,[\,+2\,|E_2^+|^2 - |M_2^+|^2 - 3\,E_2^-\,E_2^{+*} + M_2^-[E_2^+ - 4\,M_2^{+*}]^* - E_2^+ M_2^{+*}\,]
\end{aligned} \tag{A.11}$$

The formalism developed in this section shows how a complete set of data can be obtained in order to give enough informations to determine the amplitudes expected by different theoretical formalism. That has not been possible up to now because of lack of high polarized photons beams with high emittance. It has, thus, been necessary to introduce some theoretical constraints in order to reduce the number of parameters.

Appendix B

Reactions included in the event generator

Number	Reaction
1	$\gamma + p \rightarrow \pi^+ + n$
2	$\gamma + p \rightarrow \pi^0 + p$
3	$\gamma + n \rightarrow \pi^- + p$
4	$\gamma + n \rightarrow \pi^0 + n$
5	$\gamma + p \rightarrow \Delta^{++} + \pi^-$
6	$\gamma + p \rightarrow \Delta^+ + \pi^0$
7	$\gamma + p \rightarrow \Delta^0 + \pi^+$
8	$\gamma + n \rightarrow \Delta^+ + \pi^-$
9	$\gamma + n \rightarrow \Delta^0 + \pi^0$
10	$\gamma + n \rightarrow \Delta^- + \pi^+$
11	$\gamma + p \rightarrow \rho^0 + p$
12	$\gamma + p \rightarrow \rho^+ + n$
13	$\gamma + n \rightarrow \rho^- + p$
14	$\gamma + n \rightarrow \rho^0 + n$
15	$\gamma + p \rightarrow \pi^+ + \pi^- + p$
16	$\gamma + p \rightarrow \pi^0 + \pi^+ + n$

Number	Reaction
17	$\gamma + n \rightarrow \pi^+ + \pi^- + n$
18	$\gamma + n \rightarrow \pi^0 + \pi^- + p$
19	$\gamma + p \rightarrow \eta + p$
20	$\gamma + n \rightarrow \eta + n$
21	$\gamma + p \rightarrow \omega + p$
22	$\gamma + n \rightarrow \omega + n$
23	$\gamma + p \rightarrow \pi^+ + \pi^0 + \pi^- + p$
24	$\gamma + p \rightarrow \pi^+ + \pi^+ + \pi^- + n$
25	$\gamma + n \rightarrow \pi^+ + \pi^0 + \pi^- + n$
26	$\gamma + n \rightarrow \pi^+ + \pi^- + \pi^- + p$
27	$\gamma + p \rightarrow \pi^+ + \pi^+ + \pi^- + \pi^- + p$
28	$\gamma + n \rightarrow \pi^+ + \pi^+ + \pi^- + \pi^- + n$
29	$\gamma + p \rightarrow \Lambda + K^+$
30	$\gamma + p \rightarrow \Sigma^0 + K^+$
31	$\gamma + p \rightarrow \Lambda + K^0 + \pi^+$
32	$\gamma + p \rightarrow \gamma + p$
33	$\gamma + p \rightarrow \eta' + p$
34	$\gamma + p \rightarrow \pi^+ + \gamma + n$
35	$\gamma + p \rightarrow \pi^0 + \pi^0 + p$
36	$\gamma + p \rightarrow \phi^0 + p$
37	$\gamma + p \rightarrow K^+ + K^- + p$
51	$\gamma + d \rightarrow \pi^0 + d$
52	$\gamma + d \rightarrow p + n$
55	$\gamma + {}^3\mathrm{He} \rightarrow \Delta^{++} + n + n$
56	$\gamma + {}^3\mathrm{He} \rightarrow \pi^0 + d + p$
57	$\gamma + {}^3\mathrm{He} \rightarrow \pi^+ + \pi^- + d + p$
58	$\gamma + {}^3\mathrm{He} \rightarrow \pi^- + \mathrm{dibaryon} + p$

Table B.1: *Reaction included in the event generator*

Appendix C

Summary of all the variables used by the simulation

Laggen variables	**Internal chamber**		**External chamber**	
	Cathode 1	Cathode 2	Cathode 1	Cathode 2
cartesian coordinates (cm)	xci(3,multi1)		xce(3,multi2)	
energy loss per particle (MeV)	deci(3,multi1)		dece(3,multi2)	
number of particles	multi1		multi2	

Table C.1: *Variable summary of the event generator* **laggen**.

Lagdig variables	**Internal chamber**		**External chamber**	
	Cathode 1	Cathode 2	Cathode 1	Cathode 2
CONV= conversion energy to charge (charge/GeV)	$22,8\ 10^{10}$	$26,4\ 10^{10}$	$20,2\ 10^{10}$	$21,4\ 10^{10}$
SIGCT = dispersion on the electronic cascade			26 %	
SIGCE = dispersion on the electronic noise			2300 charges	
CYTHRE = threshold on the strip			6000 charges	
SSCAT = ADC range			1024 channels	
VSCCAT = maximum charge			400000 charges	
number of wires	mcci		mcce	
wire identificator	wci(mcci)		wce(mcce)	
number of strips	mbci(1)	mbci(2)	mbce(1)	mbce(2)
strip identificator	ibci(mbci(1),1)	ibci(mbci(2),2)	ibce(mbce(1),1)	ibce(mbce(2),2)
strip charge(ADC)	cbci(mbci(1),1)	cbci(mbci(2),2)	cbce(mbce(1),1)	cbce(mbce(2),2)

Table C.2: *Variable summary of the program* **lagdig**, *that digitizes the information from* **laggen**.

Prean variables	**Internal chamber**		**External chamber**	
	Cathode 1	Cathode 2	Cathode 1	Cathode 2
number of wires	mcci		mcce	
wire identificator	wci(mcci)		wce(mcce)	
number of clusters	ncl1	ncl2	ncl3	ncl4
cluster multiplicity	mcl1(ncl1)	mcl2(ncl2)	mcl3(ncl3)	mcl4(ncl4)
center of gravity (cm)	bcl1(ncl1)	bcl2(ncl2)	bcl3(ncl3)	bcl4(ncl4)
cluster charge (ADC integral)	ccl1(ncl1)	ccl2(ncl2)	ccl3(ncl3)	ccl4(ncl4)

Table C.3: *Varable summary of the preanalysis progam* **prean**. *The program can analyse events both from simulation and from real data.*

Appendix D

Some calculations on the cylindrical MWPCs

D.1 Determination of the reaction and decay vertex

In this section we calculate the intersection between two or more tracks measured by the cylindrical chambers. Most of the reactions requires at first to calculate the decay vertex and then to use this point in order to calculate the reaction vertex. The method is, anyway, the same in both cases. Let us suppose to have a straight line in the three-dimensional space:

$$\begin{aligned} x(t) &= x_i + \alpha_i t \\ y(t) &= y_i + \beta_i t \\ z(t) &= z_i + \gamma_i t \end{aligned}$$

where x_i, y_i, z_i is a point belonging to the line i and α_i, β_i, γ_i are the components of the unitary vector defining this line. The distance between a point in this space $P = (x, y, z)$ and the line is:

$$d_i^2(t) = (x - x_i - \alpha_i t)^2 + (y - y_i - \beta_i t)^2 + (z - z_i - \gamma_i t)^2$$

The minimum of this distance is given by its derivative with respect the parameter t:

$$\frac{\partial d_i^2(t)}{\partial t} = 0$$

The value t_o that minimizes the equation is:

$$t_o = \alpha_i(x - x_i) + \beta_i(y - y_i) + \gamma_i(z - z_i)$$

and the squared distance at this minimum is:

$$\begin{aligned} d_i^2 = d_i^2(t_o) = \{ & (1-\alpha_i^2)(x-x_i) & -\alpha_i\beta_i(y-y_i) & -\alpha_i\gamma_i(z-z_i)\}^2 \\ +\{ & -\alpha_i\beta_i(x-x_i) & +(1-\beta_i^2)(y-y_i) & -\beta_i\gamma_i(z-z_i)\}^2 \\ +\{ & -\alpha_i\gamma_i(x-x_i) & -\beta_i\gamma_i(y-y_i) & +(1-\gamma_i^2)(z-z_i)\}^2 \end{aligned}$$

In the case of n tracks (two, at least), the point P that minimizes the n distances is given by the solution the following three equations:

$$\sum_{i=1}^{n} \frac{\partial d_i^2}{\partial x} = 0, \quad \sum_{i=1}^{n} \frac{\partial d_i^2}{\partial y} = 0, \quad \sum_{i=1}^{n} \frac{\partial d_i^2}{\partial z} = 0$$

The matrix associated to this linear system is:

$$\left(\begin{array}{ccc|c} \sum_{i=1}^{n}(1-\alpha_i^2) & -\sum_{i=1}^{n}(\alpha_i\beta_i) & -\sum_{i=1}^{n}(\alpha_i\gamma_i) & \sum_{i=1}^{n}\Big[(1-\alpha_i^2)x_i - \alpha_i\beta_i y_i - \alpha_i\gamma_i z_i\Big] \\ -\sum_{i=1}^{n}(\alpha_i\beta_i) & \sum_{i=1}^{n}(1-\beta_i^2) & -\sum_{i=1}^{n}(\beta_i\gamma_i) & \sum_{i=1}^{n}\Big[-\alpha_i\beta_i x_i + (1-\beta_i^2)y_i - \beta_i\gamma_i z_i\Big] \\ -\sum_{i=1}^{n}\alpha_i\gamma_i & -\sum_{i=1}^{n}\beta_i\gamma_i & \sum_{i=1}^{n}(1-\gamma_i^2) & \sum_{i=1}^{n}\Big[-\alpha_i\gamma_i x_i - \beta_i\gamma_i y_i + (1-\gamma_i^2)z_i\Big] \end{array}\right)$$

The solution of this linear system are the coordinates of the point corresponding to the lowest distance to the tracks and it is the vertex of the n tracks.

D.2 Beam misalignment effects

The beam alignment is not perfect on data. A small difference δ_x and δ_y can emerge from small deflections of the electron beam between the two bending magnets.

Let us consider first the case of one chamber. The difference between the measured ϕ^m and the true one ϕ^t in the limit of the chamber radius $R \gg \delta_x, \delta_y$ is:

$$\phi^t - \phi^m = \Delta / R$$

where Δ is the circumference arc between ϕ^t and ϕ^m. If we approximate the arc Δ with a straight line, it can be written as:

$$\Delta = -\delta_x \sin \phi^m + \delta_y \cos \phi^m$$

Let us assume that Δ is the same for both chambers: this approximation holds if the variation $\phi^t - \phi^m$ is small. In this case:

$$\begin{cases} \phi^t - \phi_i^m = \Delta / R_i \\ \phi^t - \phi_e^m = \Delta / R_e \end{cases}$$

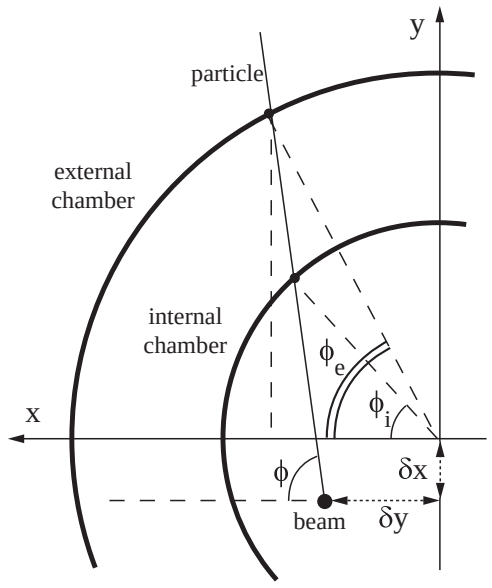

Figure D.1: *Association between the two chambers.*

And the real difference we measure is:

$$\phi_e^m - \phi_i^m = \Delta / R_i - \Delta / R_e = \frac{R_e - R_i}{R_e R_i} \left(-\delta_x \sin \phi_i^m + \delta_y \cos \phi_i^m \right)$$

List of Figures

List of Tables

Bibliography

[1] L.M. Brown and H. Rechenberg. *The Origin of the Concept of Nuclear Forces*, volume 1. Institut of Physics Publishing Bristol and Philadelphia, 1996.

[2] N. Kaiser *et al. SU(3) chiral dynamics with coupled channels Eta and Kaon photoproduction. Nuclear Physics*, A612:297–320, 1997.

[3] Ll. Ametller *et al. Low energy photon-photon diffusion into three pions in generalized chiral perturbation theory. Physical Review D*, 60:094003, 1999.

[4] N. Levy *et al. Kaon photoproduction. Nuclear Physics*, B55:493–512, 1973.

[5] B. Saghai. *From known to undiscovered resonances. arXiv nucl-th/0105001*, 2 May 2001.

[6] C. Caso *et al. Particle Data Group. The European Physical Journal*, 15:1, 2000.

[7] D.M. Manley and E.M. Saleski. . *Physical Review D*, 45:4002, 1992.

[8] R.A. Arndt *et al.* . *Physical Review C*, 52:2120, 1995.

[9] M. Batinić *et al.* . *Physics Scripta*, 58:15, 1998.

[10] T.P. Vrana *et al. Baryon resonance extraction from πN data using a unitary multichannel model. Physics Reports*, 328:181, 2000.

[11] R. Workman *et al. Extraction of the $D_{13}(1520)$ photon-decay couplings from pion- and η-photoproduction data. Physical Review C*, 62:048201, 2000.

[12] W.-T. Chiang *et al. An isobar model for η photo- and elctro-production on the nucleon. Proceeding NSTAR 2001*, page 171, 2001.

[13] G. F. Chew *et al. Relativistic Dispersion Relation Approach to Photomeson Production. Physical Review*, 106:1345–1355, 1957.

[14] C. G.Fasano *et al. Spin observables at threshold for meson photoproduction. Physical Review C*, 46:2430–2455, 1992.

[15] J. Ajaka *et al. New measurement of* Σ *beam asymmetry for* η *meson photoproduction on the proton. Physical Review Letters*, 81:1797, 1998.

[16] L. Tiator *et al. Eta photoproduction. pi-N Newsletters*, 1998.

[17] B. Krusche *et al. Near Threshold Photoproduction of* η *Mesons off the Proton. Physical Review Letters*, 74:3736, 1995.

[18] R.M. Davidson *et al. Effective-Lagrangian approach to the theory of pion photoproduction in the* $\Delta(1232)$ *region. Physical Review D*, 43:71, 1991.

[19] M. Benmerrouche *et al. Effective Lagrangian approach to the theory of* η *photoproduction in the* $N^*(1535)$ *region. Physical Review D*, 51:3237, 1995.

[20] H. R. Hicks *et al. Isobar analysis of* $\gamma p \to \eta p$. *Physical Review D*, 7:2614, 1973.

[21] H. Thom. *Phenomenological Analysis of* $K^+\Lambda$ *Photoproduction. Physical Review*, 151:1322, 1966.

[22] Y. Renard. K^+ *Photoproduction low-energy description and duality relations. Nuclear Physics*, B40:499–540, 1971.

[23] M.Q. Tran *et al. Measurement of* $\gamma p \to K^+\Lambda$ *and* $\gamma p \to K^+\Sigma^0$ *at photon energies up to 2 GeV. Physics Letters*, B445:20–26, 1998.

[24] S. Goers *et al. Measurement of* $\gamma p \to K^0\Sigma^+$ *at photon energies up to 1.55 GeV. Physics Letters*, B391:446–450, 1997.

[25] K.-H. Glander *et al. Recent results on the Kaon photoproduction at SAPHIR in the reactions* $\gamma p \to K^+\Lambda$ *and* $\gamma p \to K^0\Sigma^+$. *Proceedings NSTAR2001*, page 381, 2001.

[26] R.A. Adelseck and B. Saghai. *Kaon photoproduction: Data consistency, coupling constants and polarization observables. Physical Review C*, 42:108, 1990.

[27] J. C. David *et al. Electromagnetic production of associated strangess. Physical Review C*, 46:1617, 1992.

[28] T. Mizutani *et al. Off-shell effects in the electromagnetic production of strangness. Physical Review C*, 58:75, 1998.

[29] R. A. Williams *et al. Hyperon electroproduction in a crossing and duality constrained model. Physical Review C*, 46:1617, 1992.

[30] P. Oswald. *Photo- et électro-production de kaons sur le nucléon et le deuton.* PhD thesis, Université Claude Bérnard - Lyon I, November 2001.

[31] R. A. Williams *et al. Physical Review C*, 53:1996, 1996.

[32] R.M. Davidson and R. Workman. *Form factors and photoproduction amplitudes. Physical Review C*, 2001.

[33] T. Mart and C. Benhold. *Evidence for a missing nucleon resonance in kaon photoproduction. Physical Review C*, 1999.

[34] Z. Li, B. Saghai, T. Ye. *in progress.*

[35] N. Isgur and G. Karl. *Positive-parity excited baryons in a quark model with hyperfine interactions. Physical Review D*, 19:2653, 1979.

[36] S. Capstick and W. Roberts. . *Prog. Part. Nucl. Phys.*, 45(Suppl. 2):5241, 2000.

[37] R. Bijker *et al.* . *Ann. Phys.*, 284:89, 2000.

[38] L.Ya. Glozman and D.O. Riska. . *Physics Reports*, 268:263, 1996.

[39] Zhenping Li. *Kaon photoproduction off nucleons in the chiral quark model. Physical Review C*, 52:1648–1661, 1995.

[40] Zhenping Li *et al. Unified approach to pseudoscalar meson photoproduction off nucleons in the quark model. Physical Review C*, 56:1099, 1997.

[41] A. Manohar and H. Georgi. . *Nuclear Phyiscs B*, 234:189, 1984.

[42] L. Ya. Glozman *et al. Unified description of light and strange-baryon spectra. Physical Review D*, 58:074008, 1998.

[43] R.P. Bickerstaff and A.W. Thomas. *Up-down uqrks massdifference in the MIT bag model. Physical Review D*, 25:25, 1982.

[44] D.H. Lu *et al. Chiral bag model approach to Δ electroproduction. Physical Review C*, 55:3108, 1997.

[45] C. Gobbi and D.O. Riska. *Electromagnetic Properties of Predicted Bound States of Heavy Quarkonia and Nucleons. Nuclear Physics*, A568:779–797, 1994.

[46] C.A. Carlson *et al. Phys. Rev. D*, 59:114008, 1999.

[47] D. Pirjol and T.-M. Yan. *Phys. Rev. D*, 57:5434, 1998.

[48] W. Kaune *et al. Inclusive cross sections for pion and proton production by photons using collimated coherent bremsstrahlung. Physical Review D*, 11:478, 1975.

[49] H. Steffens *et al. A Spin rotator for producing a longitudinally polarized electron beam with MAMI. Nucl. Instr. and Meth.*, A325:378–383, 1993.

[50] A. D'Angelo *et al. LADON project. Annual reoport of the INFN of Roma2*, 1995.

[51] F. Renard. *Étude de la structure du nucléon via la photoproduction de mésons pseudoscalaires à GRAAL.* PhD thesis, Université Joseph Fourier - Grenoble I, December 1999.

[52] J. Ajaka. *Photoproduction dun méson eta sur l'hydrogène du seuil jusqu'à1100 MeV: mesure de l'asymétrie faisceau* Σ. PhD thesis, Université Louis Pasteur - Strasbourg, December 1997.

[53] F. Ghio *et al. The Graal high resolution BGO calorimeter and its energy calibration and monitoring system. Nucl. Instr. and Meth.*, A404:71, 1998.

[54] L. Nicoletti. *Calibrazione e controllo di stabilità di un calorimetro costituito da una sfera di BGO*, Università degli Studi di Roma "Tor Vergata" (Italy), 1996. *Tesi di Laurea.*

[55] P. Levi Sandri *et al. Nucl. Instr. and Meth.*, A370:396, 1996.

[56] P. Calvat. *Mesure des observables de polarisation dans la photoproduction des mésons pseudoscalaires à GRAAL.* PhD thesis, Université Joseph Fourier - Grenoble I, January 1997.

[57] V. Kouznetsov *et al. A large acceptance lead-scintillator time-of-flight wall for neutral and charged particles. Nucl. Instr. and Meth.*, A, 2001.

[58] D. Barancourt *et al. The data acquisition system for the GRAAL experiment at the ESRF in Grenoble. Nucl. Instr. and Meth.*, A388:226, 1997.

[59] *GEANT - Detector Description and Simulation Tool*, 1973. CERN Program Library Long Writeup W5013 (1994); CERN Program Library Office, CERN-CN Division, CH-1211 Geneva 23, Switzerland.

[60] L. Mazzaschi *et al. Nucl. Instr. and Meth.*, A305:391, 1991.

[61] G. Charpak *et al. Nucl. Instr. and Meth.*, A167:455, 1979.

[62] E. Gatti *et al. Nucl. Instr. and Meth.*, 163:83, 1979.

[63] J. Bouvier *et al. Analog and digital ASICs developpments for nuclear instrumentation*, 1997. Rapport interne ISN.

[64] I. Endo *et al. Systematic shifts of evaluated charge centroid for the cathode read-out multiwire proportional chamber. Nucl. Instr. and Meth.*, A188:51–58, 1981.

[65] S. Koutzenzov, 2000. Private communication.

[66] F. Renard *et al. Differential Cross Section Measurement of η Photoproduction on the proton from Threshold to 1100 MeV. Physical Letters B*, accepted.

[67] O. Bartalini. , Università degli Studi di Roma "Tor Vergata" (Italy), 1999. *Tesi di Laurea.*

[68] A. Zucchatti *et al. Optimisation of clustering algorithms for the reconstruction of events started by a 1 GeV photon beam in a segmented BGO calorimeter. Nucl. Instr. and Meth.*, A425:536–548, 1999.

[69] J.P. Bocquet *et al. Nucl. Phys.*, pages 466c–472c, 2001.

[70] B. Saghai, 2001. Private communication.

[71] B. Saghai and F. Tabakin. *Pseudoscalar meson photoproduction: From known to undiscovered resonances. Physics Review C*, 55:917, 1997.

[72] I. S.Barker *et al. Complete experiments in pseudoscalar photoproduction. Nuclear Physics*, B95:347–356, 1975.

[73] B. Saghai. *Multipole decomposition of pseudoscalar mesons photoproduction observables. in progress*, 2001.